DISSERTATION

OBLIQUE PUMPING, RESONANCE SATURATION, AND SPIN WAVE INSTABILITY PROCESSES IN THIN PERMALLOY FILMS

Submitted by

Heidi M. Olson

Department of Physics

In partial fulfillment of the requirements

For the Degree of Doctor of Philosophy

Colorado State University

Fort Collins, Colorado

Spring 2008

COLORADO STATE UNIVERSITY

February 14, 2008

WE HEREBY RECOMMEND THAT THE DISSERTATION PREPARED UNDER OUR SUPERVISION BY HEIDI M. OLSON ENTITLED OBLIQUE PUMPING, RESONANCE SATURATION AND SPIN WAVE INSTABILITY PROCESSES IN THIN PERMALLOY FILMS AS FULFILLING IN PART REQUIREMENTS FOR THE DEGREE OF DOCTOR OF PHILOSOPHY.

Committee on Graduate Work

Professor Martin Gelfand

Professor Robert Leisure

Professor Carmen S. Menoni

Professor Mingzhong Wu

Advisor Professor Carl E. Patton

Department Head Professor Hans D. Hochheimer

ABSTRACT OF DISSERTATION

OBLIQUE PUMPING, RESONANCE SATURATION, AND SPIN WAVE INSTABILITY PROCESSES IN THIN PERMALLOY FILMS

The study of nonlinear dynamics in metal films is of increasing importance as advancements are made in magnetic recording. In this dissertation, these interactions are examined by the study of first order spin wave instability (SWI) processes that occur for external static magnetic fields well below ferromagnetic resonance (FMR), and second order SWI processes that occur for static fields over the full FMR field range. This work is concerned specifically with the study of the high power resonance saturation and oblique pumping responses in thin Permalloy films, the microwave threshold amplitudes at which the instabilities occur, and the theoretical analysis of the relevant SWI processes.

To greatly increase measurement accuracy and reduce measurement time, the high power FMR system has been modified and new calibration techniques implemented. The modifications to the system allow for fully automated and calibrated microwave threshold amplitude vs. static field measurements, termed butterfly curves.

Resonance saturation butterfly curves have been measured for an in-plane field configuration for 35 - 123 nm thin Permalloy films. The butterfly curves show a jump on the low field side associated with a low field shift of the FMR profile and a foldover like asymmetry development. Apart from the jump, the second order Suhl SWI theory, suitably modified for thin films, provides good fits to the butterfly curve data through the use of constant spin wave relaxation rates that are on the same order as expected for intrinsic magnon-electron scattering processes. The FMR in-plane precession cone angles at threshold are small.

Oblique pumping butterfly curves have been measured at different in-plane field configurations for 104 and 123 nm thin Permalloy films. The butterfly curves show thickness dependent high field cutoffs that agree with the field points at which the bottom of the spin wave band moves above one half the pump frequency. A combination of parallel and perpendicular first order SWI theory, suitably modified for thin films, shows good fits to the data except at low fields where the thin film approximation is not applicable. The damping trial functions used for the fits correspond to magnon-electron and three-magnon scattering processes.

Heidi M. Olson
Department of Physics
Colorado State University
Fort Collins, CO 80523
Spring 2008

DEDICATION

This work is dedicated to my biggest fan, my mother. She always encouraged me to indulge my curiosity and provided me with the means to do so. From Saturday morning inventions/messes in the kitchen to teaching me how to argue, my mother showed me how to be me.

ACKNOWLEDGEMENTS

I would like to thank my advisor Carl E. Patton for all his support throughout the years and the pressure to finish when it came down to the very end. I have also greatly enjoyed his ability to provide extremely useful arguments.

Pavol Krivosik was a wonderful very patient mentor through this process. He guided me through spin wave instability theory, answered questions no matter how far out in left field they may have been, and was always willing to help out with a quick calculation.

Erica Snow and Margo Greenfield are two of the kindest and most supportive people I have ever met and were there for me again and again through the toils of my graduate career.

I owe so much to my family. From Dad, Laura, Lindsey, Eli, and Zach, to all of my extended Olson and Postnikoff families, the love, support and encouragement that you have given so freely has held me together through the worst of times. Thank you.

Finally, I would like to thank Maureen Kotzbach for all her support throughout the years and for giving even when she had nothing left to give. You rock the cat box!

This work was supported in part by the Information Storage Industry Consortium EHDR program.

TABLE OF CONTENTS

INTRODUCTION

This chapter provides an introduction to high power ferromagnetic resonance (FMR) research and an overview of this thesis. The first section presents a brief introduction to the basic concepts and history of FMR and high power phenomena. The second section discusses the motivation for the study of high power FMR in thin Permalloy films and reviews past work. Special emphasis is given to results for thin metal films Very little work on metal films, by means of high power FMR measurements, has been done. Additionally, the majority of previous work was limited in scope and only qualitative in nature. The final section presents a detailed overview of this dissertation.

1.1 BRIEF INTRODUCTION TO FERROMAGNETIC RESONANCE

Low power FMR was discovered by Griffiths (1946) and provides a means to study magnetic excitations in ferromagnetic and ferrimagnetic materials at microwave frequencies. The basic FMR experiment involves a sample placed in an external static magnetic field. The field is sufficiently large to magnetize the sample parallel to the field direction. If the magnetization is slightly perturbed, it precesses about the field direction. Relaxation mechanisms associated with the sample cause the precession to be damped and the magnetization to decay to its equilibrium position parallel to the field.

To excite the precessional motion of the uniform magnetization mode, a microwave magnetic pumping field is applied to the sample, generally in a direction perpendicular to the static field. The microwave frequency is then swept over a particular frequency range and the microwave power absorbed by the sample is measured. When the microwave frequency is far from the precessional frequency, very little energy is coupled into the uniform mode and the power absorbed is small. However, when the microwave frequency is approximately equal to the precessional frequency, the coupling of energy into the uniform mode is large and the power absorbed is large. This effect is termed ferromagnetic resonance and was first explained by Kittel (1948).

Ferromagnetic resonance can also be studied through a static field swept measurement rather than a frequency swept measurement. The microwave frequency is kept fixed and the static magnetic field is swept over a certain field range. For a particular static field, the precessional frequency is approximately the microwave pumping frequency and again there is a FMR response. For different microwave pumping frequencies, FMR occurs at different static magnetic fields. It is important to note that relaxation mechanisms produce a broadened frequency or field swept loss profile. The width of this FMR profile is measured to obtain information on the relaxation mechanisms.

The comments above concerned low power ferromagnetic resonance and the linear response of the magnetization. If the microwave power is increased above a particular threshold power, magnetic excitations with nonlinear behavior produce two separate phenomena over a broad range of static fields. These phenomena are termed resonance saturation and subsidiary absorption. They were first observed by Bloembergen and Damon (1952) and Bloembergen and Wang (1954), respectively. Resonance saturation is a decrease in loss at the FMR peak and a broadening of the FMR profile. Subsidiary absorption is an increase of loss over a broad static field range below the FMR field.

These nonlinear effects were successfully explained by Anderson and Suhl (1955). A comprehensive spin wave instability (SWI) theory was developed by Suhl (1957) and Schloemann (1959). These theories show that energy is indirectly coupled through the uniform magnetization mode and parametrically pumped into spin wave modes at a power dependent rate. Spin wave modes consist of neighboring spins which are slightly out-of-phase and form a wave of dynamic magnetization. At the point in power where the power dependent rate exceeds the relaxation rate of the spin waves, the occupation numbers of the spin waves increase above thermal levels and there is an abrupt change in the loss. For resonance saturation, the precession angle of the magnetization locks up and energy is parametrically pumped into spin waves at the pump frequency. This results in a broadening of the FMR profile and a decrease in loss at the FMR field. For subsidiary absorption, the energy is parametrically pumped into spin waves at half the pump frequency. This results in the increase in loss at static fields below FMR profile.

A third high power phenomenon, called parallel pumping, was discovered by Schloemann *et al.* (1960). This nonlinear process is different from resonance saturation and parallel pumping in that it occurs for the field configuration where the microwave pumping field is parallel to the static field. As with subsidiary absorption, parallel pumping gives an increase in loss over a broad low field region. It is also a threshold effect. In this case, however, the energy is coupled directly from the microwave pumping field to parametrically pumped spin waves at half the microwave pumping frequency rather than indirectly through the FMR response.

The combination of the subsidiary absorption and parallel pumping processes for configurations between perpendicular and parallel is called oblique pumping. Oblique pumping provides a means to experimentally compare the two separate nonlinear effects.

1.2 MOTIVATION FOR HIGH POWER FERROMAGNETIC RESONANCE IN THIN PERMALLOY FILMS

The metal material of nominal composition $Ni_{80}Fe_{20}$, called Permalloy by industry, was discovered in 1914 by Elmen (2007). Permalloy thin films are ferromagnetic materials and have the lowest magnetic loss yet measured in any metal film. A ferromagnetic material is a material in which the magnetic moments of the atoms or ions in a magnetic domain tend to align parallel to one another. The sum of these magnetic moments per unit volume is the magnetization [Weast and Astle (1982)]. In addition to the attributes mentioned above, Permalloy has several properties that make it an ideal candidate for study and applications. It is a soft material with a very low coercive force. For bulk, the coercive force is about 0.05 Oe. It has a large saturation magnetization. For bulk, the saturation induction is about 10-15 kG. Finally, Permalloy has a very large permeability. For bulk, the permeability is about 9×10^4 [Bozorth (1978)].

As mentioned above, Permalloy films are ideal for applications. Some of the early applications included telephone transformer coils and sensitive relays [Bozorth (1978)]. New applications are constantly in development. One such application is the use of Permalloy in RF inductors. The high permeability of Permalloy improves the effective inductance up to 50% [Ni *et al.* (2006)]. A current study for future applications is in the use of Permalloy to fill one-end-opened carbon nanotubes. These filled nanotubes have many new potential applications that include magnetic drug delivery systems and high-density magnetic recording [Wang *et al.* (2006)]. One important application of Permalloy has been in the hard drive industry as a recording head core material.

In 1979, the thin film inductive recording head was invented and Permalloy was used as the head core material [Osaka *et al.* (2005), Osaka and Sayama (2007)]. However, as the density of magnetic recording media increased, media with a larger coercivity were required to circumvent the superparamagnetic limit related to thermal effects and the loss of bit integrity. With the increase in coercivity of the media, it became necessary in the late 1990's, to find a soft metal for the write head core material with an even larger saturation magnetization, which is still true today. Currently, Co-Ni-Fe is used by some industries as the head core material, as it has a saturation magnetization of 20-21 kG.

Although Permalloy is no longer used as a core material in heads, the magnetic properties of the material are important to understand. The exploration of the magnetic properties of this low loss material provides a basis for the study of high loss metal films and patterned films. In addition to losses there are other magnetic properties of interest in metal ferromagnetic materials. One such property is anisotropy. If Permalloy is deposited in an external magnetic field, the magnetization shows small planer anisotropy in the 5 – 10 Oe range. This small anisotropy is neglected for this work, as it is much smaller than the static magnetic fields of interest.

The losses associated with nonlinear processes can, in principle, have a dramatic effect on magnetization switching in recording applications. The extra losses, for example, can serve to reduce switching speeds in conventional heads and media applications. At the same time, the nonlinear interactions can also promote magnetization reversal. This has been recently demonstrated for a variety of current driven nano contact and nano pillar spin torque devices [Hoefer *et al.* (2005), Slavin and Kabos (2005), Guan *et al.* (2007)]. Dobin and Victora (2004) have recently demonstrated a direct connection between the nonlinear dynamics in large angle magnetization switching in thin films and SWI processes.

One clear way to examine the basic nonlinear interactions that are relevant to large angle switching in thin films is to study the SWI processes that occur at and below the FMR profile for high microwave power levels. This work is concerned specifically with the resonance saturation and oblique pumping processes. While high power FMR experiments do not usually extend to angles as large as those that occur in switching, they provide a measure of the precession angles at which nonlinear effects can come into play. In Permalloy films, for example, the onset of second order SWI processes and resonance saturation effects generally occur at precession angles in the $3^{\circ} - 6^{\circ}$ range.

While there has been extensive work on SWI processes in ferrites, high power ferromagnetic work on metal films is limited to only a few studies in the 1960's. High power resonance saturation and subsidiary absorption processes for in-plane magnetized Permalloy films were first observed by Comly *et al.* (1963). Berteaud and Pascard (1965) observed resonance saturation for perpendicular-to-plane magnetized Permalloy films. Berteaud and Pascard (1966) expanded on the previous work to include in-plane to perpendicular-to-plane resonance saturation and oblique pumping measurements. The first parallel pumping experiments on Permalloy were performed by Comly (1965). Milton (1968) extended the in-plane magnetized resonance saturation measurements to include temperature effects.

While the majority of films used in these experiments were very thick, issues with conductivity were not taken into account. There were no quantitative connections to the SWI theory and the qualitative discussions about the results mostly utilized bulk SWI theory. In 1964 a thin film approximation was used by Harte (1964) to obtain a spin wave dispersion relation for thin films. Qualitative comparisons of the data to thin film SWI theory were not performed until 1965 by Comly (1965). It should be noted that although Comly did use spin wave instability theory, suitably modified for thin films, the films and foils used were too thick to be fully explained by thin film theory.

Recent work by An *et al.* (2004) extended subsidiary absorption measurements to include full data on the SWI threshold microwave field amplitude vs. static field for in-plane magnetized films. These measurements are termed butterfly curves. These authors also provided a full analysis of the data based on the first order SWI theory, suitably modified for the film geometry. As a result of cavity loading and calibration issues, An *et al.* (2004) did not include any quantitative work on resonance saturation or second order SWI processes.

Until now oblique pumping measurements in in-plane magnetized Permalloy films have never been performed. There have been extensive oblique pumping measurements in ferrites, however. In 1969 oblique pumping experiments by Patton (1969) in single crystal yttrium-iron-garnet (YIG) and Dy-doped YIG showed quite different results. For the Dy-doped YIG there was a smooth transition of the butterfly curves as the angle between the microwave field and the static field was changed from 90° to 0°. On the other hand, the single crystal YIG results showed butterfly curves at the intermediate angles that were not smooth but rather had characteristics of both the 90° and the 0° curves. Variations on these experiments followed [Green *et al.* (1969), Patton and Jantz (1978), Patton (1980), and Liu and Patton (1982)]. In 1995, Wiese *et al.* (1995) were able to explain this angular dependent phenomena to some extent with the use of a thin film based instability theory. Many questions remain about the behavior of the butterfly curves in thin metal films for oblique pumping.

1.3 OVERVIEW OF THIS THESIS

Chapter 2 provides a discussion of low and high power FMR. The magnetic torque equation that governs the motion of the magnetization for low and high power responses is introduced. The discussion of low power FMR includes an introduction to the uniform mode and the FMR response. The high power FMR overview presents an introduction to the basic resonance saturation, subsidiary absorption, parallel pumping and oblique pumping responses.

Chapter 3 develops the first and second order SWI theory, suitably modified for thin films. Section 3.1 establishes the sample geometry in the precession frame of reference and gives a brief derivation of the total effective field. Section 3.2 analyzes the solution to the linearized torque equation of motion with phenomenological Gilbert damping included to obtain the spin wave dispersion relation and other important relations that pertain to linear spin waves. The special case of the uniform mode solution to the torque equation is examined.

Section 3.3 uses the methods and formalism established in the previous sections to develop working equations for the first and second order SWI processes. Section 3.4 uses the working equations developed in Sec. 3.3 to perform example calculations. Example calculations are presented for resonance saturation, subsidiary absorption, parallel pumping, and one oblique pumping angle for a 104 nm thin Permalloy film. Threshold microwave field vs. static magnetic field butterfly curves are presented, along with results on the corresponding critical spin wave modes.

Chapter 4 provides on overview of the thin Permalloy films. Basic information on the samples is provided, such as thickness, composition, and sample preparation details. The samples were provided by Dr. S. Konishi, Kyushu, University, Fukuoka, Japan. Static magnetic and measured and derived microwave properties of the films are presented.

Chapter 5 introduces the high power FMR spectrometer system and presents the newly developed calibration techniques, experimental procedures, example data, and corresponding theoretical fits. Section 5.1 introduces the high power system design and instrumentation. Section 5.2 presents the system calibration procedure. It is important to note that the cavity calibration procedure is discussed separately in Sec. 5.4. Section 5.3 introduces the experimental procedure to obtain uncalibrated high power FMR profiles. Example FMR data are provided and discussed. These results provide instrumental in the proper calibration of the cavity.

Section 5.4 presents the cavity calibration procedure and the obstacles associated with the calibration of the cavity are presented and resolved. The procedures to determine the critical limit for cavity loading, measurement techniques to obtain the calibration constant, and the extended cavity calibration are discussed. Section 5.5 establishes the measurement procedures to obtain calibrated microwave threshold curves, extract the threshold fields, and create butterfly curves. Section 5.6 provides example butterfly curve results with the corresponding theoretical fits for resonance saturation and oblique pumping.

Chapter 6 presents the results of the resonance saturation threshold field measurements on the 35, 57, 74, 104, and 123 nm thin Permalloy films. The results show that the theoretical analysis of the threshold data, based on the second order SWI theory, suitably modified for thin films, yielded good fits to the butterfly curve data based on a single field independent value of the spin wave linewidth. These linewidths and the corresponding Gilbert damping parameter values are consistent with those expected for intrinsic magnon-electron relaxation [Meckenstock *et al.* (2004), Frait and Fraitova (1980), Meckenstock *et al.* (1995)]. The implicit critical modes are consistent with the original Suhl theory and the FMR precession angles at threshold are quite small, on the order of few degrees.

Chapter 7 presents the results of the oblique pumping threshold field measurements on the 104 and 123 nm thin Permalloy films. The results show a thickness dependent spin wave band edge effect at a static field that corresponds to the point where the half pumping frequency drops below the spin wave band. The threshold responses as a function of coupling angle provide evidence that energy is very weakly coupled into the spin wave modes through the parallel coupling coefficient. The theoretical fits to the threshold data, based on the first order SWI theory, suitably modified for thin films, yielded good fits to the data except at low fields. At low fields the thin film approximation used for the theoretical calculations breaks down. The spin wave linewidth trial function that best fits the data consists of a Gilbert damping term and trial function that loosely corresponds to a three magnon interaction. The corresponding Gilbert damping parameters agree with the parameters obtained from resonance saturation only for the subsidiary absorption configuration and show that the 123 nm film has an overall lower loss than the 104 nm film.

Chapter 8 provides an overview of the highlights and conclusions of this work. In particular, the high power FMR system improvements and calibrations and the conclusions from the resonance saturation and oblique pumping experiments are briefly reviewed. Finally, ideas for future work on metal films are presented.

REFERENCES

[An *et al.* (2004)] S. Y. An, P. Krivosik, M. A. Kramer, H. M. Olson, A. V. Nazarov, and C. E. Patton, J. Appl. Phys. **96**, 1572 (2004).

[Anderson and Suhl (1955)] P. W. Anderson and H. Suhl, Phys. Rev. **100**, 1788 (1955).

[Berteaud and Pascard (1965)] A. Berteaud and H. Pascard, J. Appl. Phys. **36**, 970 (1965).

[Berteaud and Pascard (1966)] A. Berteaud and H. Pascard, J. Appl. Phys. **37**, 2035 (1966).

[Bloembergen and Damon (1952)] N. Bloembergen and R. W. Damon, Phys. Rev. **85**, 699 (1952).

[Bloembergen and Wang (1954)] N. Bloembergen and S. Wang, Phys. Rev. **93**, 72 (1954).

[Bozorth (1978)] Bozorth, *Ferromagnetism* (IEEE, Inc., New York, 1978).

[Comly *et al.* (1963)] J. B. Comly, T. Penney, and R. V. Jones, J. Appl. Phys. **34**, 1145 (1963).

[Comly (1965)] J. B. Comly, Technicial Report No. 485, (unpublished) 1965.

[Dobin and Victora (2004)] A. Y. Dobin and R. H. Victora, J. Appl. Phys. **95**, 7139 (2004).

[Elmen (2007)] Elmen, In Encyclopaedia Britannica, Retrived August 29 2007, from Encyclopaedia Britannica Online: http://www.britannica.com/eb/article-9032459.

[Frait and Fraitova (1980)] Z. Frait and D. Fraitova, J. Magn. Magn. Mater. **15**, 1081 (1980).

[Green *et al.* (1969)] J. J. Green, C. E. Patton, and E. Stern, J. Appl. Phys. **40**, 172 (1969).

[Griffiths (1946)] J. H. E. Griffiths, Nature **158**, 670 (1946).

[Guan *et al.* (2007)] Y. Guan, W. E. Bailey, E. Vescovo, C. C. Kao, and D. A. Arena, J. Magn. Magn. Mater. **312**, 374 (2007).

[Harte (1964)] K. J. Harte, Technical Report No. 364, (unpublished) 1964.

[Hoefer *et al.* (2005)] M. A. Hoefer, M. J. Ablowitz, B. Ilan, M. R. Pufall, and T. J. Silva, Phys. Rev. Lett. **95**, 267206 (2005).

[Kittel (1948)] C. Kittel, Phys. Rev. **73**, 155 (1948).

[Liu and Patton (1982)] Y. H. Liu and C. E. Patton, J. Appl. Phys. **53**, 516 (1982).

[Meckenstock *et al.* (1995)] R. Meckenstock, O. v. Geisau, J. Pelzl, and J. A. Wolf, J. Appl. Phys. 77, 6439 (1995).

[Meckenstock *et al.* (2004)] R. Meckenstock, D. Spoddig, Z. Frait, V. Kambersky, and J. Pelzl, J. Magn. Magn. Mater. **272**, 1203 (2004).

[Milton (1968)] A. F. Milton, Ph. D. dissertation, Harvard University, Cambridge, Massachusetts (1968).

[Ni *et al.* (2006)] W. Ni, J. Kim, and E. C. Kan, IEEE Trans. Magn. **42**, 2827 (2006).

[Osaka *et al.* (2005)] T. Osaka, T. Asahi, J. Kawaji, and T. Yokoshima, Electrochimica Acta **50**, 4576 (2005).

[Osaka and Sayama (2007)] T. Osaka and J. Sayama, Electrochimica Acta **52**, 2884 (2007).

[Patton (1969)] C. E. Patton, J. Appl. Phys. **41**, 431 (1969).

[Patton and Jantz (1978)] C. E. Patton and W. Jantz, IEEE Trans. Magn. **14**, 698 (1978).

[Patton (1980)] C. E. Patton, Proceedings of the International Conference, October 1980, High Power Microwave Processes and Parametric Pumping in Single Crystal Ferrites.

[Schloemann (1959)] E. Schloemann, Technical Report No. R-48, (unpublished) 1959.

[Schloemann *et al.* (1960)] E. Schloemann, J. J. Green, and U. Milano, J. Appl. Phys. **31**, 386S (1960).

[Slavin and Kabos (2005)] A. N. Slavin and P. Kabos, IEEE Trans. Magn. **41**, 1264 (2005).

[Suhl (1957)] H. Suhl, J. Phys. Chem. Solids **1**, 209 (1957).

[Wang *et al*. (2006)] X. H. Wang, H. Orikasa, N. Inokuma, Q. H. Yang, P. X. Hou, H. Oshima, K. Itoh, and T. Kyotani, J. Mater. Chem. **17**, 986 (2006).

[Weast and Astle (1982)] R. C. Weast and M. J. Astle, *CRC Handbook of Chemistry and Physics 63rd ed*, (CRC Press, Inc., 1982).

[Wiese et al. (1995)] G. Wiese, P. Kabos, and C. E. Patton, Phys. Rev. B **51**, 15085 (1995).

INTRODUCTION TO LOW AND HIGH POWER FERROMAGNETIC RESONANCE

INTRODUCTION

This chapter provides an introduction to high power ferromagnetic resonance. Section 2.1 introduces the magnetic torque equation of motion that describes the precession dynamics of the magnetization. Section 2.2 qualitatively discusses the low power ferromagnetic resonance (FMR) response. Section 2.3 introduces the main high power FMR phenomena. The resonance saturation, subsidiary absorption, parallel pumping, and oblique pumping responses are qualitatively presented and loss vs. external magnetic field graphs are shown to demonstrate these phenomena.

2.1 MAGNETIC TORQUE EQUATION OF MOTION

Ferromagnetic materials [Ashcroft and Mermin (1976), Weast and Astle (1982)] are magnetically ordered substances where the microscopic localized magnetic moments of the electrons tend to align parallel to one another in a zero applied field. The magnetic moment of an electron $\boldsymbol{\mu}$ is related to the electron spin $\mathbf{s}$ by

$\boldsymbol{\mu} = -g_e \,|\, e/2m_e c \,|\, \mathbf{s}$ where g_e is the Landé g factor, e is the magnitude of the electron charge, and m_e is the mass of the electron. For an electron the Landé g factor is 2. The connection between magnetic moment and spin can be more clearly written as $\boldsymbol{\mu} = -|\gamma_e|\mathbf{s}$, where $|\gamma_e|$ is the absolute value of the gyromagnetic ratio for an electron and is 1.76×10^7 rad/sec Oe. In more practical CGS units, $|\gamma_e|/2\pi$ is equal to 2.8 GHz/kOe.

If an external static magnetic field $\mathbf{H}$ is applied to an isolated magnetic moment $\boldsymbol{\mu}(\mathbf{r},t)$, a torque is created on the magnetic moment, $\boldsymbol{\tau}(\mathbf{r},t) = \boldsymbol{\mu}(\mathbf{r},t)\times\mathbf{H}$. The magnetic moment, then, precesses about the $\mathbf{H}$ field. The torque is also the time rate of change of the electron spin, $\boldsymbol{\tau}(\mathbf{r},t) = d\mathbf{s}(\mathbf{r},t)/dt$. The precession of the magnetic moment in the static field is then described by $d\boldsymbol{\mu}(\mathbf{r},t)/dt = -|\gamma_e|\boldsymbol{\mu}(\mathbf{r},t)\times\mathbf{H}$.

The precessional equation above can be extended to a ferromagnetically ordered system with a magnetic moment per volume $\mathbf{M}(\mathbf{r},t)$ or magnetization. The magnetic torque equation of motion is

$$\frac{d\mathbf{M}(\mathbf{r},t)}{dt} = -|\gamma|\mathbf{M}(\mathbf{r},t)\times\mathbf{H}_{\text{eff}}(\mathbf{r},t) \quad . \tag{2.1}$$

This equation is for a ferromagnetically ordered system of magnetic moments and is much more complicated. One such complication is that the Landé g factor and, hence, the $|\gamma|$ is not necessarily that of a free electron spin but is somewhat modified by spin orbit coupling. A second major complication is that the magnetization no longer simply precesses around the static field but rather an equilibrium direction based on the total effective field $\mathbf{H}_{\text{eff}}(\mathbf{r},t)$. The $\mathbf{H}_{\text{eff}}(\mathbf{r},t)$ consists of the static magnetic field, dipolar field or Maxwellian fields, the non-Maxwellian effective exchange field due to the exchange interaction, an effective anisotropy field, and the applied microwave pumping field. Through the $\mathbf{H}_{\text{eff}}(\mathbf{r},t)$ field specific sample properties, such as sample shape and anisotropy, are folded into the torque equation. In addition, the $\mathbf{H}_{\text{eff}}(\mathbf{r},t)$ field generally has terms that depend on the magnetization. As a result, the torque equation comprises a coupled set of nonlinear equations. At high power the nonlinear terms lead to the instability processes of interest. A full discussion of the $\mathbf{H}_{\text{eff}}(\mathbf{r},t)$ field is presented in Ch. 3.

Equation (2.1) in combination with the right-hand rule shows that the magnetization precesses in a counterclockwise direction. This natural counterclockwise precession of the magnetization is termed Larmor precession. Similarly, a clockwise precession of the magnetization is termed anti-Larmor precession. If the precession of the magnetization is not circular but rather elliptical, the precession can be described simply in terms of both Larmor and anti-Larmor circular components.

Generally the magnetization for a given normal mode varies spatially over the sample and harmonically in time with a precessional frequency ω_k. This is spin wave mode precession. The wave vector $\mathbf{k}$ describes the spatial variation of the magnetization over the sample. The uniform mode is a specific case of spin wave mode precession. Here, the magnetization varies harmonically in time with a precessional frequency ω_0 and has a wave number of zero.

Notice that there is no dissipative term in the torque equation. Without a dissipative term, the magnetization never decays to equilibrium and continues to precess at ω_0, for the uniform mode case. A loss term can be added to the magnetic torque equation of motion to provide a means to describe the decay of the magnetization to equilibrium. The relaxation of the uniform mode depends on the intrinsic properties of the sample such as magnon-electron interactions and extrinsic contributions such as inhomogeneities. The term magnon refers to the quantum mechanical analog of a spin wave.

A microwave pumping field can be used to drive the uniform mode precession. For a microwave pumping frequency far from ω_0, very little energy is coupled to the precessing magnetization. When the microwave pumping frequency is equal to ω_0, energy is coupled into the precessing magnetization. This is a resonance response. The magnetization precession angle increases as the microwave power is increased until one reaches the spin wave instability threshold.

2.2 LOW POWER FERROMAGNETIC RESONANCE RESPONSE

For a low power ferromagnetic resonance measurement, the microwave pumping field $\mathbf{h}_p(t)$ is typically quite small and is applied perpendicular to the external static magnetic field $\mathbf{H}$. As mentioned in Ch. 1, ferromagnetic resonance can be studied by frequency or field-swept measurements. For the first measurement the $\mathbf{H}$ is kept at a fixed value and the precessional frequency is at a given $\omega_0(H)$. The microwave frequency ω_p is swept over a range that includes ω_0 and the absorbed power is measured. For frequencies off of ω_0 the absorbed power is very small, as the magnetization decays to thermal equilibrium, but at ω_0 the absorbed power is large, as the magnetization is harmonically driven at resonance.

For the field-swept measurement, the microwave pumping frequency is fixed, the static magnetic field is swept over a particular range, and the absorbed power is measured. When the static field is such that the $\omega_p = \omega_0(H)$ criteria is met, then the absorbed power is large and the magnetization is again driven harmonically at resonance. This static field is the ferromagnetic resonance field H_{res}.

Figure 2.1 shows an example FMR response profile for a 104 nm film thin Permalloy film at a microwave frequency of 9.11 GHz. The graph shows data on the cavity voltage reflection coefficient ρ vs. H. The reflection coefficient is a measure of loss and is given by $\rho = (P_{\text{ref}} / P_{\text{in}})^{1/2}$ where P_{ref} is the power reflected from the sample and P_{in} is the incident power on the sample. The voltage is proportional to the square root of the power. The $\mathbf{H}$ and $\mathbf{h}_p(t)$ fields were in-plane and mutually perpendicular at a coupling angle of $\phi = 90^{\circ}$, as shown in the diagram inset. The black dot marks the FMR field point at $H_{\text{res}} = 830$ Oe. The FMR field swept linewidth ΔH_{FMR} indicated in the plot is defined to be the distance, in field

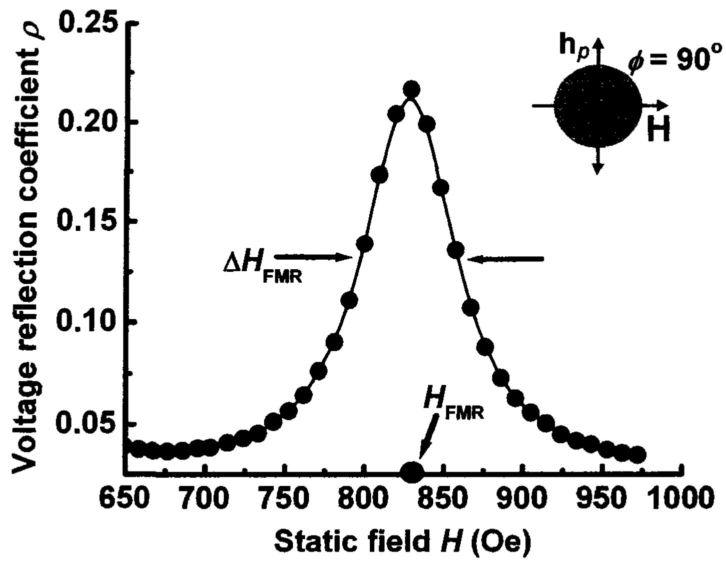

FIG. 2.1. Voltage reflection coefficient ρ vs. static field H for the 104 nm thin film and a microwave frequency of 9.11 GHz. The FMR peak is $H_{\mathrm{FMR}} = 830$ Oe and the FMR linewidth is $\Delta H_{\mathrm{FMR}} = 59$ Oe, as indicated. The H and microwave pumping field h_p are in-plane and mutually perpendicular at $\phi = 90^{\circ}$, as shown in the inset.

units, between the half-power points of the absorption. Recall that Fig. 2.1 shows the loss in terms of ρ and not power. The ΔH_{FMR} is then not located at exactly the half-way point on the profile. In this case $\Delta H_{\mathrm{FMR}} = 59$ Oe.

As noted, the low power FMR peak in Fig. 2.1 is at 830 Oe and the half power linewidth is about 59 Oe. This peak is the basic FMR response where the $\omega_p = \omega_0(H)$ criteria is met. The broadening is due to the loss or dissipative mechanisms which damp the FMR response.

The next section discusses the change to the FMR profile as the microwave power is increased. Other high power phenomena that occur off of the FMR resonance profile and for field configurations where the coupling angle ϕ between the $\mathbf{H}$ and $\mathbf{h}_p(t)$ fields is varied from perpendicular to parallel are also discussed.

2.3 HIGH POWER FERROMAGNETIC RESONANCE

Recall that the torque equation is comprised of a coupled set of nonlinear equations. At high power the nonlinear terms lead to instability processes. Chapter 3 provides the theoretical analysis of these nonlinear terms. This section gives a qualitative discussion of the high power FMR phenomena that corresponds to the instability processes and shows example high power FMR data. This section is separated into four separate subsections. Each subsection presents a different type of high power effect.

2.3.1 RESONANCE SATURATION RESPONSE

At low microwave power levels, the response of the dynamic magnetization to an increase in power is linear. For high microwave power levels, above some particular threshold power, coupling of the energy from the microwave pumping field to the spin wave modes results in a nonlinear response. For resonance saturation, the energy from the microwave pumping field is indirectly coupled through the uniform mode into the spin wave modes at the microwave pumping frequency.

Figure 2.2 shows the effect of high power on the FMR response and the loss for fields below the FMR peak for a 104 nm thin Permalloy film. The graph shows data on ρ vs. H for peak input microwave power levels to the cavity P_{in} of 0.25 and 22 W, as indicated. The microwave pumping frequency was 9.58 GHz. The **H** and $\mathbf{h}_p(t)$ fields were in-plane and mutually perpendicular at $\phi = 90^{o}$, as shown in the diagram inset. The low power FMR peak is at 909 Oe, as labeled. The RS and SA labels indicate, respectively, the resonance saturation (RS) and subsidiary absorption (SA) responses. The subsidiary absorption region will be considered in subsection

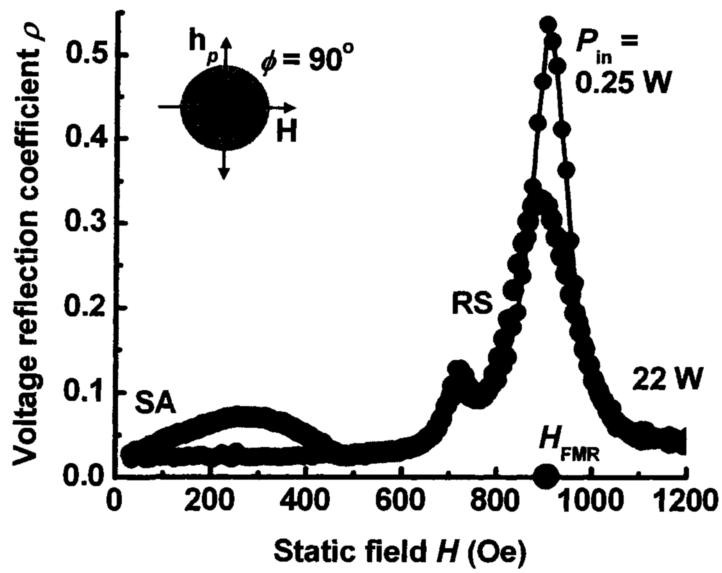

FIG. 2.2. Voltage reflection coefficient ρ vs. H for the 104 nm thin film and a microwave frequency of 9.58 GHz. The symbols show data for different P_{in} values, as indicated. The RS and SA labels denote the resonance saturation and subsidiary absorption responses, respectively. The black dot marks the H_{FMR} field. The **H** and $\mathbf{h}_p(t)$ fields were in-plane and mutually perpendicular at $\phi = 90^{o}$, as shown in the inset.

2.3.2.

As previously noted, the low power FMR peak in Fig. 2.2 is at 909 Oe and the half power linewidth is about 95 Oe. The increase in the H_{FMR} field in Fig. 2.2 compared to Fig. 2.1 is the result of the increase in the microwave pumping frequency from 9.11 to 9.58 GHz. The linewidth for the low power FMR profile in Fig. 2.2 is notably larger than in Fig. 2.1 for the same sample. This is due to sample loading on the cavity which distorts the FMR profile. The problem of cavity loading and the resolution to this problem are discussed in Ch. 5. The true linewidth for this sample is 59 Oe. The peak on the low field side of FMR corresponds to a standing spin wave mode. Standing spin wave modes were studied in depth in the 1960's by Pascard and Berteaud (1964), Pascard (1965), and others. These modes are not directly related to the nonlinear processes of interest here. As such, the scope of this work does include standing spin wave modes.

The qualitative changes in the profiles as P_{in} is increased provide an indication of the overall nonlinear response. The profile for $P_{in} = 22$ W is broader, lower in amplitude, and asymmetric, relative to the low power profile. The asymmetry amounts to a shift of the profile to lower fields and the development of a low field shoulder.

The drop in amplitude and the broadening of the FMR peak with increasing power is the basic resonance saturation response. This nonlinear effect occurs for powers well below those expected from only simple FMR considerations. As mentioned, the change in the ρ coefficient with an increase of power is not a continuous effect but rather a threshold effect. Calibrated data on the ρ vs. the microwave magnetic field amplitude h_p, presented in Ch. 5, will show that the change in the ρ coefficient occurs more or less abruptly at some threshold h_{crit} value.

The idea is that energy is coupled from the driven uniform mode into parametrically pumped spin waves at frequencies equal to the pump frequency at some power dependent rate G_k. At the point at which G_k exceeds the relaxation rate of the spin waves, taken as η_k, the occupation numbers of the spin waves increase above thermal levels and there is an abrupt change in loss over the FMR profile. The decrease in loss at FMR occurs as the uniform mode precession angle locks up and energy is pumped from the uniform mode into the spin wave modes. The broadening of the FMR profile occurs as the occupation numbers of the spin waves increase above thermal levels.

It is important to note that the actual threshold is tied closely to the low power FMR precession amplitude. The corresponding threshold field is usually smallest at the FMR peak where the precession angle is the largest. The shift to low field and the development of the low field shoulder with increasing power is the manifestation of a foldover effect for metal films. This foldover effect is discussed in Ch. 5 and 6.

2.3.2 SUBSIDIARY ABSORPTION RESPONSE

For subsidiary absorption, as for resonance saturation, energy from the h_p field is indirectly coupled into the spin wave modes through the uniform mode. Here, however, energy is parametrically pumped into spin waves at one half the microwave pumping frequency. Recall that the SA in Fig. 2.2 indicates the subsidiary absorption response for the 104 nm thin Permalloy film.

Figure 2.3 shows ρ vs. H data for P_{in} of 0.35, 10, 23, and 28 W, as indicated. The data are for the 104 nm thin Permalloy film at a $\omega_p / 2\pi = 9.58$ GHz. The $\mathbf{H}$ and $\mathbf{h}_p(t)$ fields were in-plane and mutually perpendicular at $\phi = 90^\circ$, as shown in

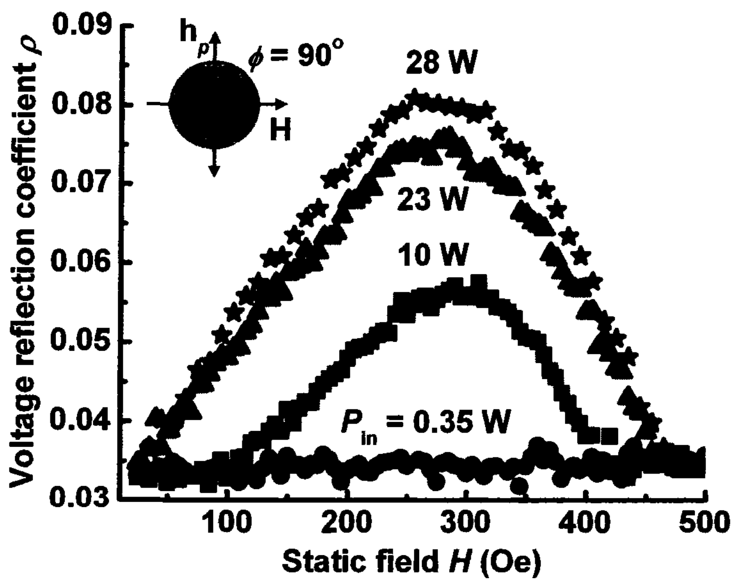

FIG. 2.3. Voltage reflection coefficient ρ vs. H for the 104 nm thin Permalloy film and a microwave frequency of 9.58 GHz. The symbols show data for different P_{in} values, as indicated. The H field and the h_p field were in-plane and mutually perpendicular at $\phi = 90^\circ$, as shown in the inset.

the diagram inset. The field span covers only the region of the SA response in Fig. 2.2.

The qualitative changes in the profiles as P_{in} is increased provide an indication of the overall nonlinear response. The high power profiles show somewhat broad peaks for fields well below the main FMR peak. As the P_{in} is increased to larger levels, the high power profile increases in amplitude and broadens. The increase in loss with an increase in power is the basic subsidiary absorption response. The subsidiary absorption peak at low fields is a spin wave effect. It cannot be explained from simple FMR considerations only. As with the resonance saturation response, the change in the ρ coefficient with an increase of P_{in} is not a continuous effect, but occurs at a particular threshold value.

The basic idea of the subsidiary absorption response is the same as for resonance saturation with the exception that the energy is pumped into spin waves at *half* the microwave pumping frequency. Above some threshold value the occupation numbers of spin waves at half the pumping frequency increase. This corresponds to an increase in loss over the low H range.

2.3.3 PARALLEL PUMPING RESPONSE

The parallel pumping response is a nonlinear phenomenon that occurs when the H field is parallel to the h_p field. For this configuration, the h_p field cannot drive the uniform mode precession and no FMR response to lowest order is possible. However, a direct coupling of energy from the microwave pumping field into the spin wave modes is possible because of the elliptical precession of the magnetization, termed spin wave ellipticity. The elliptical precession is due to dipole-dipole interactions between the neighboring spins.

For a magnetization that is constant in magnitude the elliptical precession results in a wobble of the component of magnetization that is parallel to the $\mathbf{h}_p(t)$. The wobble in the parallel magnetization component has a $e^{i2\omega_k t}$ time dependence, where ω_k is the precessional frequency of the spin wave. Energy is directly coupled into spin wave modes from the h_p field when the microwave pumping frequency is twice the spin wave precessional frequency, that is, one has $\omega_p = 2\omega_k$.

Parallel pumping is also a threshold effect. As the P_{in} level is increased, energy is parametrically pumped directly into spin waves at *half* the microwave pump frequency. Due to relaxation the occupation numbers of the spin waves reside at thermal levels until one reaches some particular threshold power. Above this threshold power, the energy coupled into the spin wave modes exceeds the rate at which the energy can be lost due to relaxation and the occupation numbers of the spin waves increase above thermal levels. This corresponds to an increase in loss for low H fields in the same general field range as for subsidiary absorption.

No results were obtained for a pure parallel pumping response. None of the Permalloy films of interest showed a parallel pumping response for the power level available. However, the parallel pumping process does contribute to the oblique pumping process that is discussed in the next subsection.

2.3.4 OBLIQUE PUMPING RESPONSE

For both the parallel pumping and subsidiary absorption responses, energy is parametrically pumped into spin wave modes at *half* the microwave pump frequency and the responses are in the same general H range. As mentioned above, the parallel pumping and subsidiary absorption responses are for the parallel and perpendicular field configurations, respectively. For oblique angles between the parallel and perpendicular configurations both processes contribute to the response. The oblique pumping response is a combination of the subsidiary absorption and parallel pumping responses weighted by the ϕ angle.

Figure 2.4 shows data on ρ vs. H for the 104 nm thin Permalloy film and a pumping frequency of 9.58 GHz. The data represented by the blue circles and red triangles are for P_{in} of 0.25 and 22 W, respectively. The static and microwave fields

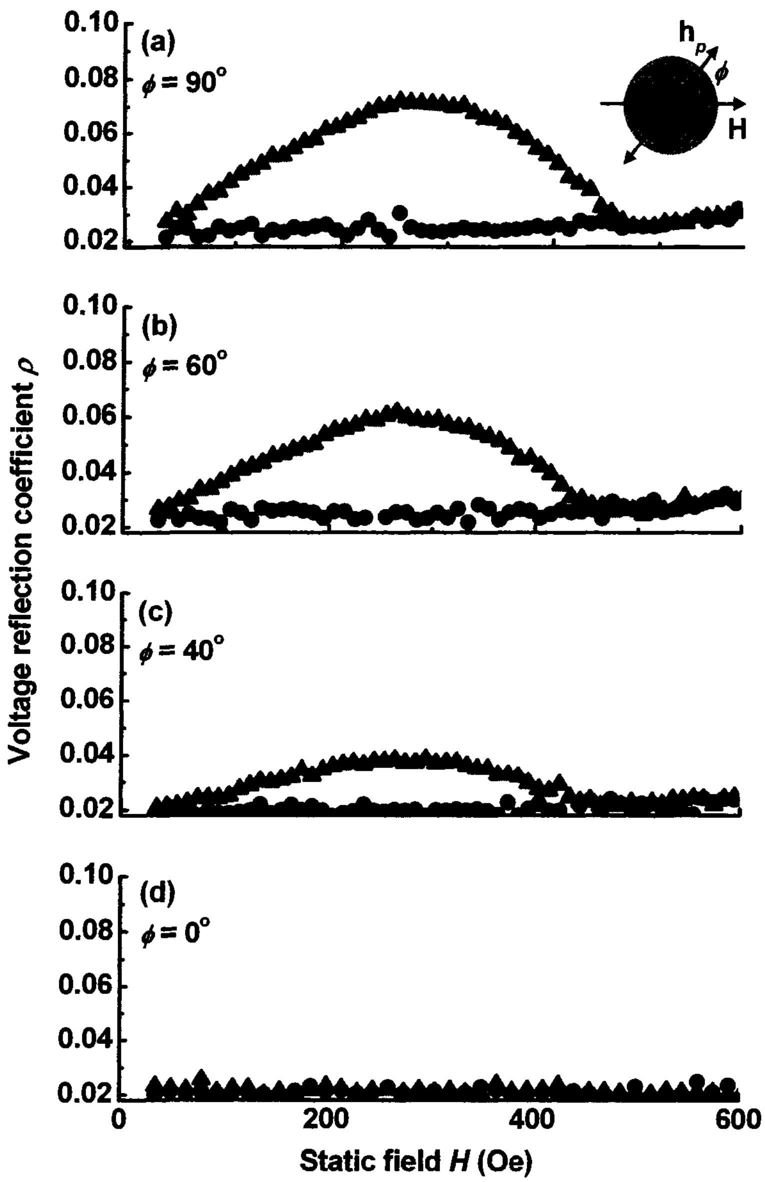

FIG. 2.4. Voltage reflection coefficient ρ vs. H for the 104 nm thin film and a microwave frequency of 9.58 GHz. The angles between the H field and the h_p field are as indicated and the fields are in the film plane. The field configuration is shown in the diagram inset. The data represented by blue circles and red triangles are for peak input microwave power levels to the cavity P_{in} of 0.25 and 22 W, respectively.

were in-plane. Graphs (a), (b), (c), and (d) are for ϕ angles of 90°, 60°, 40°, and 0°, respectively. The field configuration is shown in the diagram inset.

The qualitative changes in the profiles as P_{in} is increased again provide an indication of the overall nonlinear response. In graphs (a), (b), and (c) the profiles for $P_{in} = 22$ W show an increase in amplitude. As the coupling angle is decreased, the amplitude of the profiles for the same P_{in} level decreases. At $\phi = 0^{\circ}$ there is no measurable increase in loss. It is important to mention that for P_{in} as high as 800 W no parallel pumping response was observed for any of the films.

An increase in loss is the basic subsidiary absorption response and, hence the oblique pumping response, as well. The change in ρ with increasing power at a fixed field is a threshold effect that depends on both the subsidiary absorption and parallel pumping processes. Oblique pumping provides a unique means to compare the subsidiary absorption and parallel pumping processes.

It is important to emphasize that the results discussed above are qualitative and are for steady state responses. All high power FMR curves are obtained at full coupling $\phi = 90^{\circ}$ and there is no one-to-one correspondence between the input power and the microwave field amplitude over a give profile. However, this qualitative study provides a practical background for the theoretical analysis of spin wave instability theory in the next chapter.

REFERENCES

[Ashcroft and Mermin (1976)] N. W. Ashcroft and N. D. Mermin, *Solid State Physics* (Harcourt, Inc., 1976).

[Pascard and Berteaud (1964)] H. Pascard and A. Berteaud, C. R. Acad. Sc. Paris **258**, 2275 (1964).

[Pascard (1965)] H. Pascard, Ph.D. dissertation, University of Paris, Paris, France (1965).

[Weast and Astle (1982)] R. C. Weast and M. J. Astle, *CRC Handbook of Chemistry and Physics 63rd ed*, (CRC Press, Inc., 1982).

FIRST AND SECOND ORDER SPIN WAVE INSTABILITY THEORY

INTRODUCTION

The focus of this chapter is on the analysis of first and second order spin wave instability. An introduction to the uniform mode dynamics is given and first and second order spin wave instability (SWI) theory, suitably modified for thin metal films, is developed. The formalism used to modify the SWI theory for a thin film is based on unpublished calculations by Dr. Pavol Krivosik [Krivosik (2007)]. The theory for subsidiary absorption and resonance saturation was outlined in An *et al.* (2004) and Olson *et al.* (2007), respectively.

Section 3.1 establishes the sample geometry in the precessional reference frame and a working equation for the total effective field. Section 3.2 presents the solution to the linearized torque equation of motion with phenomenological Gilbert damping included. The spin wave dispersion relation and other important equations that pertain to linear spin waves are obtained. This analysis is used to develop the necessary uniform mode equations. The ferromagnetic resonance (FMR) frequency, along with other important uniform mode expressions, is obtained.

Section 3.3 uses the formalism to develop working equations for the first and second order SWI processes. Finally, Sec. 3.4 presents example calculations that demonstrate the SWI theory. These results are utilized in Ch. 6 and 7 for the analysis of the resonance saturation and oblique pumping experimental results.

3.1 TOTAL EFFECTIVE MAGNETIC FIELD AND SAMPLE GEOMETRY

Ferromagnetic materials [Ashcroft and Mermin (1976)] are magnetically ordered substances that have strong internal interactions between the microscopic localized magnetic moments at the lattice sites of the material. The intrinsic properties of the electrons are responsible for these localized magnetic moments. For a ferromagnetic material these localized moments all align in the same direction. Classically a continuum approximation allows one to study the dynamic magnetic processes macroscopically. This classical approach is used for this work. It is important to note that spin wave instability theory has been recast in various forms by Schloemann *et al.* (1963), Schloemann (1959), Patton (1979), Chen and Patton (1994), and Nazarov *et al.* (2002).

The starting point for the analysis is the magnetic torque equation of motion [Sparks (1964)] for the total magnetization $\mathbf{M}(\mathbf{r},t)$, as introduced in Ch. 2. The equation of motion is based on the magnetic torque model and was first used by Landau and Lifshitz (1935). The magnetic torque equation of motion is

$$\frac{d\mathbf{M}(\mathbf{r},t)}{dt} = -|\gamma|\mathbf{M}(\mathbf{r},t)\times\mathbf{H}_{\text{eff}}(\mathbf{r},t) \ , \tag{3.1}$$

where $\mathbf{H}_{\text{eff}}(\mathbf{r},t)$ is the total effective field. A working equation for the $\mathbf{H}_{\text{eff}}(\mathbf{r},t)$ field [Patton (1968)] is developed in this section.

Figure 3.1 shows the sample geometry in the $(\hat{\mathbf{x}},\hat{\mathbf{y}},\hat{\mathbf{z}})$ precession frame where, $\hat{\mathbf{x}}-\hat{\mathbf{z}}$ are the in-plane coordinates and $\hat{\mathbf{y}}$ is the normal to plane direction. The sample is taken to be an isotropic thin film and infinitely large in the $\hat{\mathbf{x}}-\hat{\mathbf{z}}$ direction. The uniform external static magnetic field $\mathbf{H}$ and the equilibrium position of the static magnetization, in the $\hat{\mathbf{z}}$-direction, and the linearly polarized uniform

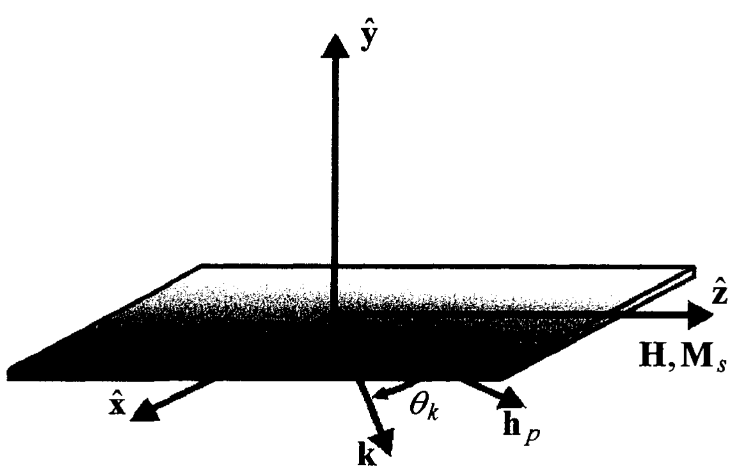

FIG. 3.1. The precession $(\hat{\mathbf{x}},\hat{\mathbf{y}},\hat{\mathbf{z}})$ coordinate frame and the orientation of the coordinate system to the film. The external static magnetic field $\mathbf{H}$ and saturation magnetization $\mathbf{M}_s$ coincide with the $\hat{\mathbf{z}}$-axis. The microwave pumping field $\mathbf{h}_p$ is at an in-plane angle ϕ. The wave vector $\mathbf{k}$ is in film plane at an angle θ_k.

microwave pumping field $\mathbf{h}_p(t)$ are constrained to be in the plane of the film. The angle between $\mathbf{H}$ and $\mathbf{h}_p(t)$ is ϕ.

The $\mathbf{M}(\mathbf{r},t)$ is separated into its static and dynamic components as

$$\mathbf{M}(\mathbf{r},t) = M_s\hat{\mathbf{z}} + \mathbf{m}(\mathbf{r},t) \quad , \tag{3.2}$$

where $\mathbf{m}(\mathbf{r},t)$ is the dynamic magnetization and $M_s\hat{\mathbf{z}}$ is termed the saturation magnetization and is the static component of the total magnetization. The $\mathbf{H}_{\text{eff}}(\mathbf{r},t)$ field is comprised of four terms [Patton (1979)] and is given by

$$\mathbf{H}_{\text{eff}}(\mathbf{r},\mathrm{t}) = \mathbf{H} + \mathbf{h}_p(t) + \mathbf{H}_D(\mathbf{r},\mathrm{t}) + \mathbf{h}_{\text{ex}}(\mathbf{r},\mathrm{t}) \quad , \tag{3.3}$$

where $\mathbf{H}_D(\mathbf{r},t)$ is the dipolar or Maxwellian field due to the sample shape and magnetic dipole-dipole interactions. The $\mathbf{H}_D(\mathbf{r},t)$ field consists of a static demagnetizing field $\mathbf{H}_D$ and a dynamic dipole field $\mathbf{h}_D(\mathbf{r},t)$. The $\mathbf{h}_{\text{ex}}(\mathbf{r},t)$ is the effective exchange field that corresponds to the exchange interaction. The $\mathbf{h}_{\text{ex}}(\mathbf{r},t)$ field is not a Maxwellian field. Notice that there is no anisotropy term included in the $\mathbf{H}_{\text{eff}}(\mathbf{r},t)$. As mentioned in Ch. 2, the anisotropy for Permalloy is small, in the 5 – 10 Oe range. This small field may be neglected for the purposes of this work. The in-plane pumping field is separated into its vector components with explicit time dependence as

$$\mathbf{h}_p(t) = h_p\left(\cos\phi\hat{\mathbf{x}} + \sin\phi\hat{\mathbf{z}}\right)\cos\left(\omega_p t\right) \quad , \tag{3.4}$$

where ω_p is the frequency of the microwave pumping field and h_p is the pumping field amplitude.

The dynamic magnetization is expanded as

$$\mathbf{m}(\mathbf{r},t) = \sum_k \mathbf{m}_k(t) e^{i(\mathbf{k}\cdot\mathbf{r})} \quad , \tag{3.5}$$

where $\mathbf{m}_0(t)$ is the uniform mode response part of the steady state dynamic magnetization response where $\mathbf{k} = 0$, and the $\mathbf{m}_k(t) e^{i(\mathbf{k}\cdot\mathbf{r})}$ terms denote quasi-plane-wave spin wave excitations with a wave vector $\mathbf{k}$.

For this work, the thin film approximation developed and applied by Harte (1968), Arias and Mills (1999), and McMichael and Krivosik (2004), is used to find closed expressions for the critical threshold field amplitudes. In this approximation, the dynamic magnetization is taken as uniform across the film thickness. This approximation corresponds to the lowest order mode analysis in Vendik *et al.* (1977). Without these simplifications a general nonlocal exchange analysis through numerical methods [Wames and Wolfram (1970)] or Green's function analysis [Kalinikos and Slavin (1986)] is required. In this work, the thin film approximation is termed the Harte approximation.

The $\mathbf{H}_D(\mathbf{r},t)$ field is discussed first. Recall that this field consists of a uniform static component, the usual demagnetizing field, and a dynamic dipole component. The demagnetizing field is generated by the $\mathbf{M}_s$ for a finite sample and is related to the sample shape. For a thin film that is taken to be infinitely large in the in-plane directions and that is magnetized in the film plane the demagnetizing field is zero and only the $\mathbf{h}_D(\mathbf{r},t)$ field remains. In the magnetostatic approximation [Jackson (1999)] this dynamic component is given by

$$\mathbf{h}_D(\mathbf{r},t) = -\int \mathrm{d}^3 r' \frac{\nabla' \mathbf{m}(\mathbf{r},t)}{|\mathbf{r}-\mathbf{r}'|} \quad . \tag{3.6}$$

For the specific case of a thin film where the Harte approximation is applicable, the dynamic Maxwellian field can be Fourier expanded as

$$\mathbf{h}_D(\mathbf{r},t) = \sum_k \mathbf{h}_{D,k}(t) \mathrm{e}^{i(\mathbf{k}\cdot\mathbf{r})} \quad . \tag{3.7}$$

The $\mathbf{h}_{D,k}(t)$ field includes the uniform dipole field that corresponds to $\mathbf{k}=0$ and the nonuniform dipole field that corresponds to $\mathbf{k}\neq 0$. If it is assumed that the dynamic magnetization has no $\hat{\mathbf{y}}-$dependence, as in the Harte approximation noted above, $\mathbf{h}_{D,k}(t)$ becomes

$$\mathbf{h}_{D,k}(t) = -4\pi\left[(1-N_k)\frac{\mathbf{kk}}{k^2} + N_k \hat{\mathbf{y}}\hat{\mathbf{y}}\right]\cdot\mathbf{m}_k(t) \quad , \tag{3.8}$$

where the wave vector $\mathbf{k}$ is constrained to the film plane according to $\mathbf{k} = k_x\hat{\mathbf{x}} + k_z\hat{\mathbf{z}} = k[\sin\theta_k\hat{\mathbf{x}} + \cos\theta_k\hat{\mathbf{z}}]$, θ_k is the angle between the in-plane $\mathbf{k}$ vector and the $\hat{\mathbf{z}}-$axis, and the effective demagnetizing factor N_k is given by

$$N_k = \frac{1-\mathrm{e}^{-kd}}{kd} \quad , \tag{3.9}$$

where d is the film thickness. Equation (3.8) and (3.9) comprise the Harte approximation.

Two limiting cases are taken to examine the demagnetizing factor N_k more closely. Figure 3.2(a) shows a graph of N_k vs. kd based on Eq. (3.9). From this

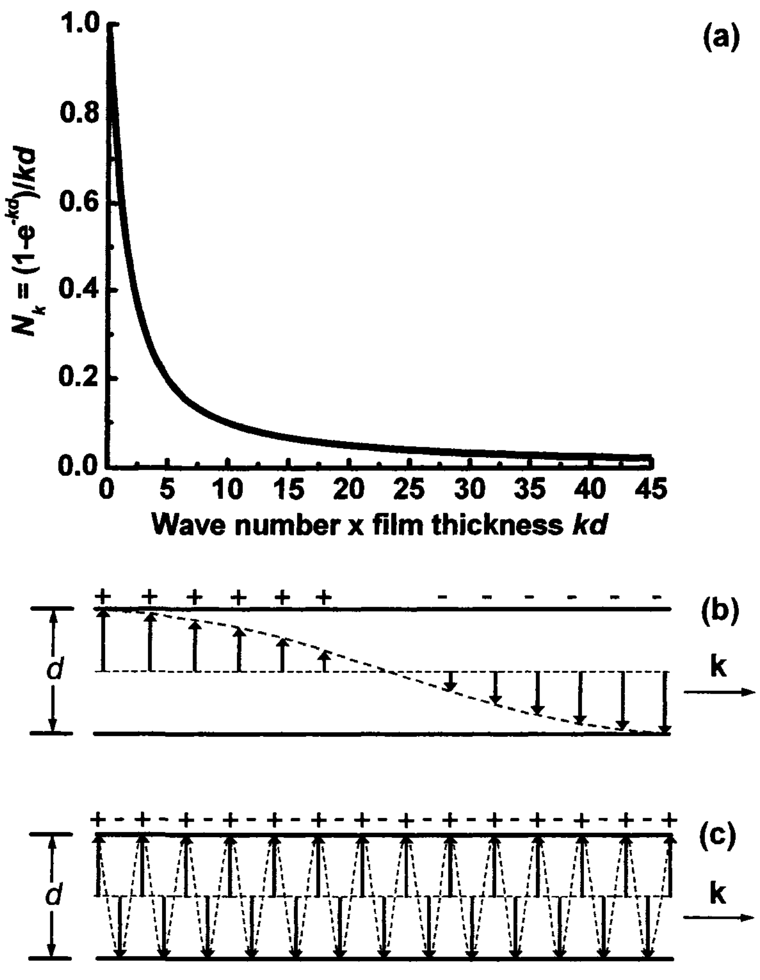

FIG. 3.2. Limiting cases of the effective demagnetizing factor N_k. Graph (a) is shows the function N_k vs. kd. Diagram (b) shows a schematic representation of a spin wave mode in the film for the limiting case where $kd \to 0$. Diagram (c) shows a schematic representation of a spin wave mode in the thin film for the limiting case where $kd \to \infty$.

figure, one can see that in the limit $kd \to 0$, the effective demagnetizing factor goes to one, while in the limit $kd \to \infty$, the effective demagnetizing factor goes to zero. These limiting cases can be applied to Eq. (3.8). For $kd \to 0$, the resultant dipolar field is given by $\mathbf{h}_{D,0} = -4\pi m_{0,y}\hat{\mathbf{y}}$, where $m_{0,y}\hat{\mathbf{y}}$ is the normal component of $\mathbf{m}_0$. This equation describes a dipolar field that is oriented normal to the film plane. Figure 3.2(b) shows a schematic representation of a spin wave mode in a film that roughly corresponds to $\mathbf{h}_{D,0} = -4\pi m_{0,y}\hat{\mathbf{y}}$. This figure shows that the wavelength of the spin wave is much larger than the film thickness.

For the $kd \to \infty$ limit of Eq. (3.8), one obtains $\mathbf{h}_{D,k} \approx -4\pi(\mathbf{kk}/k^2)\bullet\mathbf{m}_k$. Figure 3.2(c) shows a schematic representation of a spin wave mode in a film that roughly corresponds to $\mathbf{h}_{D,k} \approx -4\pi(\mathbf{kk}/k^2)\bullet\mathbf{m}_k$. In this limit, the wavelength is much smaller than the film thickness.

The remaining term in $\mathbf{H}_{\text{eff}}(\mathbf{r},t)$ is the effective exchange field $\mathbf{h}_{\text{ex}}(\mathbf{r},t)$. In the continuum approximation, the effective exchange field can be written as

$$\mathbf{h}_{\text{ex}}(\mathbf{r},t) = \frac{D}{M_s}\nabla^2\mathbf{m}(\mathbf{r},t) \quad , \tag{3.10}$$

where D is the exchange stiffness parameter [Patton (1975)]. The $\mathbf{h}_{\text{ex}}(\mathbf{r},t)$ can be Fourier expanded as

$$\mathbf{h}_{\text{ex}}(\mathbf{r},t) = \sum_k \mathbf{h}_{\text{ex},k}(t)e^{i(\mathbf{k}\bullet\mathbf{r})} \quad , \tag{3.11}$$

where $\mathbf{h}_{\mathrm{ex},k}(t)$ is given by

$$\mathbf{h}_{\mathrm{ex},k}(t) = -\frac{D}{M_s} k^2 \mathbf{m}_k(t) \quad . \tag{3.12}$$

The effective field terms from Eq. (3.8) and (3.12) can now be collected and inserted into Eq. (3.3). The working equation for the effective field is then obtained as

$$\begin{aligned} \mathbf{H}_{\mathrm{eff}}(\mathbf{r},t) = {} & H\hat{\mathbf{z}} + h_p\left(\cos\phi\hat{\mathbf{x}} + \sin\phi\hat{\mathbf{z}}\right)\cos\left(\omega_p t\right) \\ & -4\pi\sum_k \hat{\mathbf{N}}\cdot\mathbf{m}_k(t)\mathrm{e}^{i(\mathbf{k}\cdot\mathbf{r})} \quad , \end{aligned} \tag{3.13}$$

where $\hat{\mathbf{N}}$ is a combination of an exchange term and an effective $\mathbf{k}$-dependent demagnetizing term given by

$$\begin{aligned} \hat{\mathbf{N}} = {} & -\frac{Dk^2}{4\pi M_s}\hat{\mathbf{I}} \\ & + \begin{pmatrix} [1-N_k]\sin^2\theta_k & 0 & [1-N_k]\sin\theta_k\cos\theta_k \\ 0 & N_k & 0 \\ [1-N_k]\sin\theta_k\cos\theta_k & 0 & [1-N_k]\cos^2\theta_k \end{pmatrix} . \end{aligned} \tag{3.14}$$

The effective demagnetizing term depends on the film boundaries and is used to find the dynamic demagnetization fields. The instantaneous dynamic magnetization has some small component in a particular direction. The sample responds to this with a small demagnetization field.

3.2 LINEAR SPIN WAVE MODE ANALYSIS

This section focuses on the linear terms in the magnetic torque equation. These lead to important information on spin waves and the uniform mode magnetization. The uniform mode magnetization is discussed Sec. 3.3. Spin wave instability results from the analysis of the nonlinear terms and is discussed in Sec. 3.4.

The torque equation of Eq. (3.1) does not include a relaxation term. A phenomenological Gilbert damping [Gilbert (1955)] may be added to provide for the relaxation of the total magnetization to static equilibrium. The torque equation with Gilbert damping is written as

$$\begin{aligned}\frac{d\mathbf{M}(\mathbf{r},t)}{dt} &= -|\gamma|\mathbf{M}(\mathbf{r},t)\times\mathbf{H}_{\text{eff}}(\mathbf{r},t)\\ &\quad+\frac{\alpha}{M_s}\mathbf{M}(\mathbf{r},t)\times\frac{d\mathbf{M}(\mathbf{r},t)}{dt}\quad,\end{aligned}\tag{3.15}$$

where α is the Gilbert damping parameter. Note that the Eq. (3.15) still conserves the total magnetization. The Gilbert form of the damping describes a decay of the precession of the magnetization to equilibrium that is driven by the instantaneous component of the $d\mathbf{M}(\mathbf{r},t)/dt$ that is perpendicular to the trajectory of the precession. Gilbert damping, although phenomenological in nature, is closely related to the magnon-electron relaxation process [Kambersky and Patton (1975)]. This connection is important for the results of both the resonance saturation and oblique pumping analyses, as presented in Ch. 6 and 7.

If the magnetization $\mathbf{M}(\mathbf{r},t)$ from Eq. (3.2) and the total effective magnetic field $\mathbf{H}_{\text{eff}}(\mathbf{r},t)$ of Eq. (3.3) are substituted into Eq. (3.15), one obtains a set of coupled equations in $\dot{\mathbf{m}}(\mathbf{r},t)$ given by

$$\begin{aligned}\dot{\mathbf{m}}(\mathbf{r},t) &= -|\gamma|\left[M_s\hat{\mathbf{z}}+\mathbf{m}(\mathbf{r},t)\right] \\ &\quad \times\left[H\hat{\mathbf{z}}+\mathbf{h}_p(t)+\mathbf{h}_D(\mathbf{r},t)+\mathbf{h}_{\text{ex}}(\mathbf{r},t)\right] \\ &\quad +\frac{\alpha}{M_s}\left[M_s\hat{\mathbf{z}}+\mathbf{m}(\mathbf{r},t)\right]\times\dot{\mathbf{m}}(\mathbf{r},t) \ .\end{aligned} \tag{3.16}$$

As mentioned, the analysis for this section is limited to the linearized torque equation of motion and the small signal limit where $|\mathbf{m}(\mathbf{r},t)| \ll M_s$ is satisfied.

3.2.1 FREE RESPONSE

This section considers the special case for $\mathbf{h}_p(t)=0$. This is called the free response. In this limit, the linearized version of Eq. (3.16) is

$$\begin{aligned}\dot{\mathbf{m}}_k(t) &= -|\gamma|\hat{\mathbf{z}}\times\left\{M_s\left[\mathbf{h}_{D,k}(t)+\mathbf{h}_{\text{ex},k}(t)\right]-H\mathbf{m}_k(t)\right\} \\ &\quad +\alpha\hat{\mathbf{z}}\times\dot{\mathbf{m}}_k(t) \ .\end{aligned} \tag{3.17}$$

This equation can be simplified by the introduction of new scalar complex amplitudes

$$a_k(t)=\frac{1}{M_s}\left[m_{k,x}(t)+im_{k,y}(t)\right] \tag{3.18}$$

and

$$a_{-k}^{*}(t)=\frac{1}{M_s}\left[m_{k,x}(t)-im_{k,y}(t)\right] \ . \tag{3.19}$$

After some algebra, Eq. (3.17) then takes the form

$$-i\begin{pmatrix}\dot{a}_k(t)\\ \dot{a}_{-k}^{*}(t)\end{pmatrix}=\begin{pmatrix}A_k & B_k\\ -B_k & -A_k\end{pmatrix}\begin{pmatrix}a_k(t)\\ a_{-k}^{*}(t)\end{pmatrix}+\alpha\begin{pmatrix}0 & -1\\ 1 & 0\end{pmatrix}\begin{pmatrix}\dot{a}_k(t)\\ \dot{a}_{-k}^{*}(t)\end{pmatrix} \ , \tag{3.20}$$

with

$$A_k=\omega_H+|\gamma|Dk^2+\frac{\omega_M}{2}\left[(1-N_k)\sin^2\theta_k+N_k\right] \ , \tag{3.21}$$

and

$$B_k=\frac{\omega_M}{2}\left[(1-N_k)\sin^2\theta_k-N_k\right] \ . \tag{3.22}$$

The $\omega_H=|\gamma|H$ and $\omega_M=|\gamma|4\pi M_s$ terms simply express the H and $4\pi M_s$, respectively, in frequency units. The B_k term depends only on the dipole-dipole interaction. For the special case of an in-plane magnetized isotropic film, B_k is real. In general B_k is complex.

If the $\dot{a}_k(t)$ and $\dot{a}_{-k}^{*}(t)$ terms in Eq. (3.20) are collected and the equation is simplified [Arfken and Weber (2001)], one obtains

$$-i\begin{pmatrix}\dot{a}_k(t)\\ \dot{a}_{-k}^{*}(t)\end{pmatrix}=\frac{1}{1+\alpha^2}\begin{pmatrix}A_k(1+i\alpha) & B_k(1+i\alpha)\\ -B_k(1-i\alpha) & -A_k(1-i\alpha)\end{pmatrix}\begin{pmatrix}a_k(t)\\ a_{-k}^{*}(t)\end{pmatrix} \ . \tag{3.23}$$

For small damping $\alpha \ll 1$ Eq. (3.20) is given by

$$-i\dot{a}_k(t) = A_k(1+i\alpha)a_k(t) + B_k(1+i\alpha)a_{-k}^*(t) \tag{3.24}$$

and

$$-i\dot{a}_{-k}^*(t) = -A_k(1-i\alpha)a_{-k}^*(t) - B_k(1-i\alpha)a_k(t) \ . \tag{3.25}$$

The form and meaning of the two terms on the right side of Eqs. (3.24) and (3.25) are now clear. If the second term on the right side of both equations is temporarily disregarded, then the equations are in the form of a damped harmonic oscillator

$$\dot{a}_k(t) = (i\omega_k - \eta_k)a_k(t) \tag{3.26}$$

where the Gilbert relaxation rate η_k is given by

$$\eta_k = \alpha A_k \tag{3.27}$$

and ω_k is the spin wave frequency, given by

$$\omega_k = \sqrt{A_k^2 - |B_k^2|} \tag{3.28}$$

This dispersion equation is discussed in more detail shortly.

Conversely, if the first term on the right side of both equations is temporarily disregarded, both equations show that the B_k term gives the coupling between wave vectors k and $-k$. Recall that the B_k term in Eq. (3.22) derives from the dipole-dipole interaction alone. The k and $-k$ modes, therefore, are coupled only by the dipole-dipole interaction. For small damping, the α terms affect the coupling by a small amount and may be neglected. Eqs. (3.24) and (3.25) are now

$$-i\begin{pmatrix} \dot{a}_k(t) \\ \dot{a}^*_{-k}(t) \end{pmatrix} = \begin{pmatrix} A_k + i\eta_k & B_k \\ -B_k & -A_k + i\eta_k \end{pmatrix} \begin{pmatrix} a_k(t) \\ a^*_{-k}(t) \end{pmatrix} . \tag{3.29}$$

Equation (3.29) is diagonalized with the use of the Holstein-Primakoff transformation [Sparks (1964)]. The complex amplitudes $a_k(t)$ and $a^*_{-k}(t)$ are transformed to a new set of complex amplitudes $b_k(t)$ and $b^*_{-k}(t)$ through

$$a_k(t) = \lambda_k b_k(t) - \mu_k b^*_k(t) \tag{3.30}$$

and

$$a^*_{-k}(t) = \mu^*_k b_k(t) - \lambda_k b^*_{-k}(t) \ , \tag{3.31}$$

where the transformation coefficients are given by

$$\lambda_k = \sqrt{\frac{A_k + \omega_k}{2\omega_k}} \tag{3.32}$$

and

$$\mu_k = \sqrt{\frac{A_k - \omega_k}{2\omega_k}} \frac{B_k}{|B_k|} \ . \tag{3.33}$$

These are the amplitudes of the normal spin wave modes. The final diagonalized equation of motion for the spin wave b_k amplitudes is obtained as

$$-i\begin{pmatrix} b_k(t) \\ b^*_{-k}(t) \end{pmatrix} = \begin{pmatrix} \omega_k + i\eta_k & 0 \\ 0 & -\omega_k + i\eta_k \end{pmatrix} \begin{pmatrix} b_k(t) \\ b^*_{-k}(t) \end{pmatrix} . \tag{3.34}$$

The solution to this set of equations is that of a harmonic oscillator, given by

$$b_k(t) = b_{k0}\, e^{(i\omega_k - \eta_k)t} \tag{3.35}$$

and

$$b_{-k}^*(t) = b_{-k0}^*\, e^{(-i\omega_k - \eta_k)t} \quad . \tag{3.36}$$

These can be used to find linear solutions for the dynamic magnetization $\mathbf{m}_k(\mathbf{r},t)$ through Eqs. (3.30), (3.31), (3.18), and (3.19).

3.2.2 SPIN WAVE DISPERSION

The spin wave dispersion is an extremely important consideration for this analysis. The spin wave dispersion relation from Eq. (3.28) can be prescribed in more detailed form with the use of Eqs. (3.21) and (3.22). One obtains

$$\begin{aligned}\omega_k = \Big\{&\left[\omega_H + |\gamma| Dk^2 + \omega_M (1 - N_k)\sin^2\theta_k\right] \\ &\times\left[\omega_H + |\gamma| Dk^2 + \omega_M N_k\right]\Big\}^{1/2} \quad .\end{aligned} \tag{3.37}$$

Recall that for first order SWI processes energy is coupled into spin waves at $\omega_k = \omega_p / 2$ and for second order SWI processes energy is coupled into spin waves at $\omega_k = \omega_p$. The spin wave dispersion relation and the resulting spin wave bands then determine the available spin wave modes for a particular H and ω_k [Harte (1968)].

Figure 3.3 gives an example graph of spin wave frequency, expressed as $f_k = \omega_k / 2\pi$ in GHz, vs. k for a range of θ_k angles between 0° and 90°. The spin

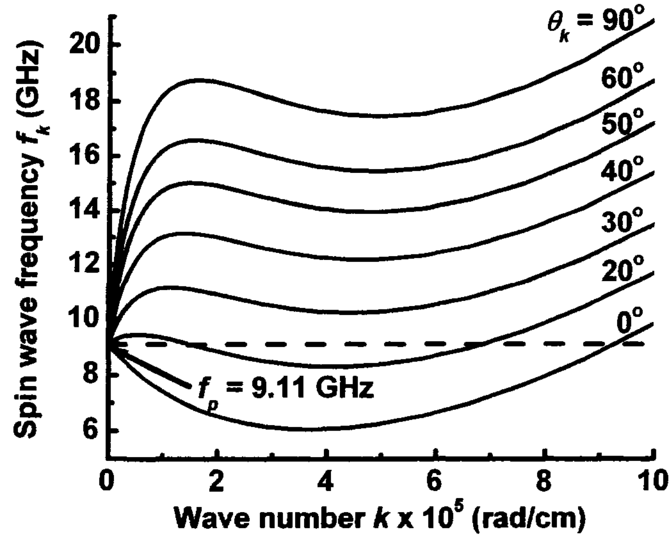

FIG. 3.3. The spin wave dispersion curve for a 104 nm thin Permalloy film. The graph shows f_k vs. k dispersion curve branches. The curve is for a ferromagnetic resonance field $H_{\mathrm{FMR}} = 830$ Oe that corresponds to the microwave pumping field $f_p = 9.11$ GHz. The dashed line is a cut at f_p. The branches of the dispersion curve shown are for the angles indicated.

wave dispersion branches are labeled by θ_k. This particular dispersion curve is for $H = 830$ Oe, which corresponds to the FMR point for a microwave pumping frequency of 9.11 GHz. The parameters for the evaluations are as follows: a thin film thickness d of 104 nm, a $4\pi M_s$ value of 11,320 G, a $|\gamma|/2\pi$ value of 2.869 MHz/Oe, and a D value of 2.1×10^{-9} Oe cm^2/rad^2. The horizontal dashed line through the spin wave dispersion shows the available modes that correspond to the FMR frequency, $f_p = 9.11$ GHz.

There are three major features of the thin film spin wave dispersion relation that are of interest here. The first is the dependence of the dispersion on H. Figure 3.4 graphs (a), (b), and (c) show dispersion curves of f_k vs. k for H values of 100, 250

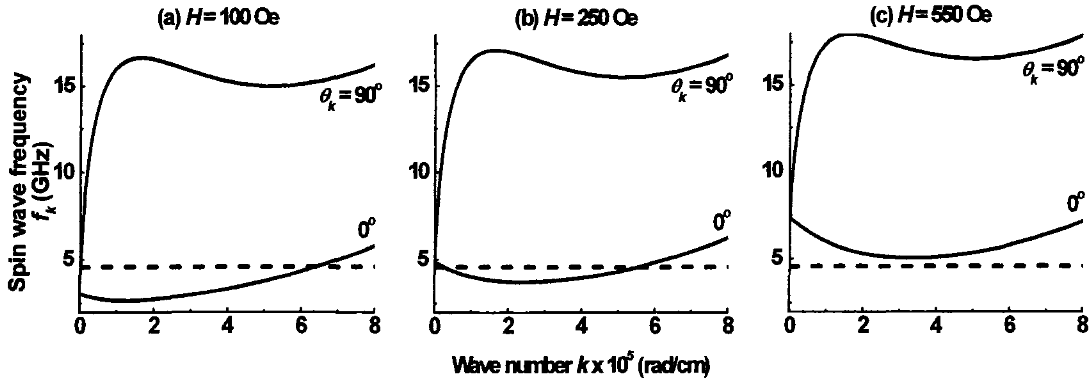

FIG. 3.4. Thin film spin wave dispersion curves for a 104 nm Permalloy film at three values of the H field, as indicated. The graphs show the f_k vs. k dispersion branches for $\theta_k = 90^\circ$ and 0°, as indicated. The dashed lines mark the frequency $f_k = f_p / 2$ =4.56 GHz.

and 550 Oe, respectively, and the same 104 nm film parameters as above. Only the $\theta_k = 0^\circ$ and 90° branches of the dispersion curve are shown. The horizontal dashed line now shows a cut through the spin wave band at $f_k = f_p / 2$.

The graphs show that the spin wave band shifts up in frequency with an increase in H. For this demonstration, there are no available spin wave modes at $f_p / 2$ for H values above about 455 Oe. There are no available modes for energy to couple into above this cutoff field H_{cut}. Section 3.5.2 will show that this results in no SWI effect. The experimental oblique pumping results shown in Ch. 7 are in agreement with this theoretical result.

The second point of note for the spin wave dispersion is the thickness dependence. Figure 3.5 shows the $\theta_k = 0^\circ$ dispersion branch for film thicknesses of 30 nm, 100

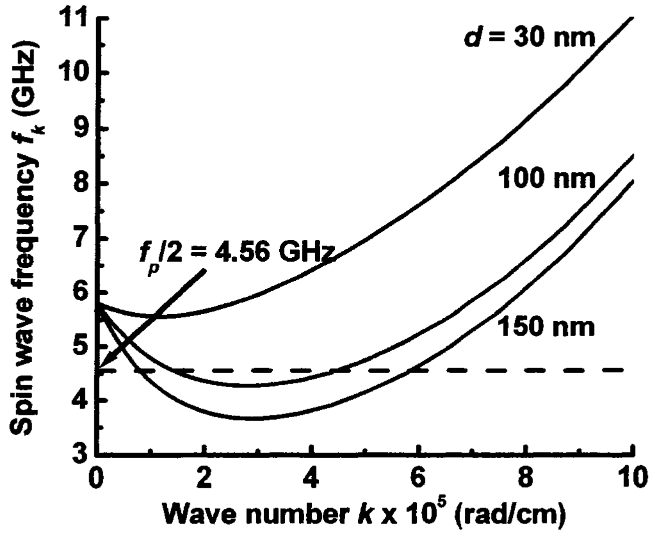

FIG. 3.5. The $\theta_k = 0^\circ$ spin wave dispersion branches for thin Permalloy films of thicknesses $d = 30$, 100, and 150 nm, as indicated. The graph shows f_k vs. k. The curve is for $H = 350$ Oe. The dashed line is a cut at $f_p/2$.

nm, and 150 nm, all at a fixed field of 350 Oe. The parameters are the same as above. The dashed line is a cut through the spin wave band at $f_k = f_p/2$.

The graphs show that the bottom of the spin wave band becomes shallow for thinner films and deeper for thicker films. This is the feature that changes the H_{cut} field with thickness. For thicker films, the H_{cut} field will be larger than for thinner films. It is important to note that for very thin films there are no available modes at $f_k = f_p/2$ for any H field and there is no first order SWI effect. The experimental oblique pumping results in Ch. 7 are in agreement with this result.

The final feature concerns the break down of the Harte approximation [Harte (1968)]. Recall that the Harte approximation takes the dynamic magnetization to be uniform across the thickness of the film. This is adequate only for small θ_k and low k spin waves. Outside these limits, a rigorous dipole-exchange dispersion calculation must be performed [Kalinikos and Slavin (1986)].

Figure 3.6 shows example f_k vs. k dispersion curves obtained with the Harte approximation and from an exact dipole-exchange spin wave analysis. The graphs are for the 104 nm thin film, a $H = 830$ Oe, and the same parameters used for Fig. 3.3. The curves are shown for θ_k angles of 0^o and 90^o. The solid curves are for the exact analysis and the dashed curves are for the dispersion relation that uses the Harte approximation. The $\theta_k = 90^o$ branches from the exact analysis are labeled as

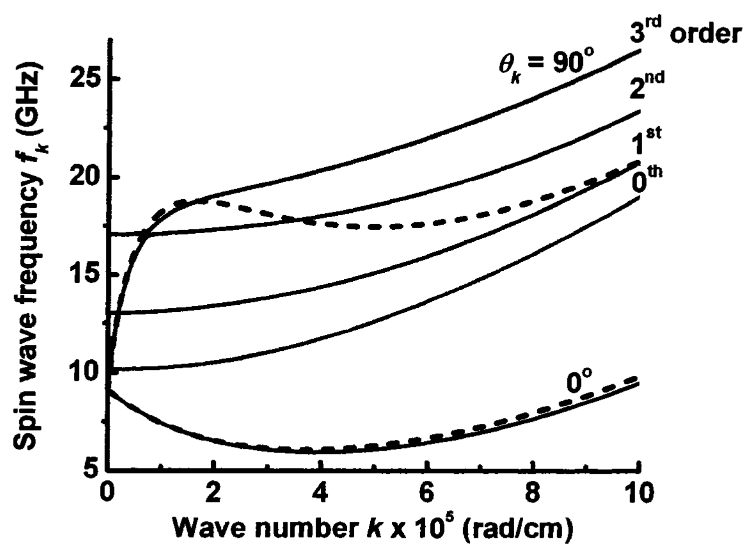

FIG. 3.6. Spin wave frequency f_k vs. wave number k curves for a 104 nm Permalloy thin film in an external field $H = 830$ Oe. The dashed curves are for the $\theta_k = 90^o$ and 0^o dispersion branches calculated with the Harte thin film approximation. The solid curves are for the exact $\theta_k = 90^o$ and 0^o dispersion branches calculated numerically for a thin film.

zeroth, first, second, and third order.

The curves shown for the $\theta_k = 90^\circ$ branch of the exact calculation are the dipole-exchange branches. The full analysis of the dispersion relation solves the electromagnetic boundary value problem. This results in a set of discrete dispersion curves for the wave number values allowed by the boundary conditions. Each curve represents a standing wave across the film thickness. For the $\theta_k = 0^\circ$ branch the only the zeroth order mode is shown. The exchange interaction results in a shift up in frequency of the higher order dispersion branches so that the degeneracy is lifted and higher order branches need not be considered.

For low kd values, the approximation is very good. The $\theta_k = 0^\circ$ branch of the dispersion relation shows a breakdown of the approximation only at large kd values. Recall that in this limit the wavelength is much smaller than the film thickness and the dipole field cannot be taken as uniform across the film. The $\theta_k = 90^\circ$ shows a larger breakdown of the approximation. For very small kd values the approximation is adequate but for larger kd values surface spin wave modes must be taken into account and the dipole field is not uniform across the thickness of the film.

From the spin wave dispersion relation analysis leading to Eq. (3.27), it can be seen that the Gilbert relaxation rate is given by

$$\eta_k = \alpha A_k = \alpha \omega_k \frac{\partial \omega_k}{\partial \omega_H} \quad , \tag{3.38}$$

where the $\partial\omega_k / \partial\omega_H = A_k / \omega_k$ is a spin wave ellipticity factor. This so called ellipticity factor, however, is not the ellipticity of the precession cone of the magnetization, but rather is related to the ellipticity e_k by $\partial\omega_k / \partial\omega_H = (1/e_k + e_k)/2$. The ellipticity of the precession cone of the magnetization is give by

$$e_k = \left|\frac{m_{k,x}}{m_{k,y}}\right| = \sqrt{\frac{A_k + |B_k|}{A_k - |B_k|}} \quad . \tag{3.39}$$

Notice that if the precession of the magnetization is circular, so that $e_k = 1$, then the ellipticity factor $\partial\omega_k / \partial\omega_H$ also goes to 1. As discussed previously, the B_k factors given only depend on the dipole-dipole interaction. A nonzero dipole-dipole interaction is necessary to have an elliptical precession.

3.3 UNIFORM MODE ANALYSIS

This section considers the specific linearized torque equation problem for $k = 0$. This connects to the uniform mode. An $\mathbf{h}_p(t)$ field is included to drive the magnetization. It is important to note that microwave field component perpendicular to the $H\hat{\mathbf{z}}$ drives the linear response. The coupled set of equations for the uniform mode becomes

$$-i\begin{pmatrix} \dot{a}_0(t) \\ \dot{a}_0^*(t) \end{pmatrix} = \begin{pmatrix} A_0(1+i\eta_0) & B_0 \\ -B_0 & -A_0(1-i\eta_0) \end{pmatrix}\begin{pmatrix} a_0(t) \\ a_0^*(t) \end{pmatrix} - |\gamma| h_{p,x} \begin{pmatrix} \cos(\omega_p t) \\ -\cos(\omega_p t) \end{pmatrix} \quad . \tag{3.40}$$

For $k=0$, $N_k=1$ is true. The Gilbert relaxation rate for the uniform mode is, therefore, given by

$$\eta_0 = \alpha \frac{2\omega_H + \omega_M}{2} \quad . \tag{3.41}$$

The uniform mode amplitude solutions are obtained as

$$a_0(t) = |\gamma| \frac{h_{p,x}}{2}\left(q_{\mathrm{LA}} e^{i\omega_p t} + q_{\mathrm{AL}} e^{-i\omega_p t}\right) \quad , \tag{3.42}$$

along with the complex conjugate of this equation. Here, equations q_{LA} and q_{AL} are the Larmor and anti-Larmor coefficients, respectively. In general, the Larmor coefficient corresponds to the precession of the dynamic magnetization in a counterclockwise direction and anti-Larmor corresponds to a clockwise precession. However, the microwave pumping field is taken to be linearly polarized and Larmor excitation is the dominate term in the response. The q_{LA} and q_{AL} coefficients are given by

$$q_{\mathrm{LA}} = \frac{\omega_M + \omega_H + \omega_p\left[1 + i2\eta_0/(2\omega_H + \omega_M)\right]}{\omega_0^2 - \omega_p^2 + i2\eta_0\omega_p} \tag{3.43}$$

and

$$q_{\mathrm{AL}} = \frac{\omega_M + \omega_H - \omega_p\left[1 - i2\eta_0 / \left(2\omega_H + \omega_M\right)\right]}{\omega_0^2 - \omega_p^2 - i2\eta_0\omega_p} \quad , \tag{3.44}$$

where η_0 is the uniform mode relaxation rate and ω_0 is the uniform mode frequency. Recall that the low power ferromagnetic resonance response is a measure of the uniform mode response. The uniform mode relaxation rate is connected to the measured FMR linewidth by

$$\eta_0 = \frac{|\gamma|\Delta H_{\mathrm{FMR}}}{2} \left.\frac{\partial\omega_0}{\partial|\gamma|H}\right|_{\mathrm{FMR}} = \frac{|\gamma|\Delta H_{\mathrm{FMR}}}{2}\varepsilon \quad , \tag{3.45}$$

where ΔH_{FMR} is the half power FMR linewidth. The multiplier ε is equal to $|\gamma|(2H_{\mathrm{FMR}} + 4\pi M_s)/2\omega_p$ and represents an ellipticity correction [Patton (1975)]. For Permalloy films at 10 GHz, this factor is about 2.

The ω_0 parameter is the uniform mode frequency which is found by the substitution of $k = 0$ into Eq. (3.37) and is given by

$$\omega_0 = \sqrt{\omega_H\left(\omega_H + \omega_M\right)} \quad . \tag{3.46}$$

This equation is the FMR Kittel equation [Kittel (1948)] for the case of an in-plane magnetized isotropic thin film. Here the condition $\omega_0 = \omega_p$ defines the FMR field, H_{FMR}.

Notice that in the Larmor and anti-Larmor coefficient equations, Eqs. (3.43) and (3.44), respectively, the $i2\eta_0/(2\omega_H+\omega_M)$ term is very small compared to 1. This term can then be neglected and the equations are

$$q_{\mathrm{LA}}=\frac{\omega_M+\omega_H+\omega_p}{\omega_0^2-\omega_p^2+i2\eta_0\omega_p} \tag{3.47}$$

and

$$q_{\mathrm{AL}}=\frac{\omega_M+\omega_H-\omega_p}{\omega_0^2-\omega_p^2-i2\eta_0\omega_p}\ , \tag{3.48}$$

The final solutions for $\mathbf{m}_0(\mathbf{r},t)$ can be found from the expressions for the Larmor and anti-Larmor coefficients, Eq. (3.42) and the complex conjugate, and Eqs. (3.18) and (3.19). The results for $m_{0,x}$ and $m_{0,y}$ can be used to calculate the angle of the precession cone of the magnetization at FMR. These angles are useful for the discussion of the effects of the uniform mode at the SWI threshold in Ch. 6 and are given by

$$\begin{aligned}\vartheta_x&=\sin^{-1}\left(\frac{|m_{0,x}|}{M_s}\right)\\&=\sin^{-1}\left[\left(\frac{\omega_H+\omega_M}{\omega_p}\right)\frac{h_p}{\Delta H_{\mathrm{FMR}}\sqrt{1+\left(\frac{\omega_M}{2\omega_p}\right)}}\right]\end{aligned} \tag{3.49}$$

and

$$\begin{aligned}\vartheta_y &= \sin^{-1}\left(\frac{|m_{0,y}|}{M_s}\right) \\ &= \sin^{-1}\left[\frac{h_p}{\Delta H_{\mathrm{FMR}}\sqrt{1+\left(\dfrac{\omega_M}{2\omega_p}\right)}}\right].\end{aligned} \tag{3.50}$$

The in-plane ϑ_x angle is larger than the out-of-plane ϑ_y angle as it depends on $(\omega_H + \omega_M)/\omega_p$. Recall that the static field and the equilibrium position of the magnetization are in the film plane. The dynamic magnetization then has a larger precession angle in the film plane.

3.4. SPIN WAVE INSTABILITY

This section is divided into three subsections. The first subsection sets up the nonlinear problem at hand. The next subsection presents and discusses the nonlinear first order equations applicable to in-plane oblique pumping with specific examples of subsidiary absorption and parallel pumping. The final subsection presents and discusses the nonlinear second order equations applicable to resonance saturation. The last two sections provide the working equations for the SWI threshold determinations for the processes of interest.

3.4.1. INTRODUCTION TO THE SPIN WAVE INSTABILITY ANALYSES

The starting point for the spin wave instability analysis is the same magnetic torque equation developed above. The solutions of interest are the spin wave and critical threshold field amplitudes. The nonlinear terms are now retained. These nonlinear terms contain linear $\mathbf{m}_k(t)$ components, but also include $\mathbf{m}_0(t)$ and $\mathbf{h}_p(t)$ components. This results in a very complicated set of nonlinear equations for $\mathbf{m}_k(t)$. To find solutions for this nonlinear set of equations, the $|\mathbf{M}(\mathbf{r},t)|$ is taken to be a constant and is written as $M_s^2 = m_{k,x}^2 + m_{k,y}^2 + (M_s + m_{k,z})^2$. The small signal limit approximation is again made and the $m_{k,z}$ component of $\mathbf{M}(\mathbf{r},t)$, that is the source of the coupling between the nonlinear equations, is written in terms of $m_{k,y}$ and $m_{k,x}$. As before, Eqs. (3.18) and (3.19) are used to transform from $\mathbf{m}_k(\mathbf{r},t)$ to $a_k(t)$.

After a considerable amount of algebra one obtains

$$
\begin{aligned}
-i\begin{pmatrix} \dot{a}_k(t) \\ \dot{a}_{-k}^*(t) \end{pmatrix} &= \begin{pmatrix} A_k + i\eta_k & B_k \\ -B_k & -A_k + i\eta_k \end{pmatrix}\begin{pmatrix} a_k(t) \\ a_{-k}^*(t) \end{pmatrix} \\
&+ \begin{pmatrix} C_k(t) & D_k(t) \\ -D_k^*(t) & -C_k^*(t) \end{pmatrix}\begin{pmatrix} a_k(t) \\ a_{-k}^*(t) \end{pmatrix},
\end{aligned}
\tag{3.51}
$$

where the $C_k(t)$ and $D_k(t)$ terms are given by

$$
\begin{aligned}
C_k(t) = &-\frac{\omega_M}{2}(1-N_k)\sin\theta_k\cos\theta_k\left[a_0(t)+a_0^*(t)\right] \\
&+|\gamma|h_{p,z}\cos(\omega_p t) \\
&-\frac{\omega_M}{4}\left[(1-N_k)(1-3\cos^2\theta_k)+(1+N_k)\right]a_0(t)a_0^*(t) \\
&+\frac{\omega_M}{4}a_0^*(t)a_0^*(t)+\frac{|\gamma|h_{p,x}}{2}a_0^*(t)\cos(\omega_p t)
\end{aligned}
\tag{3.52}
$$

and

$$
\begin{aligned}
D_k(t) = &-\omega_M(1-N_k)\sin\theta_k\cos\theta_k a_0(t) \\
&+\frac{|\gamma|h_{p,x}}{2}a_0(t)\cos(\omega_p t) \\
&-\frac{\omega_M}{4}\left[(1-N_k)\sin^2\theta_k-(1+N_k)\right]a_0(t)a_0^*(t) \\
&+\left\{\frac{|\gamma|Dk^2}{2}-\frac{\omega_M}{2}\left[1-2(1-N_k)\cos^2\theta_k\right]\right\} \\
&\times a_0(t)a_0(t) \quad .
\end{aligned}
\tag{3.53}
$$

The $C_k(t)$ and $D_k(t)$ expressions contain both first and second order terms in the a_0 and a_0^*. Terms of third order or higher are not included. The first order terms have single $a_0(t)$, $a_0^*(t)$, and $h_{p,z}$ components. The second order terms include products of the form $a_0(t)a_0(t)$, $a_0(t)a_0^*(t)$, $a_0^*(t)a_0^*(t)$, $a_0(t)h_{p,x}$, and $a_0^*(t)h_{p,x}$. For the first order SWI theory the second order terms are discarded and for the second order theory, the first order terms are discarded.

As before, the linear terms in Eq. (3.51) are diagonalized with the Holstein-Primakoff transformation. The same transformation is also applied to the $C_k(t)$ and

$D_k(t)$. This leads to a coupled equation of motion for the spin wave mode amplitudes given by

$$-i\begin{pmatrix} \dot{b}_k(t) \\ \dot{b}_{-k}^*(t) \end{pmatrix} = \begin{pmatrix} \omega_k + i\eta_k + F_k(t) & G_k(t) \\ -G_k^*(t) & -\omega_k + i\eta_k - F_k^*(t) \end{pmatrix} \begin{pmatrix} b_k(t) \\ b_{-k}^*(t) \end{pmatrix}, \tag{3.54}$$

where F_k and G_k are given by

$$F_k(t) = \lambda_k^2 C_k(t) + \mu_k^2 C_k^*(t) - \lambda_k \mu_k \left[D_k(t) + D_k^*(t) \right] \tag{3.55}$$

and

$$G_k(t) = \lambda_k^2 D_k(t) + \mu_k^2 D_k^*(t) - \lambda_k \mu_k \left[C_k(t) + C_k^*(t) \right] . \tag{3.56}$$

The λ_k and μ_k parameters are specified in Eqs. (3.32) and (3.33), respectively. The $F_k(t)$ amounts to a small modulation of ω_k. Since $|F_k(t)| << \omega_k$ is true, the $F_k(t)$ modulation effect may be omitted from the instability analysis. The $G_k(t)$ function provides a modulation of the coupling between the $b_k(t)$ and $b_{-k}^*(t)$ modes. This is the source of the parametric excitation for spin wave instability.

The complicated $G_k(t)$ function contains both $C_k(t)$ and $D_k(t)$ terms. These terms, in turn, depend on the microwave pumping field directly through $h_{p,z}$ and indirectly through the uniform mode amplitude $a_0(t)$ and its complex conjugate. The modulation due to the $\mathbf{h}_p(t)$ in the $G_k(t)$ function is the source of the transfer of energy from the microwave pumping field into a given spin wave mode at $\mathbf{k}$ and ω_k. From the form of the $C_k(t)$ and the $D_k(t)$, and with the uniform mode solution in Eq. (3.42), one can see that the time dependence of the modulation of the $G_k(t)$ expression is given by $e^{\pm in\omega_p t}$ where n has possible values of 0, ± 1, and ± 2.

The $G_k(t)$ function is then recast with the explicit time dependence as [Schloemann (1959)].

$$G_k\left(t\right) = \sum_{n=-2}^{+2} G_k^{(n)} e^{in\omega_p t} \quad . \tag{3.57}$$

The $n = 0$ term can be neglected on the basis of two arguments. First, the $n = 0$ term is a constant and can in principle be eliminated by another Holstein-Primakoff transfomation. The second argument is that it can be neglected by the simple fact that $| G_k^{(0)} | << \omega_k$ is true.

The $n = \pm 1$ and $n = \pm 2$ cases are investigated separately. The $n = \pm 1$ case occurs for frequencies associated with the first order SWI processes and the $n = \pm 2$ case occurs for frequencies associated with the second order SWI processes.

3.4.2 FIRST ORDER SPIN WAVE INSTABILITY

For the first order SWI process $n = \pm 1$ is substituted into Eq. (3.54), as the resonance frequency is $\omega_p / 2$. Recall that the $F_k(t)$ function is a small nonlinear modulation of ω_k and is neglected. The working equation for the spin wave mode amplitudes is then given by

$$-i\begin{pmatrix} \dot{b}_k(t) \\ \dot{b}^*_{-k}(t) \end{pmatrix} = \begin{pmatrix} \omega_k + i\eta_k & G_k^{(1)}\,\mathrm{e}^{i\omega_p t} + G_k^{(-1)}\,\mathrm{e}^{-i\omega_p t} \\ -G_k^{*(1)}\,\mathrm{e}^{-i\omega_p t} - G_k^{*(-1)}\,\mathrm{e}^{i\omega_p t} & -\omega_k + i\eta_k \end{pmatrix} \cdot \begin{pmatrix} b_k(t) \\ b^*_{-k}(t) \end{pmatrix} \tag{3.58}$$

The trial solutions are

$$b_k(t) = b_k^{(1)}(t)\,\mathrm{e}^{i\frac{\omega_p}{2}t} + b_k^{(-1)}(t)\,\mathrm{e}^{-i\frac{\omega_p}{2}t} \tag{3.59}$$

and

$$b^*_{-k}(t) = b_{-k}^{(1)*}(t)\,\mathrm{e}^{-i\frac{\omega_p}{2}t} + b_{-k}^{(-1)*}(t)\,\mathrm{e}^{i\frac{\omega_p}{2}t} \quad . \tag{3.60}$$

The $b_k^{(1)}(t)$, $b_k^{(-1)}(t)$, $b_{-k}^{(1)*}(t)$, and $b_{-k}^{(-1)*}(t)$ are "slowly varying" envelopes in which the corresponding $b_k(t)$ and $b^*_{-k}(t)$ functions oscillate in time with $\mathrm{e}^{i(\omega_p/2)t}$.

The trial solutions given in Eqs. (3.59) and (3.60) are substituted into Eq. (3.58). The time dependences are compared and the terms with fast oscillations in time are neglected. Four separate equations come out of this analysis. The equations for $\dot{b}_k^{(1)}(t)$ and $\dot{b}_{-k}^{(1)*}(t)$ are retained as they are the only equations that are driven resonantly, specifically when $\omega_k - \omega_p/2 = 0$. These equations for $n = +1$

correspond to Larmor precession, as discussed in Sec. 3.2. The $G_k^{(-1)}$ coupling term is neglected, as the corresponding equations are not driven resonantly and correspond to anti-Larmor precession. The resultant coupled set of equations for $n = +1$ are

$$\begin{bmatrix} \dot{b}_k^{(1)}(t) \\ \dot{b}_{-k}^{(1)*}(t) \end{bmatrix} = \begin{bmatrix} i\left(\omega_k - \dfrac{\omega_p}{2}\right) - \eta_k & iG_k^{(1)} \\ -iG_k^{(1)*} & i\left(-\omega_k + \dfrac{\omega_p}{2}\right) - \eta_k \end{bmatrix} \bullet \begin{bmatrix} b_k^{(1)}(t) \\ b_{-k}^{(1)*}(t) \end{bmatrix} \tag{3.61}$$

where $b_k^{(1)}(t)$ and $b_{-k}^{(1)*}(t)$ are the complex amplitudes of the coupled spin waves that propagate in the $\pm k$ direction. This coupled set of first order differential equations rewritten as a single second order differential equation is

$$\begin{aligned} 0 &= \ddot{b}_k^{(1)}(t) + 2\eta_k \dot{b}_k^{(1)}(t) \\ &+ \left[\left(\omega_k - \frac{\omega_p}{2}\right)^2 + \eta_k^2 - \left|G_k^{(1)}\right|^2\right] b_k^{(1)}(t) \end{aligned} \tag{3.62}$$

Equation (3.62) is that of a damped harmonic oscillator and has a solution of the form

$$b_k^{(1)}(t) = b_{k0}^{(1)}\, e^{\kappa t} \tag{3.63}$$

where κ is

$$\kappa = -\eta_k \pm \sqrt{\left|G_k^{(1)}\right|^2 - \left(\omega_k - \frac{\omega_p}{2}\right)^2} \quad . \tag{3.64}$$

The form of κ shows the SWI effect even without a detailed knowledge of the $G_k^{(1)}$ function. Recall that the $G_k^{(1)}$ term depends on the microwave pumping field amplitude h_p directly and indirectly. For a sufficiently small h_p, $G_k^{(1)}$ is small, κ is negative, the $b_k^{(1)}(t)$ function always shows a decay, there is no SWI, and the spin wave modes continue to reside at thermal levels. As h_p in increased, however, $G_k^{(1)}$ term grows. Exactly where κ becomes positive for some mode or set of available **k** and ω_k modes, there is a threshold and an exponential growth in the $b_k^{(1)}(t)$ amplitudes for these modes. Therefore, the condition for SWI is found when $\kappa = 0$ and is

$$\left|G_k^{(1)}\right|^2 = \left(\omega_k - \frac{\omega_p}{2}\right)^2 + \eta_k^2 \quad . \tag{3.65}$$

The critical SWI threshold field amplitude h_{crit}, at a given H and ω_p, is defined as the ***minimum*** threshold among all the available **k** and ω_k modes under these conditions. The modes with $\omega_k = \omega_p / 2$ result in a smaller $G_k^{(1)}$ term, as seen in Eq. (3.65). The threshold condition for the unstable growth of first order parametric spin waves at $\omega_k = \omega_p / 2$ reduces to $| G_k^{(1)} | = \eta_k$.

The next step in the first order SWI analysis is to find the form of $G_k^{(1)}$. Equations (3.52) and (3.53) for $C_k(t)$ and $D_k(t)$, respectively, are substituted into Eq. (3.56) for $G_k(t)$ and only the nonlinear first order SWI terms are retained, as discussed previously. The condition that $\omega_k = \omega_p/2$ is used and after a considerable amount of algebra one obtains

$$G_k^{(1)}(k,\theta_k) = -\frac{\omega_M}{2\omega_p}|\gamma| h_p \bullet \left[W_k^{(1)\perp}(H,k,\theta_k)\sin\phi + W_k^{(1)\parallel}(H,k,\theta_k)\cos\phi\right] \tag{3.66}$$

where ϕ is the angle between the $\mathbf{H}$ field and the $\mathbf{h}_p(t)$ field. Here, the h_p dependence is separated out from the (H,k,θ_k) in order to obtain an h_{crit} determination from the threshold condition. The new dimensionless $W_k^{(1)\perp}(H,k,\theta_k)$ and $W_k^{(1)\parallel}(H,k,\theta_k)$ functions include the remaining dependences on the H field, the k and θ_k modes, and all of the other parameters enumerated above. The $W_k^{(1)\perp}(H,k,\theta_k)$ and $W_k^{(1)\parallel}(H,k,\theta_k)$ dimensionless coupling coefficients are given by

$$W_k^{(1)\perp}(H,k,\theta_k) = (1-N_k)\sin 2\theta_k \bullet \left[\begin{array}{l}\left(A_k - B_k + \frac{\omega_p}{2}\right)q_{\mathrm{LA}} \\ +\left(A_k - B_k - \frac{\omega_p}{2}\right)q^*_{\mathrm{AL}}\end{array}\right] \tag{3.67}$$

and

$$W_k^{(1)\parallel}\left(H,k,\theta_k\right)=\frac{2B_k}{\omega_M} \quad , \tag{3.68}$$

where the effective demagnetizing term N_k is the thickness dependent term given in Eq. (3.9), A_k and B_k are given in Eqs. (3.21) and (3.22), and q_{LA} and q_{AL}^{*} are the Larmor and anti-Larmor coefficients found in Eqs. (3.43) and (3.44), respectively.

Recall that the threshold condition for the unstable growth of first order parametric spin waves at $\omega_k = \omega_p/2$ is $|G_k^{(1)}| = \eta_k$. Then one can write the theoretical threshold h_c amplitude as [Patton (1969), Green *et al.* (1969)]

$$\begin{aligned} h_c &= \frac{2\omega_p}{|\gamma|\omega_M} \\ &\times \frac{\eta_k}{\left|W_k^{(1)\perp}\left(H,k,\theta_k\right)\sin\phi + W_k^{(1)\parallel}\left(H,k,\theta_k\right)\cos\phi\right|} \quad . \end{aligned} \tag{3.69}$$

As mentioned above, the h_{crit} at a given H field and ω_p is defined as the *minimum* threshold among all the available ω_k modes under these conditions. Equation (3.69) is minimized to obtain the h_{crit} amplitude. The modes that satisfy this condition are termed the critical modes (k_{crit}, θ_{crit}). One can simplify the minimization by use of the spin wave dispersion relation ω_k. Recall from Sec. 3.2 that for a given H, the available k and θ_k modes are defined by the ω_k dispersion relation as given in Eq. (3.37), again subject to the $\omega_k = \omega_p/2$ constraint. This dispersion constraint allows one to write θ_k as a function of k. Equation (3.69) is then

$$h_{\text{crit}}^{(1)} = \frac{\omega_p}{\omega_M} \bullet \min\left[\frac{\Delta H_k}{\left|W_k^{(1)\perp}(H,\theta_k)\sin\phi + W_k^{(1)\parallel}(H,\theta_k)\cos\phi\right|}\right]_{\omega_k=\omega_p/2} . \tag{3.70}$$

Here the spin wave relaxation rate η_k has been cast in terms of a spin wave linewidth parameter. The spin wave linewidth parameter is

$$\Delta H_k = 2\eta_k / |\gamma| \ . \tag{3.71}$$

This parameter ΔH_k serves one simple function, to cast η_k into linewidth units. It is not a *real* linewidth.

Equation (3.70) is for an arbitrary angle ϕ between the $\mathbf{H}$ and the $\mathbf{h}_p(t)$ fields and the experimental situation that pertains to this is termed *oblique pumping*. Two special cases are now considered. The first case, termed *parallel pumping,* is for an angle $\phi = 0°$ between the $\mathbf{H}$ and the $\mathbf{h}_p(t)$ fields. Notice that the $W_k^{(1)\parallel}$ coefficient is multiplied by a factor of $\cos\phi$ and the $W_k^{(1)\perp}$ dimensionless coupling coefficient is multiplied by a factor of $\sin\phi$. The process corresponding to $W_k^{(1)\parallel}$ is a maximum at $\phi = 0°$ and there is no coupling of energy by the $W_k^{(1)\perp}$ coefficient.

The $W_k^{(1)\parallel}$ coefficient is independent of the uniform mode and depends entirely on the dipole-dipole interactions, as seen by the $\sin^2\theta_k$ and $4\pi N_k M_s$ dependencies in Eqs. (3.68) and (3.22). The resultant h_{crit} function for parallel pumping is completely independent of the uniform mode and depends entirely on a direct coupling of the $\mathbf{h}_p(t)$ field to the available spin wave modes via the dipole-dipole interaction.

As discussed above, the dipole-dipole interaction results in an elliptical precession of the magnetization. The elliptical precession in combination with the assumption that the amplitude of the magnetization is constant, $|\mathbf{M}| = M_s$, results in a wobble of the $\hat{\mathbf{z}}$ – component of the dynamic magnetization. The precession of the in-plane dynamic magnetization has a time dependence of $e^{i\omega_k t}$ and the wobble of $m_{k,z}$ has a time dependence of $e^{i2\omega_k t}$. The $h_{p,z}(t)$ has a time dependence of $e^{i\omega_p t}$. Above threshold, energy is parametrically pumped into the critical $+k$ and $-k$ spin wave modes from the microwave pumping field $h_{p,z}(t)$ at $\omega_k = \omega_p / 2$ for the first order parallel pumping spin wave instability process [Patton (1975)]. However, if there is no dipole-dipole interaction, there is circular precession, no wobble of $m_{k,z}$, and no parallel pumping threshold instability process.

The second case termed *subsidiary absorption* is where the angle between the **H** and $\mathbf{h}_p(t)$ fields is perpendicular, $\phi = 90°$, and only the $W_k^{(1)\perp}$ coefficient is applicable. For a H swept high power FMR measurement, the loss due to this nonlinear process is subsidiary to the FMR response.

For subsidiary absorption the $h_{\text{crit}}^{(1)}$ function contains the uniform mode amplitude, as given in Eq. (3.42), and depends on an indirect coupling of energy from the h_p field into the available spin wave modes through the uniform mode. For this case, energy is pumped into the uniform mode and the uniform precession amplitude increases linearly until the power level exceeds some critical threshold. This critical threshold occurs when the power level exceeds the rate that energy can be lost from spin wave modes due to relaxation processes. The energy is then parametrically pumped into the critical $+k$ and $-k$ spin wave modes at $\omega_k = \omega_p/2$. Equation (3.70) for oblique pumping contains the coupling of energy due to both the subsidiary absorption and the parallel pumping processes weighted according to $\sin\phi$ and $\cos\phi$.

3.4.3 SECOND ORDER SPIN WAVE INSTABILITY

This subsection is for the case of second order SWI processes. From Eq. (3.57), one can see that $G_k(t)$ with a time dependence of $e^{\pm i2\omega_p t}$ has resonance frequencies at the microwave pumping frequency, as required for second order processes. This time dependence is substituted into the expression for the spin wave amplitudes in Eq. (3.54). Recall that the $F_k(t)$ function has been neglected, as the function is just a small nonlinear modulation of ω_k. Similar trial functions to those used for the first order SWI are used for the solutions to the second order set of coupled equations with the exception that the time dependences are now $e^{i\omega_p t}$ and $e^{-i\omega_p t}$. One uses

$$b_k(t) = b_k^{(2)}(t)e^{i\omega_p t} + b_k^{(-2)}(t)e^{-i\omega_p t} \tag{3.72}$$

and

$$b_{-k}^{*}(t)=b_{-k}^{(2)*}(t)\mathrm{e}^{-i\omega_p t}+b_{-k}^{(-2)*}(t)\mathrm{e}^{i\omega_p t} \quad . \tag{3.73}$$

The $b_k^{(2)}(t)$, $b_k^{(-2)}(t)$, $b_{-k}^{(2)*}(t)$, and $b_{-k}^{(-2)*}(t)$ are "slowly varying" envelopes in which the corresponding $b_k(t)$ and $b_{-k}^{*}(t)$ functions oscillate in time with $\mathrm{e}^{i\omega_p t}$. Four separate equations come out of this analysis. The equations for $\dot{b}_k^{(2)}(t)$ and $\dot{b}_{-k}^{(2)*}(t)$ are retained as they are the only equations that are driven resonantly, specifically when $\omega_k-\omega_p=0$ is satisfied. The procedure established in the previous subsection is used to obtain the coupled set of working equations for the second order spin wave mode amplitudes and are given by

$$\begin{bmatrix}\dot{b}_k^{(2)}(t)\\ \dot{b}_{-k}^{(2)*}(t)\end{bmatrix}=\begin{bmatrix}i(\omega_k-\omega_p)-\eta_k & iG_k^{(2)}\\ -iG_k^{(2)*} & i(-\omega_k+\omega_p)-\eta_k\end{bmatrix} \bullet\begin{bmatrix}b_k^{(2)}(t)\\ b_{-k}^{(2)*}(t)\end{bmatrix} \quad . \tag{3.74}$$

where $b_k^{(2)}(t)$ and $b_{-k}^{(2)*}(t)$ are the complex amplitudes of the coupled spin waves that propagate in the $\pm k$ directions. This coupled set of first order differential equations is rewritten as a single second order differential equation of a damped harmonic oscillator where the solution has the form

$$b_k^{(2)}(t)=b_{k0}^{(2)}\,\mathrm{e}^{\kappa t} \tag{3.75}$$

where κ is

$$\kappa=-\eta_k\pm\sqrt{\left|G_k^{(2)}\right|^2-\left(\omega_k-\omega_p\right)^2} \quad . \tag{3.76}$$

A detailed knowledge of the $G_k^{(2)}$ function is not necessary to understand the second order SWI effect. Recall that $G_k^{(2)}$ depends directly on the microwave pumping field amplitude h_p. For a sufficiently small h_p, the $G_k^{(2)}$ term is small, κ is negative, the $b_k^{(2)}(t)$ amplitudes show a decay, there is no spin wave instability, and the spin wave modes reside at thermal levels. As the h_p field is increased, the $G_k^{(2)}$ term increases. Exactly where κ becomes positive for some mode or set of available $\mathbf{k}$ and ω_k modes, there is a threshold. Above this threshold there is an exponential growth in the $b_k^{(2)}(t)$ amplitudes. Therefore, the condition for spin wave instability is found when $\kappa = 0$ and is

$$\left|G_k^{(2)}\right|^2 = \left(\omega_k - \omega_p\right)^2 + \eta_k^2 \quad . \tag{3.77}$$

Recall that the critical spin wave instability threshold h_{crit} at a given H and ω_p is defined as the ***minimum*** threshold among all the available $\mathbf{k}$ and ω_k modes under these conditions. One can clearly see in Eq. (3.77) that the modes with $\omega_k = \omega_p$ will have a smaller $G_k^{(2)}$ term than the others. The threshold condition for the unstable growth of first order parametric spin waves at $\omega_k = \omega_p$ reduces to $|G_k^{(2)}| = \eta_k$.

To find $G_k^{(2)}$ the second order SWI terms in $C_k(t)$ and $D_k(t)$ are retained and the condition that $\omega_k = \omega_p$ is now applied. After a considerable amount of algebra, one obtains

$$G_k^{(2)}(k,\theta_k) = \frac{|\gamma| h_p \omega_M}{4\omega_p} W_k^{(2)} \ . \tag{3.78}$$

with

$$W_k^{(2)}(H,k,\theta_k) = [W_1 + W_2 + W_3 + W_4 + W_5] \ . \tag{3.79}$$

The W_1, W_2, W_3, W_4, and W_5 terms are given by

$$W_1(H,k,\theta_k) = q_{\mathrm{LA}}^2 \left[r(A_k + \omega_p) - B_k v \right] \ , \tag{3.80}$$

$$W_2(H,k,\theta_k) = q_{\mathrm{AL}}^{*2} \left[r(A_k - \omega_p) - B_k v \right] \ , \tag{3.81}$$

$$W_3(H,k,\theta_k) = q_{\mathrm{AL}}^* q_{\mathrm{LA}} \left[s(A_k + \omega_p) + s(A_k - \omega_p) - B_k u \right] \ , \tag{3.82}$$

$$W_4(H,k,\theta_k) = \frac{1}{2} q_{\mathrm{LA}} (A_k + \omega_p - B_k) \ , \tag{3.83}$$

and

$$W_5(H,k,\theta_k) = \frac{1}{2} q_{\mathrm{AL}}^* (A_k - \omega_p - B_k) \ . \tag{3.84}$$

The A_k and B_k were obtained previously, as given in Eq. (3.21) and (3.22) respectively. The q_{LA} and q_{AL} are the Larmor and anti-Larmor uniform mode response functions obtained in Sec. 3.3. The remaining terms are

$$r = \frac{1}{4}\omega_M \left[\left[1 - N_k(k) \right] 2\cos^2\theta_k - 1 \right] + \frac{1}{2}|\gamma| D k^2 \ , \tag{3.85}$$

$$v = \frac{1}{4}\omega_M \quad , \tag{3.86}$$

$$s = -\frac{1}{4}\omega_M \left[\left[1 - N_k(k)\right]\sin^2\theta_k - \left(1 + N_k\right)\right] \quad , \tag{3.87}$$

and

$$u = \frac{1}{2}\omega_M \left[\left[1 - N_k(k)\right]\left(3\cos^2\theta_k - 1\right) - \left[1 + N_k(k)\right]\right] \quad . \tag{3.88}$$

Recall that the threshold condition for the unstable growth of the second order parametric spin waves at $\omega_k = \omega_p$ is now given by $|G_k^{(2)}| = \eta_k$. The theoretical threshold h_c amplitude is obtained

$$h_c = \frac{2}{\sin\phi}\sqrt{\frac{\omega_p \Delta H_k}{|\gamma|\left|W_k^{(2)}(H,\theta_k)\right|}} \tag{3.89}$$

where the relaxation rate is again written in terms of the spin wave linewidth.

Recall that the critical spin wave instability threshold h_{crit} at a given H and ω_p is defined as the *minimum* threshold among all the available **k** and ω_k modes under these conditions. The minimization is simplified by use of the spin wave dispersion relation ω_k. For a given H, the available k and θ_k modes are defined by the ω_k dispersion relation as given in Eq. (3.37), subject to the $\omega_k(k,\theta_k) = \omega_p$ constraint. This dispersion constraint allows one to write θ_k as a function of k. The $h_{crit}^{(2)}$ amplitude is

$$h_{\text{crit}}^{(2)} = \frac{2}{\sin\phi} \min\left[\sqrt{\frac{\omega_p \Delta H_k}{|\gamma| \left| W_k^{(2)}(H,\theta_k) \right|}} \right]_{\omega_k = \omega_p} . \tag{3.90}$$

Notice that $h_{\text{crit}}^{(2)}$ depends on $1/\sin\phi$. This process is then a maximum at $\phi = 90^{\circ}$.

The second order SWI process contains the uniform mode amplitude, as given in Eq. (3.42) and depends on an indirect coupling of energy from the $\mathbf{h}_p(t)$ field into the available spin wave modes through the uniform mode. As energy is pumped into the uniform mode, the uniform precession amplitude increases until the power level exceeds some critical threshold. This critical threshold occurs when the power level exceeds the rate that energy can be lost due to relaxation processes. The energy is then parametrically pumped into certain available spin wave modes as the uniform mode is saturated. Here the spin wave modes are at the microwave pumping frequency $\omega_k = \omega_p$. For a static magnetic field swept ferromagnetic resonance measurement, the excitation of these modes will be at the ferromagnetic resonance field. As the energy is parametrically pumped from the uniform mode the uniform mode precession angle locks up and there is a measurable decrease in the ferromagnetic resonance amplitude. On the other hand, as the energy is pumped into spin waves at the microwave pumping frequency there is a broadening of the ferromagnetic resonance profile. This saturation of the uniform mode at resonance is the reason this effect is termed *resonance saturation.*

3.5 SPIN WAVE INSTABILITY THEORY EXAMPLE CALCULATIONS

This section provides example calculations of the theory developed above. These example calculations demonstrate how the first and second order processes work and set the stage for the data analysis in Ch. 6 and 7. Resonance saturation is considered first, followed by example results for subsidiary absorption, oblique pumping, and parallel pumping. Graphs of h_{crit} vs. H butterfly curves and the corresponding k_{crit} vs. H, and θ_{crit} vs. H are shown and discussed.

The analysis is for parameters applicable to an isotropic 104 nm thin Permalloy film. The parameters given in given in Ch. 4 and Olson *et al.* (2007) for the 104 nm Permalloy film are used. These are a $4\pi M_{s\text{-eff}}$ value of 11,320 G, $|\gamma|/2\pi$ value of 2.869 MHz/Oe and ΔH_{FMR} value of 59 Oe. The calculations are for a f_p value of 9.11 GHz and with a standard D value for Permalloy of 2.1×10^{-9} Oe cm^2/rad^2 [Nisenoff and Terhune (1965)].

The numerical minimization procedure to obtain the theoretical $h_{\mathrm{crit}}^{(2)}$ and $h_{\mathrm{crit}}^{(1)}$ values for given H values is discussed at length in [Nazarov *et al.* (2002)] and elsewhere. One starts with a fine mesh of the available θ_k values defined by the $\omega_k(k,\theta_k)=\omega_p$ constraint, for second order SWI, or $\omega_k(k,\theta_k)=\omega_p/2$ constraint, for first order SWI, evaluates the resulting h_c at each point, and selects the minimum value which is h_{crit}. At the same time, the values of θ_k and k that correspond to this minimum threshold point define the critical modes θ_{crit} and k_{crit}. One then repeats the process for fields over the range of interest and constructs a theoretical butterfly curve h_{crit} vs. H, as well as the corresponding θ_{crit} and k_{crit} vs. H profiles. This entire process may be repeated with different ΔH_k trial functions as a control parameter to obtain a best fit to a given set of experimental h_{crit} vs. H data. One can then use such fits to make empirical determinations of appropriate ΔH_k functions for the process and material of interest.

3.5.1 RESONANCE SATURATION EXAMPLE CALCULATIONS

This subsection considers example second order SWI results. The calculation is performed for a coupling angle of $\phi = 90^{\circ}$ where there is a maximum coupling of energy into the uniform mode. A constant ΔH_k of 32 Oe is used for the example calculations. The other parameters used for the fit are given above.

Figure 3.7 shows the h_{crit} vs. H butterfly curve. A schematic k_{crit} vs. H graph and a schematic diagram of the direction of propagation of k_{crit}, $\theta_{crit} = 0^{\circ}$, with respect to the sample and the H field are shown in the insets. The critical modes that correspond to the butterfly curve in Fig. 3.7 show a linear decrease of k_{crit} with an increase of H. The k_{crit} values range from $9.1\times10^5 - 9.6\times10^5$ rad/cm and the angle is constant at $\theta_{crit} = 0^{\circ}$. Interestingly, $\theta_{crit} = 0^{\circ}$ also comes out of the original Suhl SWI theory for bulk isotropic ferrites biased at the FMR field [Suhl (1957)].

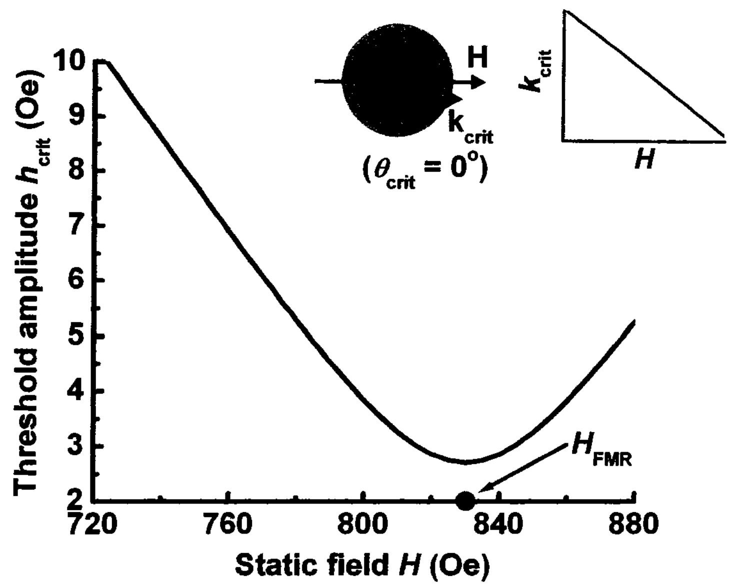

FIG. 3.7. Resonance saturation butterfly curve of h_{crit} vs. H for the 104 nm Permalloy film. The pumping frequency was 9.11 GHz. The solid circle denotes the FMR field position. The insets show k_{crit} vs. H and configuration for $\mathbf{k}_{crit}$ and $\mathbf{H}$ where the $\theta_{crit} = 0^{o}$.

The basic shape of the thin film butterfly curve for resonance saturation is determined only by the uniform mode Larmor and anti-Larmor precession coefficients found in the $W_k^{(2)}$ coefficient, given in Eq. (3.79). The butterfly curve's strong dependence on the uniform mode response, also, called the FMR response, is very complicated but can be discussed qualitatively. At the FMR peak where the FMR precession angle is large, the coupling to parametric spin waves is strong, and h_{crit} is at a minimum. As the static field is shifted above or below the FMR field point, the precession angle decreases, the coupling also decreases, and a higher microwave field is needed to reach the instability threshold. Qualitatively, this means that the h_{crit} vs. H profile is an inverted rendition of the low power FMR absorption profile.

The FMR precession angle plays a major role in second order SWI theory and comes out of the calculation for the h_{crit} values. Recall that just at the SWI threshold, energy from the uniform mode is parametrically pumped in to the spin wave modes. This results in a lock-up of the FMR precession angle at ϑ_{FMR}^{crit}. This angle is a maximum at the FMR field. The in-plane FMR precession angle at the FMR field is calculated with Eq. (3.49). For this example calculation the lock-up angle is fairly small at $\vartheta_{FMR}^{crit} = 4.9^{o}$. As one moves above threshold, the lock up gradually relaxes, but there is a sizeable increase in loss.

3.5.2 OBLIQUE PUMPING EXAMPLE CALCULATIONS

This subsection considers example first order SWI results for parallel pumping, oblique pumping, and subsidiary absorption. More specifically, the examples are for coupling angles of $\phi = 0^{o}$, 40^{o}, and 90^{o}. A constant ΔH_k of 32 Oe is used for the calculations. The other parameters used for the calculation are as given above. The available spin wave modes are the same for all three coupling configurations. However, the critical spin wave modes and the threshold vary with ϕ.

Figure 3.8(a) shows the full butterfly curves for $\phi = 0^{o}$, 40^{o}, and 90^{o}, as indicated. The inset shows the coupling configuration. Figures 3.5(b) and (c) show the

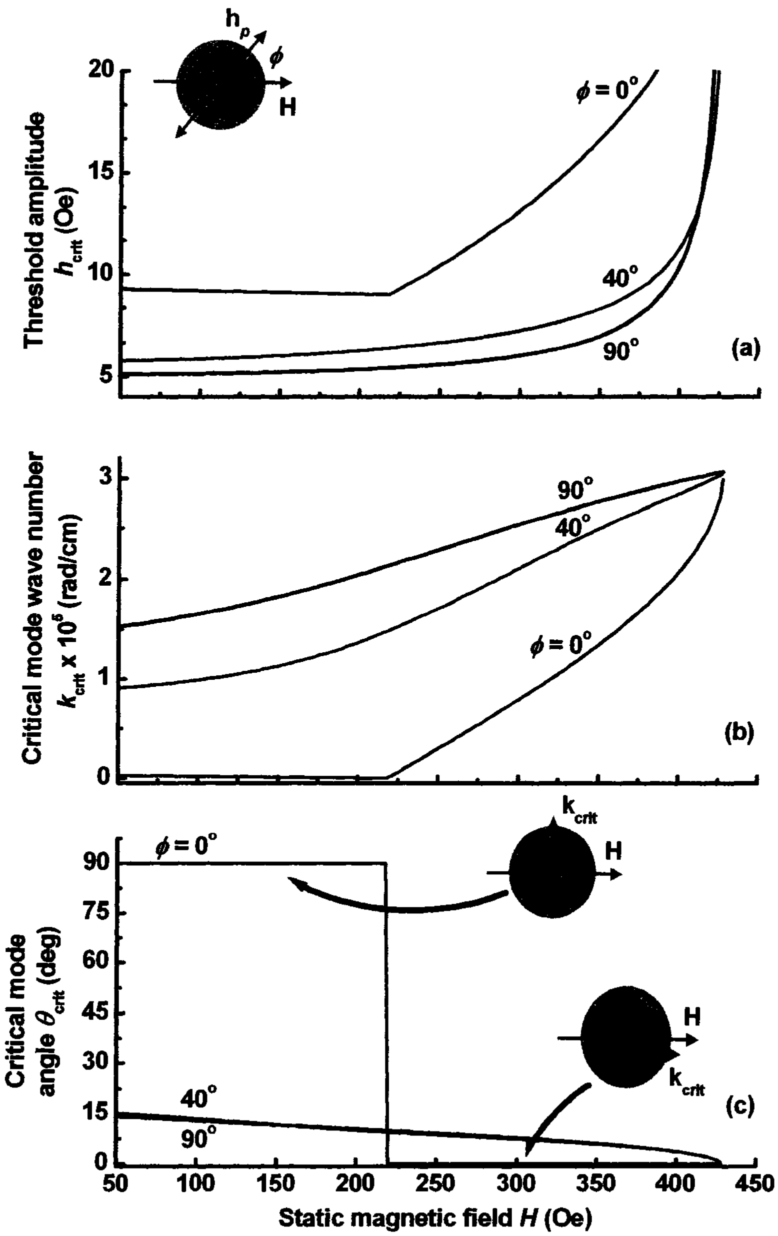

FIG. 3.8. Oblique pumping butterfly curve h_{crit} vs. H and corresponding k_{crit} and θ_{crit} vs. H for angles ϕ between **H** and $\mathbf{h}_p$ of $\phi = 0^{\circ}$, 40°, and 90°, as indicated. The inset in graph (a) shows the coupling configuration. The plots are for the 104 nm thin Permalloy sample and a microwave pumping frequency of 9.11 GHz. Graph (a) shows the h_{crit} vs. H curves. Graphs (b) and (c) show the corresponding k_{crit} and θ_{crit} vs. H curves, respectively. Graph (c) shows the configurations for the $\theta_{crit} = 90^{\circ}$ and 0° critical mode situations.

corresponding graphs of k_{crit} and θ_{crit} vs. H, respectively. The insets indicate the direction of propagation of $\mathbf{k}_{crit}$ with respect to $\mathbf{H}$ or the θ_{crit} for the perpendicular and parallel critical mode angles.

Figure 3.8(a) shows two major effects. The first point of interest is the sharp increase in the threshold amplitudes on the high field sides of the butterfly curves in Fig. 3.8(a). This is directly related to the available spin wave modes at $\omega_k = \omega_p / 2$. Recall from Sec. 3.2.2 that the spin wave dispersion curve shifts up in frequency with an increase of the H field. Above some particular H_{cut}, the $\omega_k = \omega_p / 2$ cut is below the spin wave band and there are no available spin wave modes and no SWI process is possible.

The perpendicular and parallel coupling coefficients found in Eqs. (3.67) and (3.68), respectively, produce different effects at the spin wave band edge where $\theta_{crit} \to 0$. For the case of $\phi = 90^{\circ}$, the $W_k^{(1)\perp}$ coefficient is the only coupling term. Recall that the subsidiary absorption process depends on the coupling of energy through the uniform mode and into spin wave modes. The coupling not only depends on the uniform mode but also on the dipole-dipole and exchange interactions. The $W_k^{(1)\perp}$ is proportional to a $\sin 2\theta_k$ term that stems only from the dipole-dipole interaction. When $\theta_{crit} \to 0$, the dipole-dipole interaction goes to zero, the $W_k^{(1)\perp}$ goes to zero, and the corresponding thresholds diverge.

On the other hand, for the $\phi = 0^\circ$ case, the $W_k^{(1)\parallel}$ coefficient is the only coupling term. Recall that the parallel pumping process depends on an elliptical precession of the dynamic magnetization. The elliptical precession is the result of dipole-dipole interactions. The dependence of $W_k^{(1)\parallel}$ on the dipole-dipole interaction is $(1-N_k)\sin^2\theta_k - N_k$. This shows that when $\theta_{\rm crit} \to 0$, the $\sin^2\theta_k$ goes to zero but the kd – dependent effective demagnetizing factor N_k remains at a nonzero value. The $W_k^{(1)\parallel}$ coefficient then, goes to some finite value at the spin wave band edge and correspondingly the $h_{\rm crit}$ goes to some very large but finite value. For oblique angles, other than 90° and 0°, as $\theta_{\rm crit} \to 0$, the thresholds increase. However the N_k in the $W_k^{(1)\parallel}$ coefficient is nonzero and results in a finite threshold value.

The second effect to be noted from Fig. 3.8(a) is the increase in the $h_{\rm crit}$ values with a decrease in the ϕ angle. Equation (3.70) shows that $h_{\rm crit}$ depends on the perpendicular and parallel components of the $W_k^{(1)\perp}$ and $W_k^{(1)\parallel}$ coefficients weighted by the coupling angle. When ϕ is decreased the coupling of energy into the spin wave modes from the $W_k^{(1)\perp}$ coefficient decreases and the coupling from the $W_k^{(1)\parallel}$ coefficient increases. The increase in threshold as the coupling angle decreases shows that energy is pumped more efficiently by the perpendicular SWI process then by the parallel SWI process.

The $W_k^{(1)\perp}$ coefficient dominates the coupling of energy into the spin wave modes up to some critical ϕ_c angle. This critical angle occurs when $W_k^{(1)\parallel}\cos\phi_c = W_k^{(1)\perp}\sin\phi_c$ and is $\phi_c = 31^\circ$. The butterfly curves for $\phi > \phi_c$ have lower thresholds, as there is a strong coupling of energy through the uniform mode and into the spin wave modes. The butterfly curves for $\phi < \phi_c$ have increasingly higher thresholds which are the result of the weak coupling of energy directly from the h_p field into the spin wave modes.

Figures 3.8(b) and (c) show the corresponding k_{crit} and θ_{crit} vs. H graphs. The $\phi = 0^\circ$ plots show very low k_{crit} and $\theta_{\text{crit}} = 90^\circ$ up to some field value. This field value corresponds to the minimum in the $\phi = 0^\circ$ butterfly curve. As one increases the field, the k_{crit} values decrease with the $\theta_{\text{crit}}\,90^\circ$ spin wave dispersion branch. At the minimum field value, k_{crit} is about zero as θ_{crit} abruptly jumps to zero. At this field the half pump frequency line includes the $k = 0$ spin wave mode. As one increases the field above the minimum, there is an increase in the k_{crit} values as θ_{crit} remains at zero until the spin wave band edge. At the band edge, the k_{crit} value approaches some finite value that is the only available mode when the half pump frequency is at the very bottom of the spin wave band.

The $\phi = 90^\circ$ and $\phi = 40^\circ$ curves show a different trend. The θ_{crit} values for both curves show a maximum value of about 15° at low fields. The curves then show an almost identical smooth decrease to zero at the band edge. The corresponding k_{crit}

values for both curves are on the order of 10^6 rad/cm and show a relatively smooth increase to the finite k_{crit} value at the band edge.

The difference in the spin wave modes for the larger angles, $\phi = 90^{\circ}$ and $\phi = 40^{\circ}$, to $\phi = 0^{\circ}$ stems from the coupling coefficients. Recall that for coupling angles greater than $\phi_c = 31^{\circ}$, the $W_k^{(1)\perp}$ coefficient dominates and the critical spin wave modes show only small changes. For coupling angles smaller than $\phi_c = 31^{\circ}$, the $W_k^{(1)\parallel}$ coefficient dominates and the critical modes are drastically different. The behavior and range of the critical modes for the subsidiary absorption and parallel pumping processes are very different.

REFERENCES

[An *et al.* (2004)] S. Y. An, P. Krivosik, M. A. Kramer, H. M. Olson, A. V. Nazarov, and C. E. Patton, J. Appl. Phys. **96**, 1572 (2004).

[Arfken and Weber (2001)] G. B. Arfken and H. J. Weber, *Mathematical Methods for Physicists* (Harcourt/Academic Press, San Diego, 2001).

[Arias and Mills (1999)] R. Arias and D. L. Mills, Phys. Rev. B **60**, 7395 (1999).

[Ashcroft and Mermin (1976)] N. W. Ashcroft and N. D. Mermin, *Solid State Physics* (Harcourt, Inc., 1976).

[Chen and Patton (1994)] M. Chen and C. E. Patton, in *Nonlinear Phenomena and Chaos in Magnetic Materials*, edited by Wigen (World Scientific, Singapore, 1994), Ch. 3 Spin wave instability processes in ferrites.

[Gilbert (1955)] T. A. Gilbert, Technical Report No. 11, (unpublished) 1955.

[Green *et al.* (1969)] J. J. Green, C. E. Patton, and E. Stern, J. Appl. Phys. **40**, 172 (1969).

[Harte (1968)] K. J. Harte, J. Appl. Phys. **39**, 1503 (1968).

[Jackson (1999)] J. D. Jackson, *Classical Electrodynamics* (John Wiley and Sons, Inc., 1999).

[Kalinikos and Slavin (1986)] B. A. Kalinikos and A. N. Slavin, J. Phys. C **19**, 7013 (1986).

[Kambersky and Patton (1975)] V. Kambersky and C. E. Patton, Phys. Rev. B **11**, 2668 (1975).

[Kittel (1948)] C. Kittel, Phys. Rev. **73**, 155 (1948).

[Krivosik (2007)] P. Krivosik, Private communication, 2007.

[Landau and Lifshitz (1935)] L. Landau and E. Lifshitz, Phys. Z. Sowjet Union **8**, 153 (1935).

[McMichael and Krivosik (2004)] R. D. McMichael and P. Krivosik, IEEE Trans. Magn. **40**, 2 (2004).

[Nazarov *et al.* (2002)] A. V. Nazarov, C. E. Patton, R. G. Cox, L. Chen, and P. Kabos, J. Magn. Magn. Mater. **248**, 164 (2002).

[Nisenoff and Terhune (1965)] M. Nisenoff and R. W. Terhune, J. Appl. Phys. **36**, 732 (1965).

[Olson *et al.* (2007)] H. M. Olson, P. Krivosik, K. Srinivasan, and C. E. Patton, J. Appl. Phys. **102**, 023904 (2007).

[Patton (1968)] C. E. Patton, J. Appl. Phys. **39**, 3060 (1968).

[Patton (1969)] C. E. Patton, J. Appl. Phys. **40**, 2837 (1969).

[Patton (1975)] C. E. Patton, in *Magnetic Oxides*, edited by Craik (Wiley, London, 1975), p. 575-645, Ch. 10 Microwave resonance and relaxation.

[Patton (1979)] C. E. Patton, Phys. Status Solidi B 92, 211 (1979).

[Schloemann (1959)] E. Schloemann, Technical Report No. R-48, (unpublished) 1959.

[Schloemann *et al.* (1963)] E. Schloemann, R. I. Joseph, and I. Bady, J. Appl. Phys. **34**, 672 (1963).

[Sparks (1964)] M. Sparks, *Ferromagnetic Relaxation Theory* (McGraw-Hill, 1964).

[Suhl (1957)] H. Suhl, J. Phys. Chem. Solids **1**, 209 (1957).

[Vendik *et al.* (1977)] O. G. Vendik, B. A. Kalinikos, and D. N. Chatorizhskii, Fiz. Tverd Tela **19**, 387 (1977).

[Wames and Wolfram (1970)] R. E. D. Wames and T. Wolfram, J. Appl. Phys. **41**, 987 (1970).

- 4 -

PERMALLOY THIN FILM MATERIALS OVERVIEW

INTRODUCTION

This chapter provides an overview of the thin Permalloy films of interest. Sec. 4.1 provides basic information on the samples, such as thickness, composition, and preparation details. Section 4.2 and 4.3 present the static and microwave magnetic properties of the films, respectively.

4.1 THIN PERMALLOY FILMS

The focus of this work is on Permalloy films of thicknesses (d) 35, 57, 74, 104 and 123 nm prepared by Dr. S. Konishi, Kyushu University, Fukuoka, Japan in the 1970's. The films were thermally evaporated on 8 mm square, 0.2 mm thick glass substrates in the presence of an in-plane static magnetic field of about 30 Oe. The nominal vacuum before evaporation was 2×10^{-6} Torr, during evaporation was 8×10^{-6} Torr, and during the annealing process was 2×10^{-6} Torr. The 35 and 104 nm thin films were evaporated on glass substrates held at ambient room temperature.

The 57, 74, and 123 nm thin films were evaporated and annealed on heated glass substrates at about 300^{o} C. The time of the annealing process was about two hours. All films are 5 mm in diameter and have nominal compositions of 82 at. % Ni and 18 at. % Fe.

There was no overlayer deposited on the samples. It is possible that an oxide layer developed on the films after preparation. No measurements were performed to verify an oxide layer. Silicone vacuum grease was used by Dr. Konishi's research group to hold the samples in place and is used for the same purpose for the work presented here.

4.2 THIN PERMALLOY FILM STATIC MAGNETIC PROPERTIES

The static magnetic properties of the thin Permalloy films were determined from calibrated hysteresis loop measurements by Dr. Konishi's research group in the 1970's. The coercive values reported for the samples were very low and in the range of 2 – 4 Oe. The 104 and 123 nm films evidenced the usual field induced uniaxial anisotropy with effective anisotropy fields of 5 and 4 Oe, respectively. The external field is used to align the easy axes of the magnetic domains.

Figure 4.1(a), (b), (c), and (d) show magnetic moment vs. H curves for the 35, 57, 74, and 123 nm samples, respectively. These measurements were performed recently by Dr. Sangita Kalarickal at NIST in Boulder, Colorado [Kalarickal (2007)]. The measurements were performed with a B-H looper with the static magnetic field

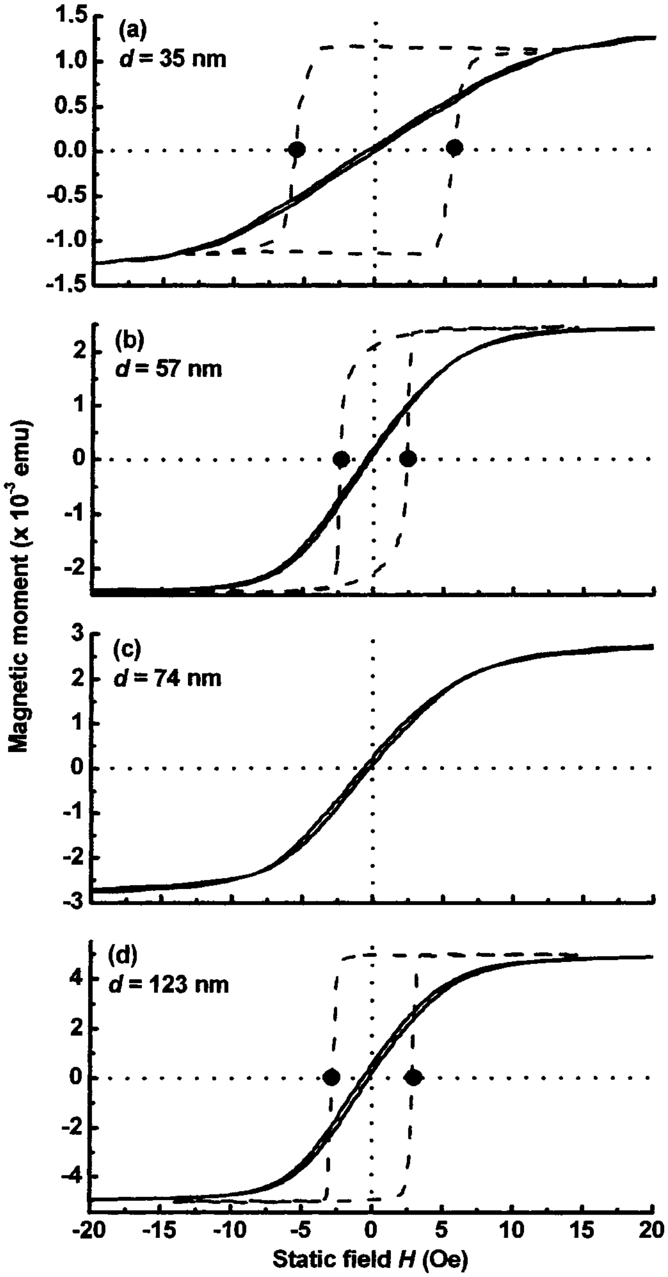

FIG. 4.1. Magnetic moment vs. H for the 35, 57, 74, and 123 nm samples, as indicated. The solid and dashed curves correspond to measurements with the static field along the hard axis and easy axis of the sample, respectively. No easy axis measurement was made for the 74 nm thin sample. The solid circles, in graphs (a), (b), and (d), indicate the coercive values for the samples. These data were provided by Dr. Sangita Kalarickal.

in the film plane. The solid curves were measured with the static field along the easy axis and the dashed curves were measured with the static field along the hard axis of the sample. Notice that no easy axis measurement was taken for the 74 nm film. The solid circles, in graphs (a), (b), and (d) indicate the coercive values for the samples. The coercive values extracted for the 35, 57, and 123 nm thin films are 5.7, 2.4, and 2.8 Oe, respectively. These agree reasonably well with the values measured by Dr. Konishi's research group.

The effective anisotropy fields extracted from the hard axis data are 12, 7.1, 7.4, and 5.8 Oe for the 35, 57, 74, and 123 nm thin films, respectively. These values are notably larger than the values measured by Dr. Konishi's research group. It is important to note that Dr. Konishi's research group only reported the effective anisotropy value for the 104 and 123 nm films. The 123 nm film was the only sample measured in both cases. The effective anisotropy values are much smaller than the fields of interest and the films were taken as isotropic for purposes of analysis.

4.3 THIN PERMALLOY FILM MAGNETIC MICROWAVE PROPERTIES AND DERIVED PARAMETERS

All five samples showed FMR responses. The basic FMR properties were determined by standard low power measurements for both in-plane and perpendicular-to-plane static field configurations. The FMR measurement details are given in Ch. 5.

Figure 4.2 shows example cavity voltage reflection coefficient ρ vs. H low power FMR profiles for the 104 nm film and a microwave frequency of 9.11 GHz. Recall that $\rho = (P_{\text{ref}} / P_{\text{in}})^{1/2}$ and is a measure of loss due to the sample. Graph (a) and (b) show in-plane and perpendicular-to-plane static field FMR profiles, respectively. The dashed line and solid point indicate the in-plane and perpendicular-to-plane FMR fields $H_{\text{FMR}}^{\parallel} = 830$ Oe and $H_{\text{FMR}}^{\perp} = 14{,}494$ Oe, respectively. The solid curves show Lorentzian fits to the FMR profiles. In spite of

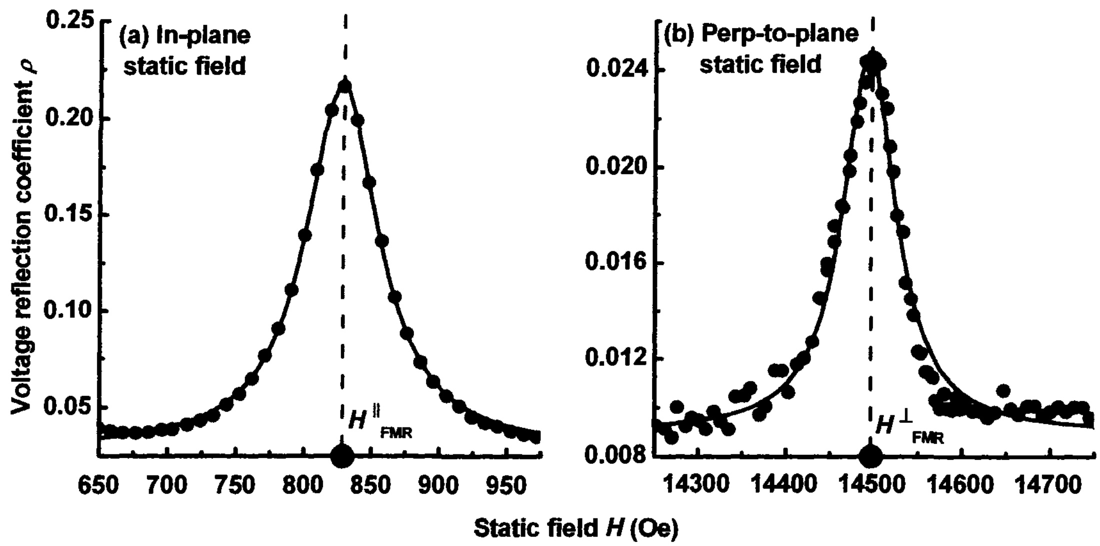

FIG. 4.2. Voltage reflection coefficient ρ vs. H for the 104 nm thin film and a microwave frequency of 9.11 GHz. The H and h_p fields were mutually perpendicular at $\phi = 90^{\circ}$. Graph (a) is for the microwave and static fields in the film plane. Graph (b) is for the microwave field in the film plane and the static field perpendicular to the film plane. The solid curves show Lorentzian fits to the data. The ferromagnetic resonance points are as indicated.

the age of these films, the low power in-plane and perpendicular-of-plane FMR profiles were all clean and reasonably narrow. These FMR profiles are typical for all of the films.

The shift of the FMR peak from low field for the in-plane configuration to a higher field for the perpendicular-to-plane configuration is due to the demagnetizing fields in the film. The perpendicular-to-plane FMR Kittel formula is $\omega_p = |\gamma|(H^{\perp}_{\mathrm{FMR}} - 4\pi M_s)$. Here the $-4\pi M_s$ is due to the static demagnetization and reduces the static field inside the film. As a result, a larger field is required to meet the resonance condition. The in-plane FMR Kittel formula is $\omega_p = |\gamma|\sqrt{H^{\parallel}_{\mathrm{FMR}}(H^{\parallel}_{\mathrm{FMR}} + 4\pi M_s)}$. Here the $4\pi M_s$ is due to the dynamic demagnetizing field that is produced when the magnetization is tipped out of the film plane. This produces an additional torque on the magnetization. As a result, a smaller field is required to meet the resonance condition [Patton (1968)].

Table 4.1 lists the key FMR results measured for all five films. The $H^{\parallel}_{\mathrm{FMR}}$ and $H^{\perp}_{\mathrm{FMR}}$ values, as listed in table 4.1, were used to determine the effective saturation induction $4\pi M_{s\text{-eff}}$ and the gyromagnetic constant $|\gamma|/2\pi$ parameters from the in-plane and perpendicular-to-plane standard FMR Kittel formulas discussed above. Small surface anisotropy effects make $4\pi M_{s\text{-eff}}$ slightly different from the actual saturation induction, $4\pi M_s$. The listed $4\pi M_{s\text{-eff}}$ and $|\gamma|/2\pi$ values match reasonably well to literature values for the $4\pi M_s$ and the $|\gamma|/2\pi$ for Permalloy [Patton (1968), Kalarickal *et al.* (2006)].

TABLE 4.1. Summary of low power 9.11 GHz ferromagnetic resonance (FMR) measurements and derived parameters.

Film thickness d (nm)	FMR field H_{FMR} (Oe)	
	In-plane static field	Perpendicular-to-plane static field
35	806	13,878
57	838	13,591
74	782	14,275
104	830	14,494
123	850	13,560

Effective saturation induction $4\pi M_{\text{s-eff}}$ (G)	Gyromagnetic constant $\|\gamma\|/2\pi$ (MHz/Oe)	In-plane half power FMR linewidth ΔH_{FMR} (Oe)	In-plane equivalent Gilbert damping parameter α_{FMR}
10,820	2.976	44	0.0072
10,510	2.954	41	0.0066
11,210	2.974	37	0.0060
11,320	2.869	59	0.0093
10,460	2.938	56	0.0090

The last two columns give the measured in-plane half power FMR linewidths (ΔH_{FMR}). The Gilbert damping parameters (α_{FMR}) that correspond to the ΔH_{FMR} values were obtained from the standard connection derived from the Gilbert damped equation of motion $\alpha_{\mathrm{FMR}} = |\gamma| \Delta H_{\mathrm{FMR}} / 2\omega_p$, as discussed in Ch. 3, where

$\omega_p / 2\pi = 9.11$ GHz. The reasonably small linewidths and low α_{FMR} values are indicative of good quality low loss films. Dr. Konishi's research group also measured the in-plane linewidths of these samples in the 1970's and obtained values within 5 Oe of the linewidths measured found here.

REFERENCES

[Kalarickal et al. (2006)] S. S. Kalarickal, P. Krivosik, W. M., C. E. Patton, M. L. Schneider, P. Kabos, T. J. Silva, and J. P. Nibargar, J. Appl. Phys. **99**, 093909 (2006).

[Kalarickal (2007)] S. S. Kalarickal, Private communication, 2007.

[Patton (1968)] C. E. Patton, J. Appl. Phys. **39**, 3060 (1968).

HIGH POWER FERROMAGNETIC RESONANCE SYSTEM, EXPERIMENTAL TECHNIQUES, EXAMPLE DATA, AND THEORETICAL FITS

INTRODUCTION

In this chapter the newly developed automated high power FMR spectrometer system and the extensive new calibration techniques are discussed. The experimental techniques are modified from previous techniques to improve the accuracy of the data and decrease the time for data acquisition. Example data and theoretical fits are provided.

Previous high power FMR systems provided invaluable spin wave relaxation information. One such system was discussed in Patton and Green (1971). The new modernized high power FMR system is capable of fully automated threshold measurements over a span of static magnetic fields. This automation greatly decreased the time to obtain the data needed for a full butterfly curve by over 75%. A traveling wave tube amplifier is used rather than a magnetron. The solid state technology provides a faster rise time and does not show the distortion seen in pulses generated by magnetrons. A microwave switch is no longer used, as the incident power and reflected power at the cavity are accurately determined through a series of calibrations. A computer, rather than a calibrated data recorder, is used for data acquisition and to perform calculations to accurately determine the necessary parameters.

In addition to the new high power FMR system, new calibration techniques were developed to accurately measure the system loss and to resolve cavity calibration issues over the FMR field range. The precise measurement of the loss throughout the system is performed as a function of frequency. This accounts for the changes in loss and, hence, in changes in the incident power at the cavity P_{in} and the reflected power from the cavity P_{ref} due to changes in the microwave pumping frequency for field swept FMR measurements. The procedure to find the microwave field amplitude inside the microwave cavity is presented in detail by Green and Kohane (1964), Frait and Patton (1980), and McKinstry and Patton (1989). This procedure is extended to allow for proper calibration over the FMR profile.

These new calibration techniques have not only improved the accuracy of the measurements but also have allowed for the first ever full set of accurately calibrated high power data to be measured over the full FMR field range. Previous calibrated measurements over just a portion of the FMR field range were performed by Cox *et al.* (2001). These took into account cavity loading due to sample absorption.

However, the dependence of the cavity calibration on loss was not taken into account. This can (and does) lead to significant errors.

Section 5.1 introduces the high power system design and instrumentation. Section 5.2 presents the calibration technique for the loss in the system. Section 5.3 develops the techniques to perform low and high power FMR measurements and provides example FMR results. It should be mentioned that the system calibration provides accurate P_{in} and P_{out} values for the FMR measurements but there is still no one-on-one correspondence between the P_{in} and the microwave field amplitude in the cavity h_p. Section 5.4 gives details on the decoupling of the cavity and further calibration issues. In addition, perturbation theory to obtain the equation for the cavity calibration constant is introduced. Section 5.5 establishes methods to determine the microwave SWI threshold amplitude h_{crit} and other important parameters. Section 5.6 gives example butterfly curve results for resonance saturation and oblique pumping and establishes the procedures for the theoretical analyses of these results.

5.1 HIGH POWER FERROMAGNETIC RESONANCE MICROWAVE SPECTROMETER SYSTEM

The purpose of the high power FMR microwave spectrometer system is to measure the magnetic losses in a sample at low and high powers. As discussed in Ch. 2, the losses are presented in terms of the voltage reflection coefficient ρ. The high power FMR system is designed to perform two types of loss measurements. The first is uncalibrated absorption profiles of ρ vs. H for a range of P_{in} values. The second type is uncalibrated and calibrated threshold curve profiles of ρ vs. P_{in} for a range of H values. As mentioned, the term "uncalibrated" means that the data are obtained under cavity loading conditions for which the connection between P_{in} and h_p is not fixed. This is generally the case in the FMR field region when the static and microwave fields are mutually perpendicular and the FMR coupling is strong. Through a reduction in the coupling angle ϕ between these fields, the coupling is reduced to the point where perturbation theory is applicable and one can define $C = h_p^2 / P_{in}$ for the sample loaded cavity and make the transition to a "calibrated" measurement.

The high power X-band pulsed microwave reflection cavity spectrometer system is similar to the systems described by Cox *et al.* (2001), Nazarov (2002), and Zhang *et al.* (1987). A schematic diagram of the basic system is shown in Fig. 5.1. The spectrometer is divided up into seven separate sections for this discussion. The sections are the high power pulsed microwave source, the input arm, the reference arm, the reflection arm, the electromagnet, the microwave reflection cavity that contains the sample, and the computer for data acquisition

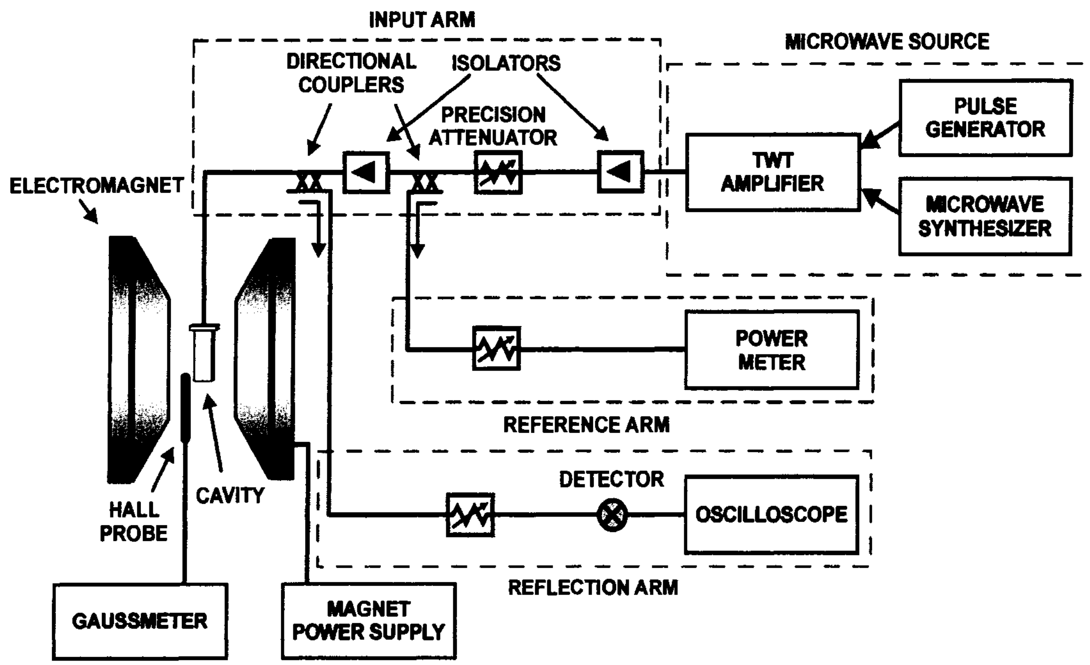

FIG. 5.1. Schematic diagram of the high power FMR spectrometer system.

and automation. The first four sections are shown in red dashed line boxes in Fig. 5.1. The first section of the high power FMR system is the high power pulsed microwave source. It consists of three major components that are all computer controlled by a General Purpose Interface Bus (GPIB) card. These include a Hewlett Packard (HP) 83640A synthesized sweeper, a Wavetek Model 81 pulse generator, and an Applied Systems Engineering Model 174XKu traveling wave tube (TWT) amplifier. The TWT is provided with a -4 dBm continuous microwave signal from the synthesized sweeper and a 4 V gate signal from the pulse generator. The signal from the pulse generator triggers the TWT to generate a linearly polarized microwave pulse with a peak power of approximately 2 kW and a maximum duty cycle limit of 4%. The repetition frequency is 40 Hz and the pulse rise time is about 100 ns.

It is important to note that the SWI threshold accuracy is adversely affected if the microwave pulse width is not set properly. For data in this dissertation, the pulse frequency was fixed at 40 Hz and the pulse width was the only duty cycle variable. The determination of the proper pulse width is of very important. Too large of a pulse width results in sample heating [McKinstry *et al.* (1985)]. The effect of sample heating is observed as a slow visible increase in the crystal detector voltage for a set input power. For a pulse width that is too short, there is not adequate time for the microwave field in the cavity to reach maximum amplitude. Additionally, the width must be larger than the characteristic time for the spin wave instability process to occur [Schloemann *et al.* (1960)]. If this condition is not satisfied, a larger input power is required for the instability process to be observed. This results in an increase in the measured threshold values. The standard pulse width for the resonance saturation measurements was 4 μs and for oblique pumping was 6 μs.

The next section is the input arm. This consists of two high power isolators and the high power variable precision attenuator, as shown in Fig. 5.1. A Raytheon 1XH7 high power isolator positioned directly after the microwave source provides protection to the TWT from reflected power. The isolator positioned between the directional couplers helps to prevent the formation of standing modes in the waveguide. The HP X382A precession attenuator controls the input power to the microwave system and is computer controlled. This allows for the input power to be remotely controlled for power swept measurements.

The third and fourth sections of the high power system are the reference and reflection arms, as indicated in Fig. 5.1. These arms are used to monitor the incident and reflected power to the cavity, respectively. The reference arm is coupled to the input microwave line through a 20 dB directional coupler and is terminated with a HP 8481A power meter head. The microwave power incident on the power meter head is measured by a HP 436A power meter.

For the reflection arm, the termination point is at a HP 8474D microwave crystal detector for the resonance saturation measurements, or a Herotek DHM124AB for the oblique pumping measurements. The voltage signal from the crystal detector is sent to a Tektronix TDS410A digitizing oscilloscope, which is triggered by the pulse generator, for data acquisition.

The reference and reflection arms both have HPX382 variable precession attenuators that are computer controlled through a series of stepper motors. These motors are calibrated to provide the required attenuation. The attenuators are varied to provide adequate protection from high microwave powers to the power meter head and the crystal detector. The computer control provides continuous protection to the detectors for power swept measurements. Additionally, the power meter and oscilloscope readings are acquired by the computer.

The next section of the high power system consists of the electromagnet that provides the adjustable **H** field and the instruments required for operation. The electromagnet has variable size pole pieces and can be rotated about an axis perpendicular to the floor. This allows the direction of the magnetic field to be changed with respect to the microwave magnetic field direction in the cavity. The electromagnet is powered by a Walker LDJ Scientific HS-1050-4SS current regulated power supply. The magnetic field is measured by a Lake Shore 450 gaussmeter. The magnetic field is computer controlled and measurements with the gaussmeter provide a means to fine tune to the requested field. The maximum magnetic field strength is about 8.5 kOe for a 4 inch magnet gap and about 20 kOe for a 1.25 inch magnet gap. The magnet and power supply are water cooled by a NESLAB System I water cooler.

The sixth section of the high power system is comprised of a microwave reflection cavity. The cavity is centered between the magnet pole pieces of the electromagnet. Measurements were made with two different microwave cavities. The first was a TE_{102} cavity with a nominal center frequency f_p of 9.11 GHz, a power reflection coefficient of -30 dB at the cavity resonance, and a loaded quality factor Q_L of 2600. The second cavity was a TE_{110} cylindrical cavity with $f_p = 9.58$ GHz, a power reflection coefficient of -36 dB at the cavity resonance, and $Q_L = 11,300$.

Figure 5.2 shows a schematic diagram of the two reflection cavities and the microwave fields in the cavities. The arrows indicate the incident power on the cavity P_{in} and the reflected power from the cavity P_{ref}. The height h and width w and the radius r and width l of the rectangular and cylindrical cavities, respectively, and the maximum h_p amplitude points of interest in the cavities are indicated.

For the application here, undercoupled cavities are used. For an undercoupled cavity, an increase in the cavity loss results in an increase in the reflection from the

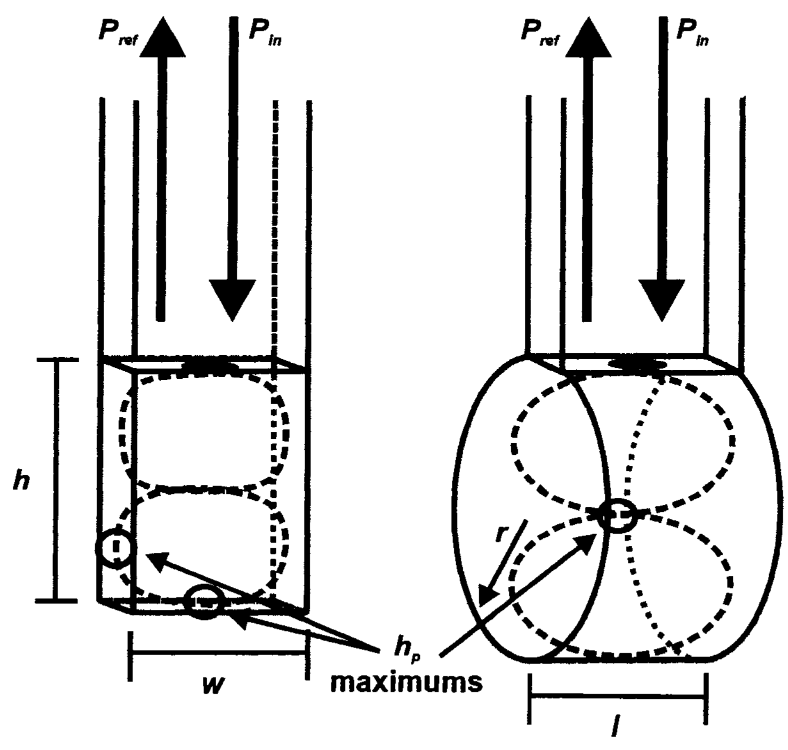

FIG. 5.2. Schematic diagram of the microwave reflection cavities and microwave fields h_p inside the cavities. Graph (a) shows the TE_{102} rectangular cavity with a resonance frequency of 9.11 GHz and graph (b) shows the TE_{011} cylindrical cavity with a resonance frequency of 9.58 GHz. The h_p maximum points are indicated. The height h and width w and the radius r and width l of the rectangular and cylindrical cavities, respectively, are indicated. The arrows represent the input P_{in} and output P_{ref} microwave powers.

cavity. The low Q_L of the TE_{102} cavity results in a 0 – 20 Oe microwave field range that is required for the resonance saturation measurements. The large Q_L of the TE_{011} cavity results in microwave fields in the 0 – 120 Oe range that are necessary for oblique pumping measurements.

Additionally, both cavities had fixed irises. Any change in the Q_L of the cavity, therefore, tracks the sample loss. The calibration techniques to determine the coefficient $C = h_p^2 / P_{\mathrm{in}}$ that connects the P_{in} to the h_p at the sample position are discussed below.

The samples are placed at maximum points of the microwave field amplitude, as shown in Fig. 5.2. For low power out-of-plane FMR measurements, the rectangular cavity is used with the sample three quarters down the side wall of the cavity. For in-plane low power and high power measurements, the sample is positioned such that the $\mathbf{H}$ and $\mathbf{h}_p(t)$ fields are in-plane. This corresponds to the bottom of the rectangular cavity and the center of the cylindrical cavity. The rectangular cavity is a split cavity. The bottom quarter of the cavity is removed to place the sample in the cavity. The cylindrical cavity has a removable post attached to a rexolite rod at the center of the side wall of the cavity that is removed to place the sample in the cavity. In both cavities, the sample is held in place by a thin layer of vacuum grease.

The sample positions along with in-plane static magnetic field rotation provided by the electromagnet provide full control of the orientation of the $\mathbf{h}_p(t)$ and the $\mathbf{H}$

fields in relation to the sample and one another. This capability is important for oblique pumping and resonance saturation measurements as discussed below.

The final section of the system consists of the cables, utilities, and computer used for data acquisition and automation of the high power FMR system. All instrument communication for data acquisition and automation is performed through a GPIB card installed in the computer. The programming language used is Labview 7.1®. The software has been updated to provide faster data acquisition times and to perform fully automated threshold measurements over a range of static fields.

5.2 HIGH POWER SYSTEM CALIBRATION

Three steps are required to calibrate the high power FMR system. Cavity calibration is covered separately in Sec. 5.4. Figure 5.3 shows a flow chart of the necessary steps for system calibration. The first step is the crystal detector calibration. This calibration determines the correspondence between the input power and the output voltage from the crystal detector. The second step determines the microwave losses in the reference and reflection arms [Nazarov (2002)]. This provides a means to convert from the measured powers at the power meter and crystal detectors to the actual P_{in} and P_{ref} at the cavity position, respectively. Finally, a calibration of the high power precision attenuators provides the actual attenuation for a particular setting. These calibrations provide accurate values of the input and reflected power at the cavity position.

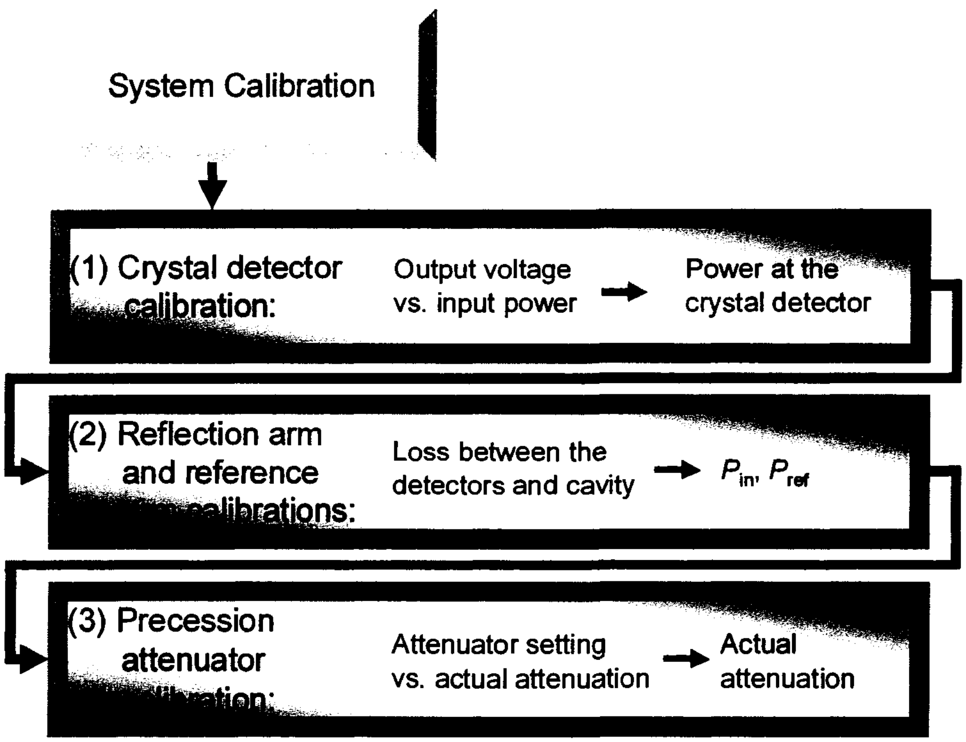

FIG. 5.3. Flow chart of the steps for the system calibration.

The first step is the crystal detector calibration. For this portion of the calibration, the crystal detector is connected directly to the synthesized sweeper. The microwave frequency is set to the cavity resonance frequency and the output power is swept from approximately -20 – 15 dBm. It is important to note that the power range of the calibration depends on the parameters of the particular crystal detector used. The crystal detector is then replaced with the power meter head and the power is again swept over the specified power range. A file is created that contains the conversion from the crystal detector voltage to the power input to the crystal detector. Typically the power is roughly proportional to the voltage squared.

The second step is to measure the reference and reflection arm losses. In particular, these are the losses between the cavity position and the positions of the power meter head and crystal detector, respectively. For this step a short is positioned at the cavity position and the remainder of the system is setup as shown in Fig. 5.1. A small frequency range centered at the cavity resonance frequency is chosen. The powers at the crystal detector and power meter head positions are then measured as a function of frequency. The short is then replaced by the power meter head. The power at the cavity iris position is then measured as a function of frequency. The losses between the reflection arm and the cavity and the reference arm and the cavity are calculated and recorded in calibration lookup files.

The third and final step is the calibration of the high power precision attenuators. The attenuators are rated for attenuation in the range 0 – 50 dB. However, the dials on the attenuators are not properly calibrated. For this calibration an HP 8510C Vector Network Analyzer is used to measure the actual attenuator values. The measured attenuation values and the dial values are written to calibration lookup files for each of the three attenuators. Typically the actual measured attenuator values are well within 1 dB of the attenuator settings but, for large attenuation the values can differ as much as 10 dB.

It is important to mention the errors in the measurements and how they propagate. There are three sources of error that influence the P_{ref} measurement. The first is the expected experimental error associated with the measurement of the voltage from the crystal detector. The second is the error introduced from the calibration of the crystal detector. The final source of error is from the loss calibration to find P_{ref} at the cavity. This includes the error from the reference arm attenuator. These errors have been reduced through a number of measures. For example, the voltage is measured multiple times for each data point and averaged to reduce random error, the reference arm loss calibration takes into account changes in the frequency, and the attenuator is calibrated to provide the actual attenuation value.

The errors that influence the P_{in} measurement are similar, with the exception that the power is measured by a power meter and not a crystal detector. The power meter measures only the average power. To calculate the peak power, it is assumed that the power is constant over the pulse. The pulse was observed by the use of the crystal detector and power over the pulse was seen to be approximately constant. The main error stems from the accuracy of the power meter. The error in ρ for all measurements was always at or below $\delta\rho = \pm 0.001$.

5.3 QUALITATIVE HIGH POWER FERROMAGNETIC RESONANCE PROFILES

This section introduces the procedure to obtain uncalibrated high power absorption profiles and provides example absorption profiles. Here "uncalibrated" means that the data were obtained under cavity loading conditions for which the connection between P_{in} and h_p was not fixed and ρ is not a measure of the imaginary part of the susceptibility. This is generally the case when the static and microwave fields are mutually perpendicular and the FMR coupling is strong. This is discussed in Sec. 5.4. This section continues the introductory discussion of the high power effects on the absorption profiles in the regions of FMR and below FMR, as presented in Ch. 2.

The configuration of the system for the measurement of the FMR response profiles is shown in Fig. 5.1. The system calibration, as presented in Sec. 5.2, must be fully performed before the measurements can be made. A low or high P_{in} value is selected with the use of the main attenuator. The reference and reflection arm attenuators are set to provide adequate protection to the power meter head and crystal detector, respectively, and a proper duty cycle is chosen to prevent cavity heating. The H range for the measurement and H step size are selected.

For high power measurements over the FMR region, the cavity resonance frequency changes as the H field is swept. At each H field point the cavity resonance frequency is measured and the microwave frequency is set accordingly. The P_{in} and P_{ref} are measured and the ρ is calculated. This process is repeated for the selected H range to obtain the full absorption profile. A data file is written that includes all the input parameters and acquired data. This procedure is repeated for different P_{in} values to observe the effect of power on the absorption profiles.

Two different sets of high power absorption profiles are shown below. The first set of data are in the field range of the FMR profile and shows the resonance saturation effect. The second set of data are for a range of H fields well below FMR and shows the subsidiary absorption effect.

Figure 5.4 shows example high power resonance saturation response profiles for the 104 nm film. These data were taken at $f_p = 9.11$ GHz. The graph shows data on ρ vs. H for P_{in} values of 0.44, 13, and 85 W, as indicated. The static and microwave fields were in-plane and mutually perpendicular at $\phi = 90^{\circ}$, as shown in

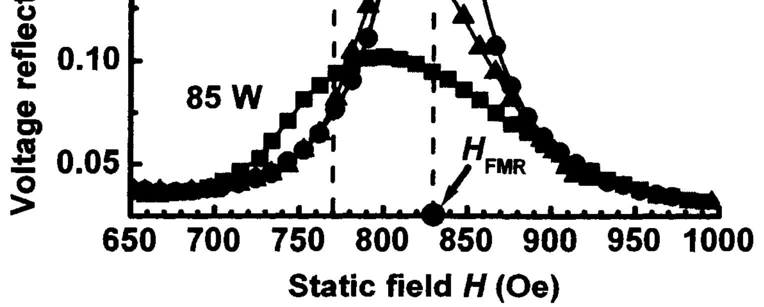

FIG. 5.4. Voltage reflection coefficient ρ vs. H resonance saturation profiles for the 104 nm thin film, the in-plane static field configuration, and a microwave frequency of 9.11 GHz. The symbols show data for different P_{in} values, as indicated. The dashed lines show cuts at 830 Oe, the FMR field H_{FMR} line cut A, and B at a lower field value of 770 Oe. The H field the h_p field were in-plane and mutually perpendicular at $\phi = 90^{\circ}$, as shown in the inset.

the diagram inset. The vertical dashed line at H_{FMR}, labeled A, and the off resonance line, labeled B, correspond to H values of 830 and 770 Oe, respectively. These lines show ρ vs. P_{in} cuts at fixed H that are useful for the cavity calibration and threshold curve discussions in Secs. 5.4 and 5.5, respectively. It is important to emphasize that these FMR curves are obtained at full coupling, or for $\phi = 90^{\circ}$.

As noted, the ferromagnetic resonance field H_{FMR} in Fig. 5.4 is at 830 Oe and ΔH_{FMR} is about 59 Oe. This ΔH_{FMR} is the half power linewidth. It is important to note that ΔH_{FMR} is not the same as the $\rho/2$ linewidth. Nevertheless, the qualitative changes in the profiles as P_{in} is increased provide an indication of the overall nonlinear response. The profile for $P_{\mathrm{in}} = 13$ W is broader, lower in amplitude, and slightly asymmetric, relative to the low power profile. The asymmetry amounts to a shift of the profile to lower fields and a development of a low field shoulder. This trend continues to an even greater extent for the $P_{\mathrm{in}} = 85$ W profile.

As discussed in Ch. 2, the decrease in amplitude and broadening of the FMR peak with increasing power is the basic resonance saturation response associated with second order SWI processes. It is important to keep in mind that such processes occur for power levels well below those for which saturation effects are expected from classical theory. It is also important to note that the change in ρ with increasing power at a fixed field is not a continuous effect. Calibrated data on ρ vs. h_p, to be considered in Sec. 5.5, show that the change in reflection coefficient occurs more-or-less abruptly at some threshold h_p value. It is this change that defines the threshold microwave field amplitude h_{crit}.

The shift to low field and the development of the low field shoulder with increasing power is the manifestation of a foldover effect for metal films. The asymmetry development also leads to a kink in the butterfly curve, h_{crit} vs. H profile, at a field somewhat below the minimum H point. The foldover shifts the high field response to a lower field and the nonlinear broadening increases the high field response to higher fields. The combination of these produces high field responses that appear to be independent of power with no measurable threshold. Preliminary work suggests that the foldover is due to two-magnon scattering interactions [Krivosik (2006)].

Figure 5.5 shows example subsidiary absorption (SA) response profiles for the 104 nm thin film. These data were taken at $f_p = 9.58$ GHz. The graph shows data on ρ vs. H for P_{in} values of 0.40, 5.0, and 25 W, as indicated. The static and microwave fields were in-plane and mutually perpendicular at $\phi = 90^{\circ}$, as shown in the diagram inset. The vertical dashed line labeled C, corresponds to an H value of 280 Oe. This line shows a ρ vs. P_{in} cut at fixed H that will be useful for the discussion in Secs. 5.4 and 5.5.

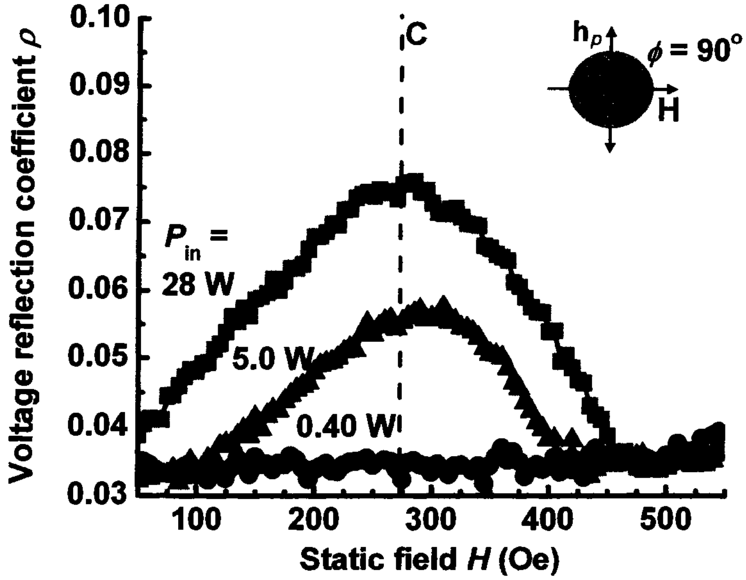

FIG. 5.5. Voltage reflection coefficient ρ vs. H subsidiary absorption profiles for the 104 nm thin film, the in-plane static field configuration, and a microwave frequency of 9.58 GHz. The symbols show data for different P_{in} values, as indicated. The dashed line shows a cut at 280 Oe, line cut C. The H field and the h_p field were in-plane and mutually perpendicular at $\phi = 90^{\circ}$, as shown in the inset.

As above, the changes in the profiles as the input power is increased qualitatively indicate the overall SA nonlinear response. The low power data has very low loss over the range of H values, as the response is on the extreme low field FMR tail. As the power is increased, the profile shows an increase in ρ relative to the low power profile. This is the basic subsidiary absorption response associated with the first order SWI process.

The increase in amplitude occurs in a limited field region, where spin waves are available at one half the microwave pumping frequency. For the thin films and microwave frequencies used here, these effects occur for static fields well below

FMR. It is important to note that for thicker films or higher magnetization materials the available spin wave modes at $\omega_p/2$ can extend to fields in the region of FMR. Again this is a threshold effect and the change in ρ occurs abruptly at some h_{crit} amplitude.

5.4 MICROWAVE CAVITY CALIBRATION

This section develops the procedure to properly calibrate the microwave cavity. Subsection 5.4.1 introduces the obstacles associated with cavity calibration. Subsection 5.4.2 discusses the cavity coupling and a method to determine the upper limit on cavity coupling for cavity perturbation theory to be applicable. Subsection 5.4.3 reviews cavity perturbation theory and gives the working equations for cavity calibration. Subsection 5.4.4 presents the experimental procedure to obtain the cavity parameters. Subsection 5.4.5 discusses the loss dependent cavity calibration that is necessary for proper calibration over the FMR field range.

5.4.1 CAVITY CALIBRATION OBSTACLES

There are two major obstacles that must be overcome to properly determine the coefficient $C = h_p^2 / P_{\text{in}}$ that connects the measured P_{in} value to the h_p field for a microwave cavity. The first is that the standard microwave theory [Green and Kohane (1964)], which provides the relation $C = h_p^2 / P_{\text{in}}$ for the h_p amplitude at the maximum field points in the cavity, requires that the absorption due to the sample be a small perturbation on the microwave fields in the cavity. For fully coupled measurements at FMR this is not necessarily the case. It is, then, necessary to determine the maximum allowable FMR coupling for perturbation theory to be applicable. The coupling is reduced by a decrease in the ϕ angle between the **H** and the $\mathbf{h}_p(t)$ fields. Once the maximum allowable FMR coupling limit is set, the actual calibration coefficient C can be obtained.

The second obstacle that must be addressed is connected to the substantial changes in the cavity frequency and the Q_L parameters over the full FMR field range. These changes make it impossible to obtain accurate h_{crit} values based on a single high H cavity reference measurement. The traditional approach is to bias the cavity at a field far from ferromagnetic resonance and use the standard recipe from Green and Kohane (1964) for a determination of the various cavity parameters. This is inadequate for threshold measurements over the FMR field range. It is important to note that both of these issues apply only to threshold measurements over the FMR field range.

5.4.2 CAVITY COUPLING CONSIDERATIONS

The upper limit on the FMR coupling for a valid calibrated response is determined from data on ρ vs. P_{in} for different ϕ angles. Representative data are used here to demonstrate the effect of cavity loading and to determine an upper limit on the loading of the cavity. It is important to note that the data acquisition method and a full discussion of these data are given in Sec. 5.5 and only a brief introduction is presented here.

As mentioned previously, the changes in the FMR and the low field responses as the P_{in} level is increased are threshold effects and not gradual changes. Recall that the uncalibrated high power FMR profiles in Fig. 5.4 that show the resonance saturation effect and the two vertical A and B line cuts through these profiles. The A cut, at the low power FMR peak position, shows that ρ decreases as the power is increased. The B cut, positioned well off the FMR peak, shows that ρ increases with an increase of power. Then for a fixed H, the P_{in} at which threshold occurs can be extracted from the ρ vs. P_{in} data. The threshold curves that are discussed here are not calibrated.

For comparison purposes the ρ vs. P_{in} data were converted to a reduced loss parameter L_R, according to

$$L_R = \frac{\left(\rho_P - \rho_{\text{ref}}\right)\left(1-\rho_0\right)}{\left(\rho_0 - \rho_{\text{ref}}\right)\left(1-\rho_P\right)} \quad . \tag{5.1}$$

Here, ρ_P is the measured ρ value for the P_{in} value of interest and ρ_0 is the ρ value in the low power limit. Both ρ_P and ρ_0 are obtained at the FMR field. The ρ_{ref} coefficient is the reference ρ value with H set far from the FMR field.

The introduction of a reduced loss parameter L_R for the data comparison for different coupling angles deserves brief comment. At or near FMR, the voltage reflection coefficient ρ is comprised of two parts, an empty cavity part and the component related to the FMR loss. As demonstrated in Fig. 5.3, the component related to FMR loss decreases as the power is increased. A decrease in coupling has a similar effect. As a result, one cannot use ρ as a basis of comparison for different coupling angles.

The standard microwave perturbation theory analysis for a weakly coupled cavity indicates that L_R should correspond to the ratio of the high and low power negative imaginary components of the microwave susceptibility [Green and Kohane (1964)]. In other words, in the small coupling limit that perturbation theory is valid, plots of L_R vs. the effective pumping field should all show the same nonlinear response. Recall that the h_p at the sample position scales with the square root of P_{in} and that only the component of $\mathbf{h}_p(t)$ that is *transverse* to the static field drives the FMR response. For a given angle ϕ between $\mathbf{H}$ and $\mathbf{h}_p(t)$, the *effective* pumping field amplitude scales with $P_{\text{in}}^{1/2}\sin\phi$. Then for all angles below the maximum ϕ the plots of L_R vs. $P_{\text{in}}^{1/2}\sin\phi$ should all show the same response.

Figure 5.6 shows representative data on L_R vs $P_{\text{in}}^{1/2}\sin\phi$ for the 104 nm film and a range of coupling angles that demonstrate the loading effects described above. These specific data are for $H = 830$ Oe, at the FMR line cut A in Fig. 5.4. Data are shown for ϕ values of 90°, 70°, 60°, and 50°, indicated, and input powers from zero to 49 W.

For the two largest ϕ values, 70° and 90°, excessive cavity loading gives a L_R vs. $P_{\text{in}}^{1/2}\sin\phi$ response that depends on the coupling and shows a larger distortion for higher powers. For the two smaller ϕ values, 50° and 60°, the L_R vs. $P_{\text{in}}^{1/2}\sin\phi$ response profiles are identical within the error of the data.

This is an indication that coupling angles at or below 60° or so are sufficient to put the cavity response in the regime where (1) perturbation theory is applicable and (2) a proper calibration between P_{in} and h_p is possible. Calibrated data on L_R vs

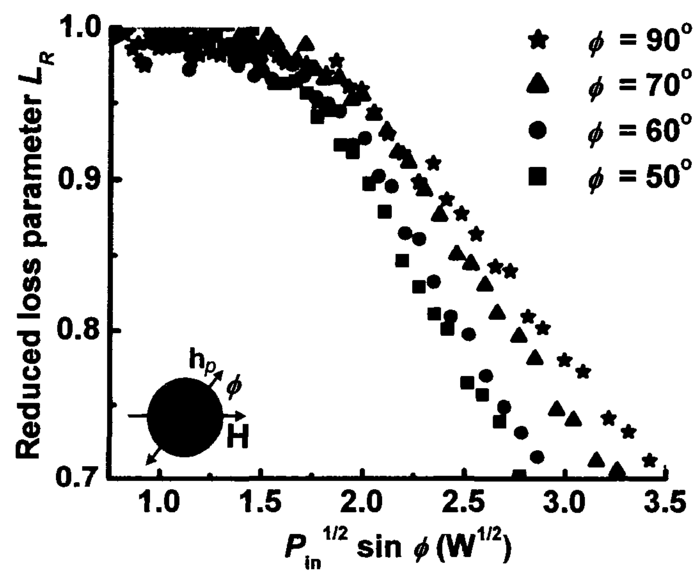

FIG. 5.6. Reduced loss parameter L_R vs. the effective pumping factor $P_{\text{in}}^{1/2}\sin\phi$ for the 104 nm thin film, where the ϕ angles are as shown in the inset. Both fields are in-plane. The data are for $H_{\text{FMR}} = 830$ Oe and a pumping frequency of 9.11 GHz.

$h_p \sin\phi$ in this regime give SWI response profiles that are independent of the coupling angle and give an accurate and reliable determination of the $h_{\rm crit}$ threshold at a given static field. It is also important to note that the change in the cavity Q_L over the full range of the data in Fig. 5.6 for the two *smallest* ϕ values is less than 20%. This is the order of change in coupling that sets an upper limit on the applicability of perturbation theory and a valid microwave field calibration.

5.4.3 CAVITY PERTURBATION THEORY

This subsection provides an overview of cavity perturbation theory and gives working equations for the coefficient that connects the input power to the microwave field amplitude. Cavity perturbation theory is only briefly discussed here, since it has been presented in detail in Green and Kohane (1964) and Nazarov (2002), among others. The microwave theory by Green and Kohane (1964) provides the relation between $P_{\rm in}$ and h_p at the positions of the maximum field amplitude in the cavity. This relation may be written as [Patton and Green (1971)]

$$h_p(\mathrm{Oe}) = \sqrt{\frac{20Q_I(1-\rho_0)^2}{g_m f_{\rm res}(\mathrm{GHz})V_c(\mathrm{mm}^3)}P_{\rm in}(\mathrm{W})} \quad , \tag{5.2}$$

where Q_I is the iris quality factor of the cavity, ρ_0 is the dimensionless voltage reflection coefficient at the resonance frequency of the cavity, g_m is a dimensionless geometrical factor, $f_{\rm res}$ is the resonance frequency of the cavity in GHz, V_c is the cavity volume in mm^3, P_{in} is the power incident on the cavity in W, and h_p is the microwave field amplitude in Oe. The cavity calibration constant C that connects P_{in} to h_p is

$$C(\text{Oe}^2/\text{W}) = \frac{20Q_I(1-\rho_0)^2}{g_m f_{\text{res}}(\text{GHz})V_c(\text{mm}^3)} \quad . \tag{5.3}$$

At this point the cavity quality factors deserve further attention. There are three cavity quality factors. The first is the iris cavity quality factor Q_I. This is determined only by the coupling of the microwaves into the cavity through the iris. It is independent of the sample. The next is the volume quality factor Q_V. This depends on the cavity walls and the sample. The Q_V factor changes as the sample absorption changes. The Q_I and Q_V factors are independent of one another. The Q_L factor is a measure of the total quality of the cavity and is given as $1/Q_L = 1/Q_I + 1/Q_V$.

The g_m parameter in Eq. (5.2) is a geometry factor that depends on the cavity dimensions. It relates the stored energy in the cavity to the h_p at the sample position. The g_m parameter can be calculated from standard waveguide theory [Jackson (1999)], [Waldron (1969)] and is

$$g_m = \frac{\int_{V_c} |h|^2 \, dV}{V_c |h_p|^2} \quad . \tag{5.4}$$

The solutions of interest are for a TE_{102} rectangular cavity and a TE_{011} cylindrical cavity, as shown in Fig. 5.2. The solution for the sample at the bottom of the TE_{102} rectangular cavity is

$$g_m = \frac{1}{4}\left[1+\left(\frac{w}{2h}\right)^2\right] , \qquad (5.5)$$

where w and h are the width and the height of the cavity, respectively and the solution for the TE_{011} cylindrical cavity is

$$g_m = \frac{1}{2}J_0^2(\rho_{11})\left[1+\left(\frac{\pi r}{l\rho_{11}}\right)^2\right] , \qquad (5.6)$$

where J_0 is the zeroth order Bessel function, ρ_{11} is the first zeroth root of the first order Bessel function, r is the cavity radius, and l is the width of the cavity.

The parameters Q_l and ρ_0 are obtained by a measurement of the cavity response ρ vs. f in a small span around f_{res}. Recall that ρ is defined as $\rho = (P_{in} / P_{ref})^{1/2}$ and ρ_0 is the unitless voltage reflection coefficient at f_{res}. The resulting cavity response curve is assumed to correspond to a Lorentzian resonance response and Q_l is calculated from this response through the procedures given in McKinstry and Patton (1989) and Frait and Patton (1980).

5.4.4 MEASUREMENT OF CAVITY PARAMETERS

This subsection develops the procedure to measure the cavity parameters in order to determine the calibration coefficient. Several modifications must be made to the high power FMR system, shown in Fig. 5.1, to measure the cavity parameters. First, a HP 70820A microwave transition analyzer (MTA) is added to the system to control the synthesized sweeper. The synthesized sweeper is connected directly to the input of the waveguide rather than to the TWT. Lastly, the crystal detector is replaced with the MTA input line to measure the reflected signal from the cavity.

The H field is set to the desired value and the MTA sweeps the microwave frequency and measures the cavity response as a function of frequency. A reference response is measured by the replacement of the cavity by a short at the cavity iris position. The reference response is subtracted from the cavity response and the resultant curve is then used to find the f_{res}, Q_l, and C parameters, as mentioned above. In addition to these parameters, the Γ, ρ_0, Q_L, and Q_V parameters are found. The typical empty cavity parameters found for both the rectangular and cylindrical cavities were given in Sec. 5.2. These cavity parameters are input into Eq. (5.3) to obtain the off-resonance cavity calibration values of C=3.54 and 14.5 Oe^2/W for the rectangular and cylindrical cavities, respectively.

When a sample is placed in a microwave cavity, there is additional loss and the Q_L and C parameters change. For low field measurements, the only change to the Q_L factor is from the addition of the sample. The traditional method for cavity calibration at a bias field far from FMR is appropriate and sufficient for these measurements. However, over the FMR field range, the Q_L and $f_{\rm res}$ values change with the susceptibility. The C function, as given above, is written in terms of ρ_0 and Q_I. Although Q_I is constant, the ρ_0 coefficient varies with Q_L and susceptibility. The calibration coefficient C is then a function of the voltage reflection coefficient. The dependence on loss provides a means to properly calibrate the cavity over the full FMR field range.

5.4.5 LOSS DEPENDENT CAVITY CALIBRATION

As mentioned earlier, there are substantial changes in the $f_{\rm res}$ and Q_L parameters over the full FMR profile. In fact, these changes are due to the FMR response and are directly connected to the real and imaginary parts of the susceptibility. The cavity calibration depends on these parameters and it is essential to take these into account for the calibration of data in the FMR field region.

A point-by-point calibration of the cavity was done over the entire FMR profile, typically in 5 – 10 Oe steps, depending on the linewidth. These calibration data were then used to determine the C vs. H response. It was found that these C values, for a given cavity, are actually a *universal function* of the cavity reflection coefficient ρ. This means that a *universal* $C(\rho)$ response function can be used for all of the data for different samples, different coupling angles, and different static fields. This allows for the accumulation of calibrated data by a much simpler means than would otherwise be the case. This is also consistent with the $C = A(1-\rho)^2$ result from perturbation theory, where A is a known function of the cavity mode, cavity volume, and frequency, as seen in Eq. (5.3) [Green and Kohane (1964)].

Figure 5.7 shows representative C vs. ρ data for the 104 nm thick film at 9.11 GHz. The coupling angle was at $\phi = 60^{\circ}$, with both fields in-plane, as shown in the inset. The field ranged from 700 to 960 Oe. Recall that the low power FMR peak is

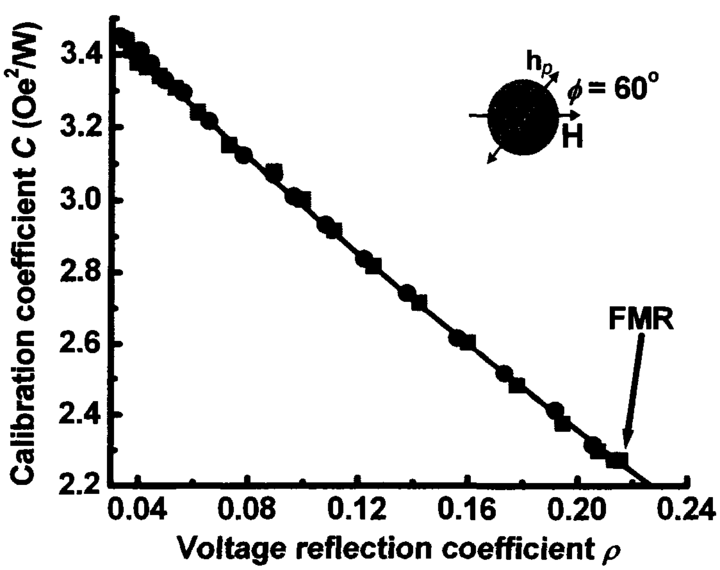

FIG. 5.7. Graph of C vs. ρ for the 104 nm thin film at 9.11 GHz. The inset shows the coupling geometry, with the H field and the h_p field at $\phi = 60°$, as indicated. The data are for a CW microwave input power at about 10 dBm. The green square data points are for fields from 700 Oe to 830 Oe and the blue circle data points are for H values from 825 Oe to 960 Oe. The arrow indicates the open square data point associated with the H_{FMR}. The solid line shows the theoretical response based on $C = A(1-\rho)^2$ with A set to 3.68 Oe^2/W.

at $H = 830$ Oe.

The cavity ρ coefficient ranged from about 0.22 at the FMR point to 0.03 at the high and low field end limits given above. The Q_L change over the range of the data was less than 20% and in line with the criteria established above. In order to emphasize the universal $C(\rho)$ connection, the data in Fig. 5.7 are shown in a C vs. ρ format. For the undercoupled cavity, ρ is a maximum at the indicated FMR field. As one moves away from the FMR peak, either to lower or higher fields, ρ decreases. The blue circles and green squares correspond to fields above and below the FMR point, respectively. The solid line shows a best fit to the data, based on $C = A(1-\rho)^2$, with A taken as a single fitting parameter. The fit shown is for $A = 3.68$ Oe^2/W. The chi-squared parameter for the fit was 0.99928.

Figure 5.7 demonstrates two major points. First, the fact that for fields above resonance and below resonance the data fall on the *same* C vs. ρ response curve provides proof that the universal $C(\rho)$ response function assumption is valid. Second, the fact that the data match the $C = A(1-\rho)^2$ relation provides further support for the thesis that perturbation theory is indeed applicable. The A value for the $C = A(1-\rho)^2$ fit is nominally the same as obtained from perturbation theory. For the nominal Q_I from the cavity calibrations and the f_{res}, along with the volume and mode parameters for the cavity, one obtains a theoretical A value of 3.54 Oe^2/W.

Based on the calibration discussion in this section, two requirements for proper cavity calibration, for resonance saturation, are now established. (1) The $\phi \leq 60°$ decoupling criteria established above can be taken as necessary and sufficient for the application of perturbation theory to cavity calibration. (2) A universal $C(\rho)$ function obtained either empirically or directly from perturbation theory is adequate for the calibration of high as well as low power data. The above procedure was repeated sample-by-sample and for different coupling angles within the range allowed by the 20% Q_L change criterion. In all cases, the same $C(\rho)$ calibration function was obtained.

The calibration recipe given above represents a major improvement over previous work. With the exception of Cox *et al.* (2001), most past FMR saturation measurements have been made for maximum coupling, that is, with $\mathbf{h}_p$ perpendicular to $\mathbf{H}$. From Fig. 5.6, one can see that a large coupling leads to a distortion in the threshold curve. This results in an overestimation of the onset h_{crit} value by as much as 10%. Even with a reduced coupling, however, one must still take the ρ dependence of C into account. Figure 5.7 shows, for example, that the nominal off-resonance C value of 3.54 Oe^2/W is 50% higher than the value at FMR. If this value is used for the P_{in} to h_p calibration, then the apparent microwave field values are about 25% too high. The combination of these considerations gives field calibration errors for the old procedures in excess of 35%.

It is important to mention that for oblique pumping measurements, the only requirement to obtain a proper cavity calibration coefficient is that the H field must be far from the FMR field. Recall that for the samples and frequencies used here, the SA process is on the extreme low field FMR tail. As a result there is no appreciable cavity loading and no change in the cavity parameters over the field range of interest.

5.5 CALIBRATED CRITICAL THRESHOLD FIELD AMPLITUDE DETERMINATION

The change in the FMR profile and absorption profile below the FMR field, in Fig. 5.4 and 5.5, as the P_{in} level is increased is a threshold effect and not a gradual change. The threshold microwave field amplitude, previously defined as h_{crit}, is the subject of this section. More specifically, this section presents and discusses the calibrated ρ vs. $h_p \sin\phi$ responses obtained from the ρ vs. P_{in} measurements at a fixed H field and the extraction of h_{crit} values from these data. Example h_{crit} vs. H butterfly curves and the procedure to measure threshold curves over the full field range are provided.

For threshold curve measurements, the high power system is set up as discussed in Sec. 5.1 and shown in Fig. 5.1. The system calibration, as discussed in Sec. 5.2, and the cavity calibration, as discussed in Sec. 5.4, must be performed before the threshold curves are measured. For the threshold measurement, the user is required to (1) choose the measurement field, (2) set the main attenuator to the value that corresponds to the initial $P_{\rm in}$, (3) choose a main attenuator value that corresponds to the final $P_{\rm in}$, (3) set the reference and reflection arm attenuators to provide adequate protection to the power meter head and voltage detector, (4) determine the proper duty cycle, and (5) determine the C, $f_{\rm res}$, and Q_L parameters. Before the first data point is measured the frequency is swept and the cavity resonance frequency is found from the cavity reflection vs. frequency response. The power is then stepped and ρ is measured as a function of $P_{\rm in}$. All parameters used and the acquired data are saved to a file.

The example calibrated SWI threshold measurements presented here are for resonance saturation and subsidiary absorption responses for the 104 nm thin Permalloy film. The calibration considerations, from the previous section, have been taken into account. Threshold curves that correspond to resonance saturation are discussed first, followed by curves that correspond to subsidiary absorption.

As discussed, the uncalibrated high power FMR profiles in Fig. 5.4 show the basic resonance saturation effect. The A cut, at the low power FMR peak position, shows that the reflection coefficient decreases as the power is increased. The B cut, positioned off the FMR peak, shows that ρ increases with an increase of power. The ρ vs. $P_{\rm in}$ measurements show the threshold effect. Properly calibrated data obtained from these measurements and based on the procedures given in Sec. 5.4 yield quantitative ρ vs. $h_p \sin\phi$ plots that again show the threshold effect.

Figure 5.8, graphs (a) and (b), show calibrated ρ vs. $h_p \sin\phi$ responses that correspond to the A and B field cuts at 830 and 770 Oe from Fig. 5.4. The insets show the $\mathbf{H}-\mathbf{h}_p(t)$ coupling configurations. Recall that only the transverse component of $\mathbf{h}_p(t)$ relative to the $\mathbf{H}$ direction is effective in driving the response for resonance saturation. The straight lines provide guides to the eye for the

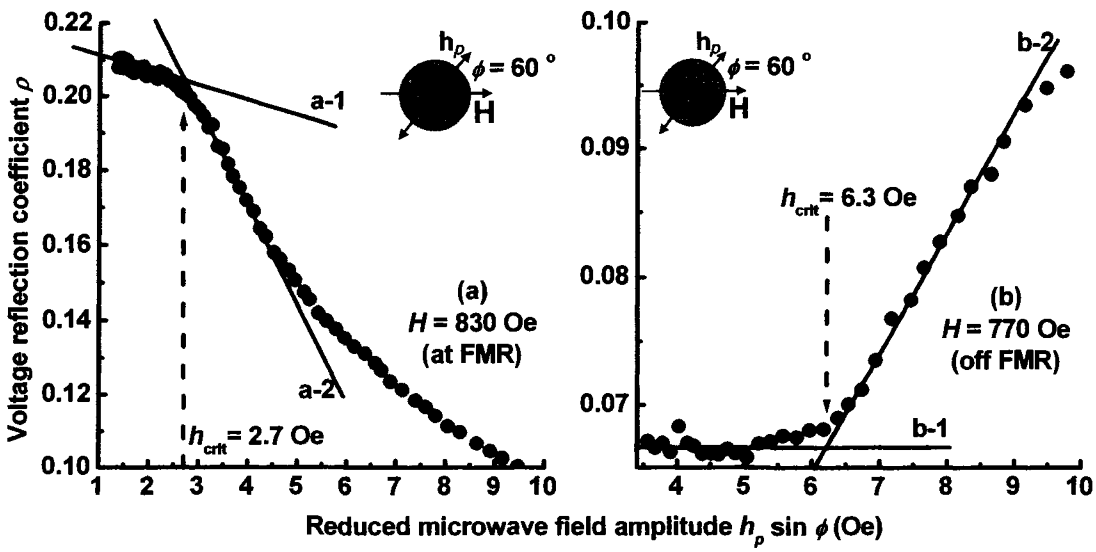

FIG. 5.8. Graph of ρ vs. $h_p \sin\phi$ for the 104 nm thin film at 9.11 GHz. The insets show the coupling geometry, with the in-plane H and h_p fields at $\phi = 60^\circ$ for both sets of data. Graph (a) shows a representative threshold response for $H = 830$ Oe, at the low power FMR peak position. Graph (b) shows the corresponding response for $H = 770$ Oe, on the low field side of the low power FMR profile. The straight lines are guides to the eye. The intersections marked by the vertical dashed lines give estimations of the $h_{\rm crit}$ for the two different cases illustrated here.

estimation of h_{crit} values from the data.

Both graphs demonstrate the threshold nature of the nonlinear response. For the FMR situation in (a), line a-1 shows that ρ is large and a weakly decreasing function of $h_p \sin\phi$ for low power and small h_p, while line a-2 shows a more rapid *decrease* at high power and large h_p. The intersection of the two lines defines the threshold h_{crit} amplitude. The off FMR situation, as in (b), is different. Now, ρ is relatively small and essentially constant below threshold and then shows a rapid *increase* above threshold. In parallel with graph (a), lines b-1 and b-2 show the low and high power trends and the intersection that marks the h_{crit} value. Note also that the threshold response is not particularly sharp in either case.

Figure 5.8 shows three things. First, both data sets show a threshold effect. The corresponding h_{crit} values define a second order SWI threshold, as discussed in Ch. 3. Second, one sees quantitatively different threshold responses on and off resonance. At the low power FMR field position, as in (a), the change in the rate of the decrease in ρ increases at $h_p \approx h_{\text{crit}}$ is due to an initial lock up in the FMR amplitude and a decrease in the effective microwave susceptibility. For the off resonance case, as in (b), the loss starts out small because the static field position is on the tail of the FMR response. As h_p exceeds h_{crit}, the parametric generation of spin waves leads to additional loss and ρ increases.

The third point to note is that the threshold transitions are fairly gradual and do not show the sharp threshold effect of the sort expected from the original nonlinear SWI theory or in defect free single crystal ferrites, for example. Suhl has shown [Suhl (1959)] that two magnon scattering interactions can lead to this type of rounded response. As mentioned previously, Krivosik (2006) extended the two magnon analysis of Suhl in the context of metallic thin films. Krivosik (2006) shows that such processes can give a rounded rather than a sharp transition at threshold as well as the asymmetry in the high power FMR profile of the sort shown in Fig. 5.4.

The results for subsidiary absorption are somewhat similar. Recall the uncalibrated high power subsidiary absorption profiles in Fig. 5.4 and the vertical C line cut through the profiles. The C cut in Fig. 5.5, positioned well off the FMR profile in the region of subsidiary absorption, shows that ρ increases with an increase of power. Properly calibrated data, based on the procedures given in Sec. 5.4, yield quantitative ρ vs. h_p plots that show a threshold effect.

Figure 5.9 shows a calibrated ρ vs. h_p response that corresponds to the C field cut at 280 Oe from Fig. 5.5. The data shown are for a coupling angle of $\phi = 90^{\circ}$, as required for subsidiary absorption measurements. As before, the straight lines provide guides to the eye for the estimation of h_{crit} values from the data.

The graph demonstrates the threshold nature of the nonlinear response for first order SWI processes. It should be noted that the shape of the threshold response is

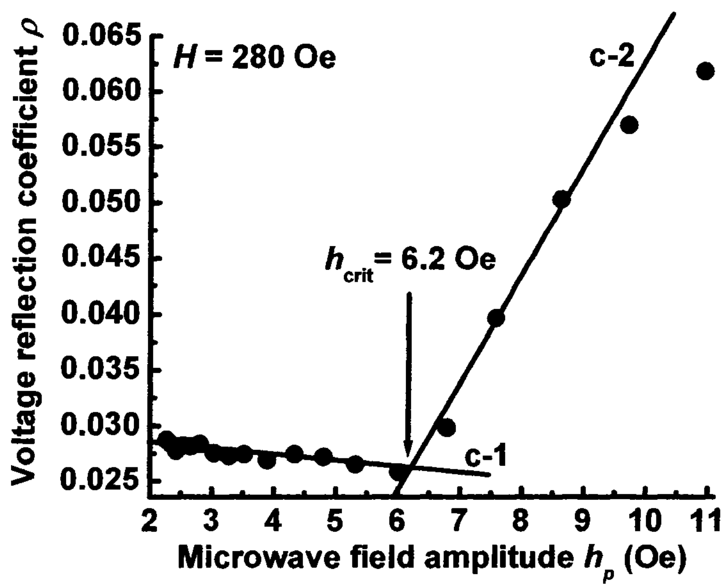

FIG. 5.9. Representative threshold curve of ρ vs. h_p for the 104 nm thin film at 9.58 GHz. The H field is 280 Oe. The in-plane H and h_p fields are mutually perpendicular. The straight lines are guides to the eye. The intersection marked by the vertical dashed line gives an estimation of the h_{crit}.

similar to that in Fig. 5.8(b), although the basis for the spin wave instability is different. The ρ is relatively small and essentially constant below threshold and then shows a rapid *increase* above threshold. In parallel with Fig. 5.8, lines c-1 and c-2 show the low and high power trends, respectively, and the intersection that marks the h_{crit} value.

Figure 5.9 shows the threshold effect and the corresponding h_{crit} values define a first order SWI threshold. The loss starts out small for low P_{in} levels as the spin wave modes reside at thermal levels. As h_p exceeds h_{crit}, the parametric generation of spin waves leads to additional loss and ρ increases.

Threshold curves are measured over a range of static fields to obtain h_{crit} vs. H butterfly curves. The h_{crit} values are extracted and plotted as a function of the static magnetic field. The high power FMR system is fully automated to measure threshold curves over a range of static magnetic fields.

This improvement to the system reduces the maximum time for a full set of threshold measurements by over 75%. The threshold curve measurement procedure described above is repeated over a range of H values. Separate files are saved for each threshold curve. Recall that for resonance saturation the calibration constant C varies with ρ. This is not taken into account by the current program. The user is required to use the ρ vs. P_{in} data, in addition to the calibration $C(\rho)$, as described in Sec. 5.4, to obtain the proper threshold values.

5.6 EXAMPLE BUTTERFLY CURVE DATA AND THEORETICAL FITS

This section presents example butterfly curve results for resonance saturation and subsidiary absorption for the 104 nm thin film. Recall that an overview of the samples was given in Ch. 4. The example resonance saturation data and theoretical fits are discussed first, followed by those for subsidiary absorption. The detailed analyses of the data and fits for the resonance saturation and oblique pumping processes are presented in Ch. 6 and 7, respectively.

5.6.1 EXAMPLE RESONANCE SATURATION DATA AND THEORETICAL FIT

Figure 5.10 shows a representative resonance saturation h_{crit} vs. H butterfly curve for the 104 nm Permalloy thin film at 9.11 GHz. The threshold fields were obtained from data similar to those in Fig. 5.8. The inset in the graph shows the $\mathbf{H}-\mathbf{h}_p$

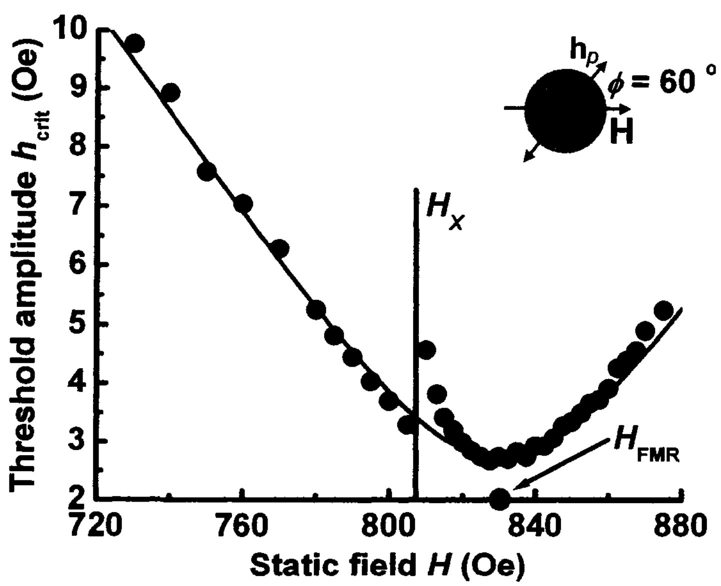

FIG. 5.10. Resonance saturation butterfly curve of h_{crit} vs. H for the 104 nm thin film. The pumping frequency was 9.11 GHz. The inset shows the coupling geometry, with the in-plane H and h_p fields at $\phi = 60°$. The solid circle denotes the FMR field position. The vertical line at H_X marks the jump in the h_{crit} data. The solid curve shows a fit of the second order SWI theory to the data.

configuration where both the $\mathbf{H}$ and $\mathbf{h}_p$ fields are in the plane of the film. The vertical line at $H_X = 810$ Oe marks the threshold crossover point in field between the two types of responses shown in Fig. 5.4. The solid blue dot indicates the FMR field. The solid red curve shows a fit to the data based on the second order SWI theory, as presented in Ch. 3.

The data have several features that deserve attention. These are briefly noted here and are explored in detail in Ch. 6. First, the overall h_{crit} vs. H profile shows a minimum threshold at the FMR field and a symmetric increase in the threshold as the field is increased from low to high. The overall shape of the butterfly curve is tied closely to the low power FMR response. Second, there is a departure from the overall smooth symmetric profile for fields close to the H_X crossover point and a distinct jump in the h_{crit} vs. H response at H_X. This is due to the foldover from two magnon interactions. Finally, in the high H limit, the threshold responses were extremely weak. This is connected with the power independent high field FMR tail response, as seen in the FMR profiles in Fig. 5.4. No reliable h_{crit} determinations were possible for static fields above about 880 Oe or so.

The experimental results shown here are connected with the second order SWI theory, developed in Ch. 3, in order to demonstrate an example h_{crit} data analysis. Recall from Ch. 3 that for thin metal films, the $h_{\text{crit}}^{(2)}$ resonance saturation response is related to the spin wave linewidth ΔH_k by

$$h_{\mathrm{crit}}^{(2)} = \frac{2}{\sin\phi} \min\left[\sqrt{\frac{\omega_p \Delta H_k}{|\gamma| \left|W_k^{(2)}(H,\theta_k)\right|}}\right]_{\omega_k=\omega_p} . \tag{5.7}$$

The solid curve in Fig. 5.10 shows a fit to the data calculated from Eq. (5.7) and the corresponding available spin wave modes. The variable parameter was ΔH_k. The parameters used in the analysis, as listed in Table. 4.1 for the 104 nm Permalloy film, are $4\pi M_{\text{s-eff}} = 11{,}320$ G, $|\gamma|/2\pi = 2.869$ MHz/Oe, and $\Delta H_{\text{FMR}} = 59$ Oe. Additionally, the effective exchange stiffness field taken as $D = 2.1\times10^{-9}$ Oe cm^2/rad^2 [Nisenoff and Terhune (1965)] for Permalloy was used. The calculations were done for a constant spin wave linewidth, $\Delta H_k = 32$ Oe. It is important to note that a constant spin wave linewidth was used rather than the phenomenological Gilbert damping for two reasons. (1) The difference between the fits for a constant spin wave linewidth and Gilbert damping is very small. (2) A constant spin wave linewidth means that the physical spin wave relaxation rate is constant. The spin wave relaxation rate is not constant for the phenomenological Gilbert damping, though. However, it will be shown that the critical spin wave modes are fairly constant over the fields of interest and that the relaxation rate that corresponds to the Gilbert damping is also fairly constant. Figure 5.10 shows that the thin film second order SWI theory, with the spin wave linewidth taken to be constant, gives a good match to the data.

5.6.2 EXAMPLE SUBSIDIARY ABSORPTION DATA AND THEORETICAL FIT

Figure 5.11 shows a representative subsidiary absorption butterfly curve for the 104 nm Permalloy thin film at 9.58 GHz. The threshold fields were obtained from data similar to those in Fig. 5.9. The coupling angle is 90° and both fields were in the plane of the film. The dashed line marks the cutoff field H_{cut} for the spin wave band edge effect. The solid blue, green, and red curves show three fits to the data

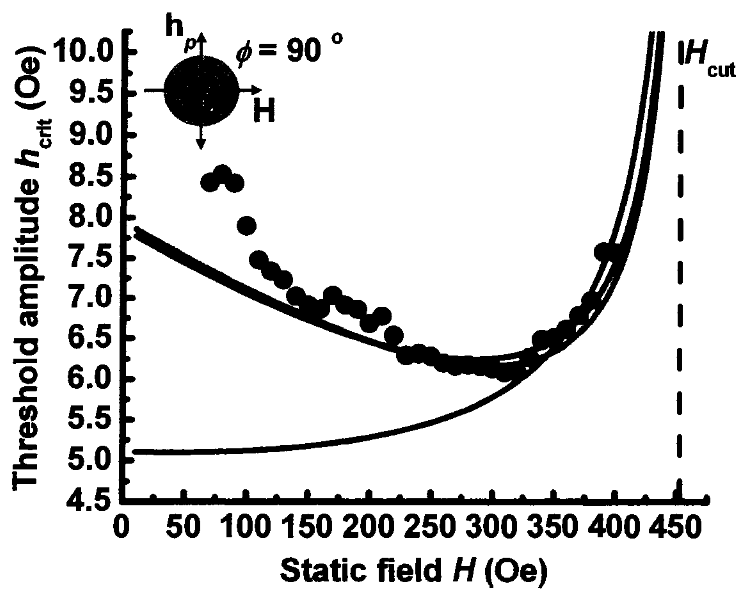

FIG. 5.11. Subsidiary absorption butterfly curve of h_{crit} vs. H for the 104 nm thin film. The pumping frequency was 9.58 GHz. The inset shows the coupling geometry, with the in-plane H and h_p at $\phi = 90^{\circ}$. The dashed vertical line at H_{cut} marks the spin wave band edge. The solid curve blue, green, and red curves show a fits to the data of the thin film first order SWI theory for spin wave linewidth trial functions of $\Delta H_k = 29$ Oe, $\Delta H_k = A + B\sin^2 2\theta_k$ where $A = 25$ Oe and $B = 70$ Oe, and $\Delta H_k = 2\alpha A_k / |\gamma| + B\sin^2 2\theta_k$ where $\alpha = 0.005$ and $B = 70$ Oe, respectively.

based on the first order SWI theory, as presented in Ch. 3, for different spin wave linewidth trial functions.

The data have several features that deserve attention. Chapter 7 will explore these in more detail. First, the overall h_{crit} vs. H profile shows a rather broad minimum and an increase in threshold for H values below the minimum. Second, the threshold increases rather sharply for H higher than the minimum. This high field cutoff is related to the available modes as the field is increased.

These experimental results are connected with the first order SWI theory, given in Ch. 3, in order to demonstrate an example h_{crit} data analysis. Recall that for thin metal films, the $h_{\mathrm{crit}}^{(1)\perp}$ subsidiary absorption response is related to the spin wave linewidth ΔH_k by

$$h_{\mathrm{crit}}^{(1)\perp} = \frac{\omega_p}{\omega_M} \min\left[\frac{\Delta H_k}{\left|W_k^{(1)\perp}(H,\theta_k)\right|}\right]_{\omega_k=\omega_p/2} . \tag{5.8}$$

For the theoretical analysis of subsidiary absorption various trial functions are used for ΔH_k to determine the best fit.

The solid curves in Fig. 5.11 show fits to the data calculated from Eq. (5.8) and the corresponding available spin wave modes with different ΔH_k trial functions. The parameters used in the analysis, as listed in Table. 4.1 for the 104 nm Permalloy film, are $4\pi M_{\mathrm{s\text{-}eff}} = 11{,}320$ G, $|\gamma|/2\pi = 2.869$ MHz/Oe, and $\Delta H_{\mathrm{FMR}} = 59$ Oe. The theoretical subsidiary absorption butterfly curves show a strong dependence on the exchange interaction and the D parameter is varied for each film to provide the best fit. For the 104 nm thin film the value used is $D = 2.38 \times 10^{-9}$ Oe cm^2/rad^2.

The solid blue curve is for a butterfly curve calculation with a constant ΔH_k trial function where $\Delta H_k = 29$ Oe. As discussed in the previous subsection, a constant ΔH_k corresponds to a constant spin wave relaxation rate. The theoretical fit with the constant ΔH_k trial function shows a good fit to the high field data only. This indicates that a constant spin wave relaxation rate is not sufficient to describe the decay of the spin waves generated by the first order SWI process.

Previous subsidiary absorption analysis for a different 104 nm thin Permalloy film given in An *et al.* (2004) used a trial function of the form $\Delta H_k = A + B\sin^2 2\theta_k$ where the $B\sin^2 2\theta_k$ loosely corresponds to a three magnon process. The green curve shows a fit to the data with this trial function. The best fit parameters are $A = 25$ Oe and $B = 70$ Oe. This provided a reasonable fit to the minimum and the high field side of the butterfly curve. The trial function is still not sufficient to describe the low field portion of the data.

Chapter 7 shows that a trial function that includes the phenomenological Gilbert damping rather than a constant term and the $B\sin^2 2\theta_k$ term provides the overall best fits to the oblique pumping data. This trial function has the form $\Delta H_k = 2\alpha A_k / |\gamma| + B\sin^2 2\theta_k$ where α is the Gilbert damping parameter and A_k is given in Eq. (3.23). The red curve in Fig. 5.11 shows a fit to the data for this trial function with $\alpha = 0.005$ and $B = 70$ Oe.

The red curve shows a good fit to the minimum of the data and a reasonable fit to the high field data, but still does not fit the low field data. Although, it is not clear from this figure which trial function best fits the data, the results in Ch. 7 support the use of this trial function. The inability to fit the low H data stems from a break down of the thin film approximation used to derive the working equations for h_{crit} and the spin wave dispersion relation. For a proper fit to the data a full numerical calculation of first order SWI theory for thin films and the spin wave dispersion is necessary. Figure 5.11 shows that the thin film first order SWI theory, with a wave vector dependent ΔH_k, gives reasonable fits to the data except for the low H data.

REFERENCES

[An *et al.* (2004)] S. Y. An, P. Krivosik, M. A. Kramer, H. M. Olson, A. V. Nazarov, and C. E. Patton, J. Appl. Phys. **96**, 1572 (2004).

[Cox et al. (2001)] R. G. Cox, C. E. Patton, M. A. Wittenauer, P. Kabos, and L. Chen, J. Appl. Phys. **89**, 4454 (2001).

[Frait and Patton (1980)] Z. Frait and C. E. Patton, Rev. Sci. Instrum. **51**, 1092 (1980).

[Green and Kohane (1964)] J. J. Green and T. Kohane, SCP Solid State Tech. **49**, (1964).

[Jackson (1999)] J. D. Jackson, *Classical Electrodynamics* (John Wiley and Sons, Inc., 1999).

[Krivosik (2006)] P. Krivosik, Technical Digests, IEEE International Magnetics Conference, San Diego, CA, 8-12 May 2006, (unpublished), Paper No. BA-06.

[McKinstry *et al.* (1985)] K. D. McKinstry, C. E. Patton, and K. M., J. Appl. Phys. **58**, 925 (1985).

[McKinstry and Patton (1989)] K. D. McKinstry and C. E. Patton, Rev. Sci. Instrum. **60**, 439 (1989).

[Nazarov (2002)] A. V. Nazarov, Ph. D. dissertation, Colorado State University, Fort Collins, Colorado (2002).

[Nisenoff and Terhune (1965)] M. Nisenoff and R. W. Terhune, J. Appl. Phys. **36**, 732 (1965).

[Patton and Green (1971)] C. E. Patton and J. J. Green, Rev. Sci. Instrum. **42**, 193 (1971).

[Schloemann *et al.* (1960)] E. Schloemann, J. J. Green, and U. Milano, J. Appl. Phys. **31**, 386S (1960).

[Suhl (1959)] H. Suhl, J. Appl. Phys. **30**, 1961 (1959).

[Waldron (1969)] R. A. Waldron, *Theory of Guided Electromagnetic Waves* (Van Nostrand Reinhold Company, London, 1969).

[Zhang et al. (1987)] Y. T. Zhang, C. E. Patton, G. Srinivasan, G. O. White, C. J. Brower, and C. A. Edmondson, Rev. Sci. Instrum. **58**, 620 (1987).

- 6 -

RESONANCE SATURATION DATA ANALYSIS AND RESULTS

INTRODUCTION

This chapter presents further results on ferromagnetic resonance saturation (RS) and second order spin wave instability (SWI) processes in thin Permalloy films. The main points are (1) FMR profiles as a function of the microwave input power P_{in}, (2) a determination of h_{crit} as a function of H over the entire FMR profile, and (3) an analysis of the h_{crit} vs. H butterfly curve data in terms of the second order SWI theory. The results are for the five Permalloy films of thicknesses of 35, 57, 74, 104, and 123 nm discussed in Ch. 4.

Section 6.1 reviews the qualitative changes in the FMR profiles as P_{in} is increased. Section 6.2 presents the features of the butterfly curves, which includes the overall shape and the effect of the foldover at high power. Section 6.3 considers the theoretical butterfly curve fits to the data and the corresponding critical spin wave modes. Section 6.4 provides a discussion of the spin wave linewidths, damping parameters, and maximum precession angles at FMR that come from the analysis.

6.1 HIGH POWER FERROMAGNETIC RESONANCE PROFILES

This section reviews the results described in Sec. 5.3 and extends the previous discussion to the 35, 57, 74, and 123 nm thin Permalloy films. Figure 6.1 shows example uncalibrated high power FMR response profiles. The graphs show data on ρ vs. H for $\omega_p / 2\pi = 9.11$ GHz. The blue circle and red triangle symbols show the low power data with $P_{in} = 0.44$ W and high power data with $P_{in} = 20$ Oe, respectively. The static and microwave fields were in-plane and mutually

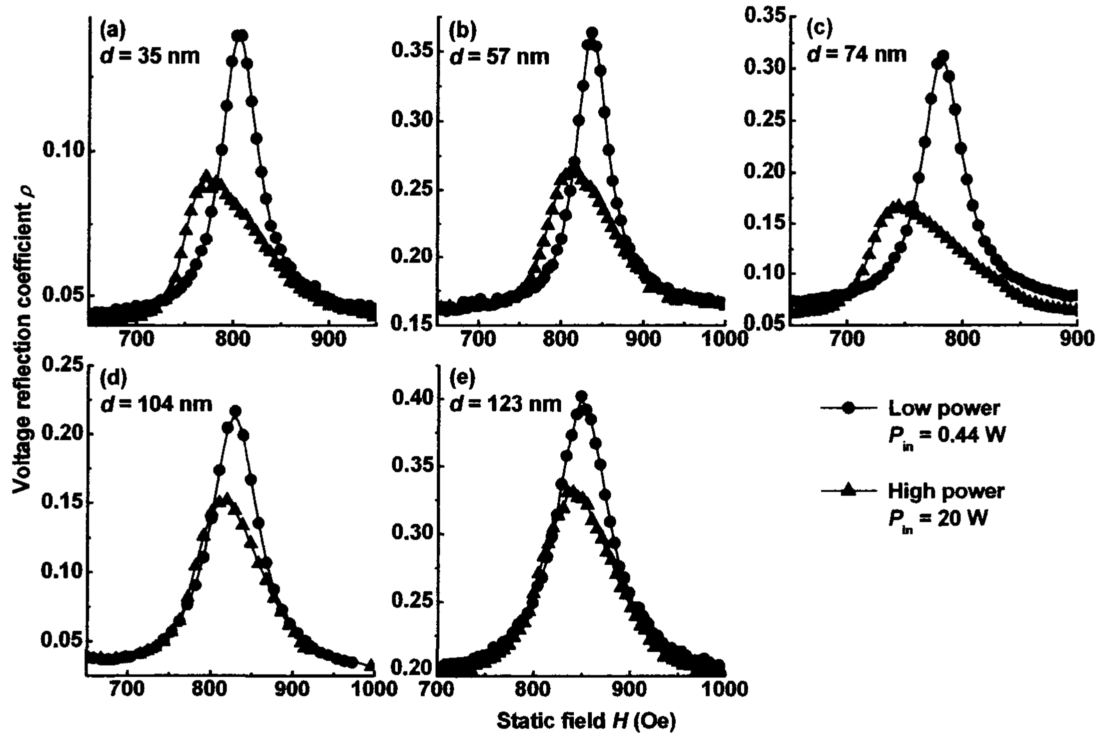

FIG. 6.1. Graphs of ρ vs. H for a f_p of 9.11 GHz. Graphs (a), (b), (c), (d), and (e) are for thin Permalloy films of thicknesses 35, 57, 74, 104, and 123 nm, respectively. The blue symbols show the low power data with P_{in} of 0.44 W. The red symbols show the high power data with P_{in} of 20 W. The H field and h_p field were in-plane and mutually perpendicular at $\phi = 90^{\circ}$.

perpendicular at $\phi = 90^{\circ}$. It is important to emphasize that these FMR curves are obtained at full coupling ($\phi = 90^{\circ}$) and there is no one-to-one correspondence between P_{in} and the microwave field amplitude h_p over a given profile.

There are two qualitative changes in the profiles as the P_{in} levels are increased. These qualitative changes provide an indication of the overall nonlinear response. The first qualitative change is the drop in amplitude and broadening of the FMR profiles. As previously discussed, this is the basic RS response associated with second order SWI processes. The second qualitative change is the shift of the profile to lower fields and the development of a low field shoulder. One can clearly see the development of this asymmetry in graphs (a), (b), and (c). This effect is smaller for graphs (d) and (e) but becomes more pronounced for higher powers. This foldover effect leads to a jump in the butterfly curve and, in combination with the RS response, results in a power independent high field response with no measurable threshold.

6.2 MAIN FEATURES OF THE BUTTERFLY CURVES

Figure 6.2, graphs (a) – (e), show the RS butterfly curve data. The threshold fields were obtained from data similar to those in Fig. 5.8. At the high H limit of the data shown, the threshold responses were extremely weak or nonexistent. This is connected with the power independent high field FMR tail responses in Fig. 6.1. No reliable h_{crit} determinations were possible for H fields above about 840 Oe or so.

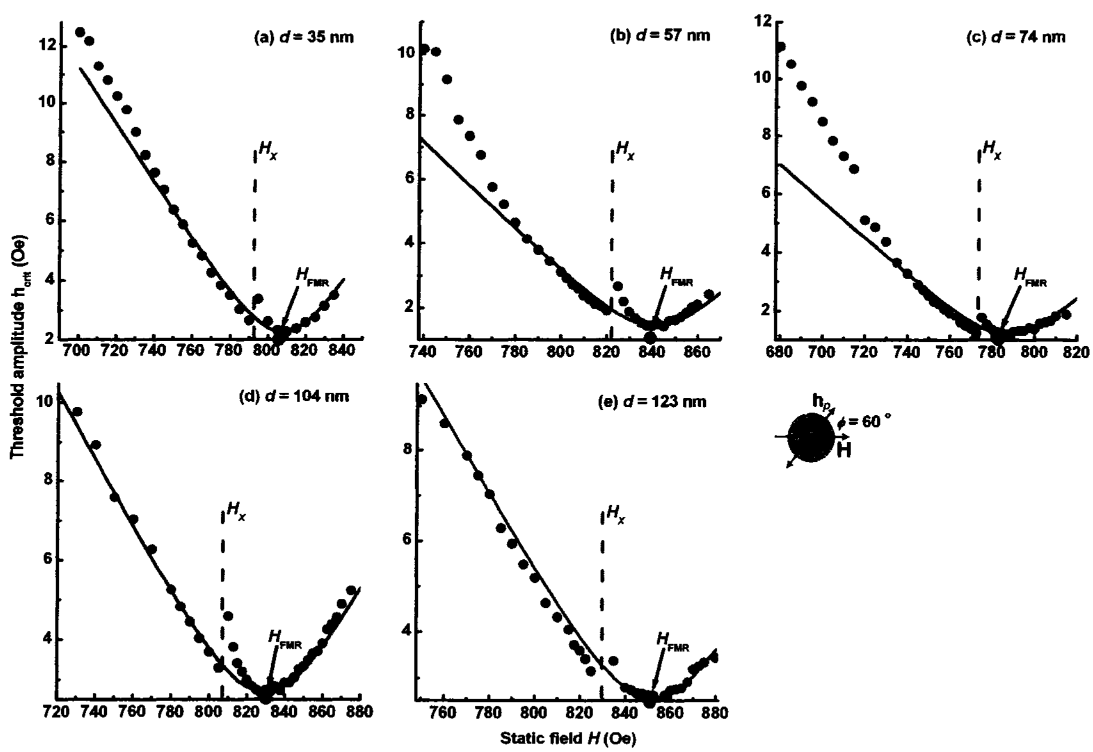

FIG. 6.2. Resonance saturation h_{crit} vs. H butterfly curves for the 35, 57, 74, 104, and 123 nm thin films. The pumping frequency was 9.11 GHz. The inset shows the coupling geometry, with the in-plane H and the in-plane linearly polarized h_p at $\phi = 60^{\circ}$. The solid circle denotes the FMR field position. The vertical line at H_X marks the jump in the h_{crit} data. The solid curve shows a fit of the thin film second order SWI theory to the data.

The green dashed lines mark the threshold crossover point in field H_X between the two types of responses seen on and off resonance, as shown in Fig. 5.8. The blue circle indicates the FMR field points from Table 4.1. The red curve shows fits to the data based on the second order SWI theory, suitably modified for thin films as introduced in Ch. 3. The theoretical fits are discussed in Sec. 6.3.

The data in Fig. 6.2 display two main features. First, the overall butterfly curve profiles show a minimum threshold at the FMR field and a symmetric increase in the threshold as one moves to lower or higher fields. Second, there is a departure, for all curves, from the overall smooth symmetric profiles for fields close to the H_X crossover points and distinct jumps in the h_{crit} vs. H responses at H_X.

6.2.1 OVERALL SHAPE

The overall shape of the butterfly curve profile is tied closely to the low power FMR response. Recall that as energy is pumped into the uniform mode, the uniform precession amplitude increases until the power level exceeds some critical threshold. This critical threshold occurs when the power level exceeds the rate that energy can be lost due to relaxation processes. The energy is then parametrically pumped into certain available spin wave modes as the uniform mode is saturated. The available spin wave modes are defined by the spin wave dispersion curve and the criteria $\omega_k = \omega_p$ for second order processes.

At the FMR field point, where the FMR precession angle is large, the coupling into parametric spin waves is strong and h_{crit} is at a minimum. As the H field is shifted above or below FMR, the precession angle decreases, the coupling also decreases, and a higher h_p is needed to reach the instability threshold. Qualitatively, this means that the butterfly curve profiles are inverted renditions of the low power FMR absorption profiles. This connection is only qualitative because the actual coupling depends on the uniform mode response in a very complicated way. The analytical formulae for the response were provided in Ch. 3. The good theoretical fit to the data in Fig. 6.2 shows that the rigorous analysis gives quantitative agreement.

6.2.2 DEPARTURE FROM SMOOTH CURVE

As noted above, the vertical line at $H = H_X$ marks the crossover point between the on and off FMR threshold responses, as shown in Fig. 5.8. The deviation in the h_{crit} data near H_{FMR} from the smooth red curve and the jump are related to the foldover effect in Fig. 6.1.

Recall that the RS response is a symmetric decrease and broadening of the FMR profile with an increase of P_{in}. In the region of the low power FMR profile the threshold curves have constant microwave loss below threshold and a rapid decrease in loss above threshold as the FMR profile decreases. For static fields above and below the low power FMR profile there is constant loss below threshold and a rapid increase in loss above threshold as the FMR profile broadens. This basic RS response results in a symmetric butterfly curve without a jump.

However, the foldover effect changes the threshold responses and results in deviations of the butterfly curve from the expected smooth symmetric profiles. The critical thresholds for $H < H_X$ are discussed first. As the P_{in} level is increased, the shift of the broadened FMR profile to lower H results in an increase in microwave loss. The increase in loss occurs for P_{in} levels smaller than expected for the situation without foldover. This corresponds to threshold curves that are somewhat rounded, as spin wave are generated before threshold by two magnon processes. The extracted h_{crit} values are also smaller than expected. This is seen in the relatively small deviations of the experimental data near H_X from the theoretical butterfly curves for $H < H_X$, as shown in Fig. 6.2.

The second field regime is for $H_X < H < H_{FMR}$. As P_{in} level is increased, the high power FMR peak shifts to lower fields and the loss is increased in this field region. The threshold curves show a relatively smooth decrease in loss that occurs for P_{in} levels larger than expected from the basic RS response. This results in an increase in the h_{crit} values in the field range $H_X < H < H_{FMR}$. The relatively large deviations of the experimental data from the theoretical butterfly curves, as seen in Fig. 6.2, for $H_X < H < H_{FMR}$ clearly show this effect.

The jumps at H_X are the crossovers between the on resonance and off resonance threshold responses. The relatively small decreases in the h_{crit} values, for $H < H_X$, and the relatively large increases in the h_{crit} values, for $H_X < H < H_{\text{FMR}}$, give the jumps shown in Fig. 6.2.

The data in the high H limit show threshold responses that are extremely weak. This is the result of the combination of the foldover effect and the basic RS response. The RS response increases the high H response to even higher H as the profile is broadened. However the foldover effect shifts the high power high field response to lower fields. The combination of these effects produces high field responses that appear to be independent of P_{in} with no measurable h_{crit}.

6.3 SECOND ORDER SPIN WAVE INSTABILITY THEORY FITS TO THE BUTTERFLY CURVES

Second order SWI theory, suitably modified for thin films, was used to the fit resonance saturation butterfly curves shown in Fig. 6.2. This section shows that second order SWI theory in combination with a constant spin wave relaxation rate η_k gives good fits to the data. The corresponding critical spin wave modes are consistent with bulk spin wave SWI theory.

6.3.1 SECOND ORDER SWI THEORETICAL FITS TO THE DATA

The solid curves in Fig. 6.2 show fits to the data based on the second order SWI theory presented in Ch. 3, as discussed in Ch. 5. The fit is based on the parameters listed in Table 4.1, the effective exchange stiffness field of $D = 2.1\times10^{-9}$ Oe cm^2/rad^2, and the constant spin wave relaxation rates given in Table 6.1. This D value, given by Nisenoff and Terhune (1965), is typical for Permalloy. It is important to note that the D value was initially varied to determine the dependence

TABLE 6.1. Summary of parameters for the fits of the Suhl theory to the resonance saturation butterfly curve data for all samples.

Film thickness d (nm)	Static field at the butterfly curve minimum $H_{\mathrm{BC}}^{\mathrm{min}}$ (Oe)	In-plane static field FMR half power linewidth ΔH_{FMR} (Oe) (from Table I)	Spin wave linewidth (relaxation rate η_k in linewidth units) $\Delta H_k = 2\eta_k / \lvert\gamma\rvert$ (Oe)
35	808	44	35
57	841	41	17
74	787	37	16
104	830	59	32
123	852	56	30

Spin wave relaxation rate $\eta_k \times 10^8$ (1/s)	Equivalent FMR Gilbert damping parameter α_{FMR}	Spin wave Gilbert damping parameter α_k	In-plane precession angle $\vartheta_{\mathrm{FMR}}^{\mathrm{crit}}$ (deg)
3.27	0.0072	0.0046	5.5
1.58	0.0066	0.0026	3.7
1.50	0.0060	0.0025	3.5
2.88	0.0093	0.0050	4.9
2.77	0.0090	0.0048	4.9

of the fit on the exchange interaction. The butterfly curve fits did not show a strong dependence on exchange. Recall that the conversion $\Delta H_k = 2\eta_k / |\gamma|$ is used to cast η_k in convenient linewidth units and that the η_k is related to the Gilbert damping parameter α by $\alpha = (\eta_k / \omega_k)/(\partial\omega_k / \partial|\gamma|H)$. These values are also given in Table 6.1.

Figure 6.2 shows that the thin film second order SWI theory, with the η_k taken to be a constant for each film, agrees well with the experimental results for the $d = 35$, 104 and 123 nm thin films. The data for the other two samples show good fits for fields down to about 60 Oe or so below the butterfly curve minimum, but poor fits for lower fields. For some reason, the measured h_{crit} values in this lower field range for these samples show a more rapid increase than the smooth data trends and corresponding theoretical responses in Fig. 6.2 (a), (d), and (e).

As mentioned, Table 6.1 summarizes the results from the fits for the full ensemble of films. The table lists the measured static fields at the butterfly curve minimum $H_{\text{BC}}^{\text{min}}$, the in-plane ΔH_{FMR} and α_{FMR} values from Table 4.1, and the η_k rates, ΔH_k values, α parameters from the butterfly curve fits, and the in-plane FMR precession angles $\theta_{\text{FMR}}^{\text{crit}}$ at h_{crit} from the butterfly curve fits. The resultant parameters from the butterfly curve fits are discussed in Sec. 6.4.

These RS butterfly curve data and the corresponding fits are only the second such results of record. The first such results by Cox *et al.* (2001), were for in-plane magnetized single crystal Zn-Y-type hexagonal ferrite disks with planar anisotropy. For these samples, the SWI theory with a constant η_k gave only a poor qualitative fit to the data. Good semi-quantitative fits required the introduction of a substantial k dependent component to the spin wave relaxation rate.

6.3.2 CRITICAL SPIN WAVE MODES

The computed $h_{\mathrm{crit}}(H)$ responses shown in Fig. 6.2 have corresponding critical mode k_{crit} and θ_{crit} vs. H profiles. For the full range of static fields shown the critical mode propagation angles were at $\theta_{\mathrm{crit}} = 0^{\circ}$. Interestingly, $\theta_{\mathrm{crit}} = 0^{\circ}$ also comes out of the original SWI theory for bulk isotropic ferrites biased at the FMR field [Suhl (1957)]. The criteria that $\omega_k = \omega_p$ for second order processes, in combination with $\theta_{\mathrm{crit}} = 0^{\circ}$ and the spin wave dispersion equation, given in Ch. 3, completely specifies the k_{crit} modes.

Figure 6.3 shows the k_{crit} vs. H curves that correspond to the fits shown in Fig. 6.2 for all five films, as indicated. The inset indicates the $\theta_{\mathrm{crit}} = 0^{\circ}$ critical mode. The k_{crit} values are in a very small range and decrease almost linearly with an increase in the H field. The decrease of the k_{crit} values is due to the increase in frequency of the $\theta_{\mathrm{crit}} = 0^{\circ}$ branch of the spin wave band with an increase in the H field.

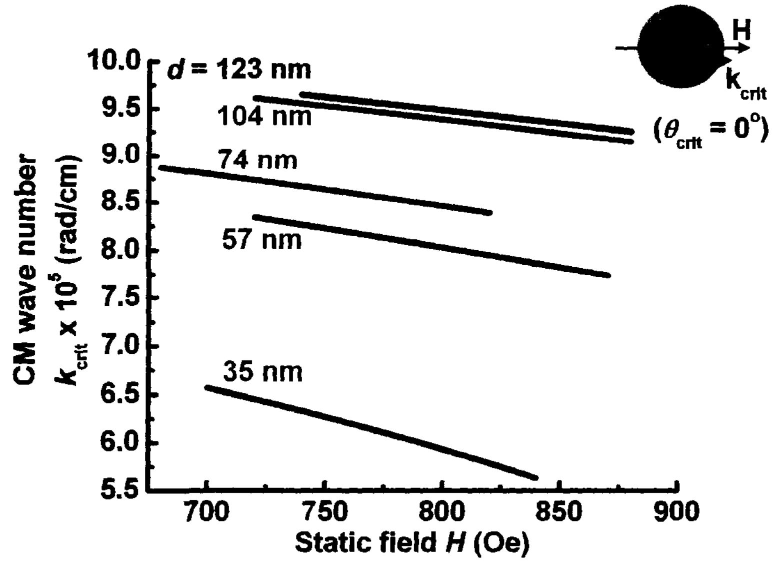

FIG. 6.3. Corresponding k_{crit} vs. H plots for the 35, 74, 57, 104, and 123 nm thin films, as indicated.

Figure 6.3 also shows an overall increase in the k_{crit} values for thicker films. This is the direct result of the change in the $\theta_{\mathrm{crit}} = 0^{\circ}$ spin wave dispersion branch with film thickness. As discussed in Ch. 3, for thinner films the $\theta_{\mathrm{crit}} = 0^{\circ}$ spin wave dispersion branch becomes shallower. The available k values are then smaller and correspondingly the k_{crit} values are lower.

The ability to achieve a good theoretical fit to an experimental butterfly curve for a single η_k value is likely due to the simple fact that the k_{crit} remains essentially constant over the full FMR profile. As noted above, the k_{crit} values are all limited to a very small range while the critical mode remains at $\theta_{\mathrm{crit}} = 0^{\circ}$. The resultant shape of the theoretical butterfly curve is then determined only by the uniform mode susceptibility and the corresponding field dependent coupling factor $W_k^{(2)}(H,k,\theta_k)$, as given in Ch. 3. In contrast, the changes in the critical mode k_{crit} and θ_{crit} values over the wide range of fields associated with the subsidiary absorption butterfly curves in An *et al.* (2004) are substantial and the resultant fits to the SA butterfly curves were k dependent. Figure 6 in An *et al.* (2004) shows, in particular that the k_{crit} and θ_{crit} values range from about $1.5\times10^5 - 3.0\times10^5$ rad/cm and $0-17°$, respectively.

6.4 CONCLUSIONS FROM THE RESONANCE SATURATION DATA ANALYSIS

This section discusses the main points from the resonance saturation threshold curve and butterfly curve analyses. First, the use of a constant η_k for the fits is significant in that the associated spin wave relaxation time is a constant for a given butterfly curve and are very small and in the range 3.06 – 6.67 ns. Second, the $H_{\text{BC}}^{\text{min}}$ values in Table 6.1 and the H_{FMR} values in Table 4.1 agree with one another as expected. The next three points require further attention and are presented in separate subsections. Subsection 6.4.1 discusses the effect of two magnon scattering on the threshold responses and the corresponding butterfly curves. Subsection 6.4.2 discusses the Gilbert damping parameters α which are lower than α_{FMR} by a factor of two or more and are consistent with values expected for magnon-electron relaxation. The final subsection discusses the small FMR precession angle just at the threshold field.

6.4.1 TWO MAGNON SCATTERING

Two magnon scattering effects are expected to affect the extrapolated h_{crit} values of the sort shown in Fig. 5.8 to some degree. It was already noted in connection with Fig. 5.8 that the change from the expected abrupt transition at threshold to a rounded response is a two magnon effect. This introduces a certain level of ambiguity in any determination of a specific h_{crit} value. Any corresponding effect on h_{crit} will also modify the fitted α.

For a complete threshold analysis that includes two magnon effects, it is necessary to include not only the nonlinear interactions between the uniform mode and spin wave modes but also the interactions between the parametric spin waves. These additional terms complicate the theory greatly. Zakharov and Lvov (1973) and Cherepanov (1992), among others, have calculated the increase in threshold due to two magnon effects for first order SWI processes, but calculations have not been performed for second order processes. Apart from a recent conference presentation, [Krivosik (2006)] on the effect of two magnon scattering on the high power susceptibility as a function of field, there has been no detailed analysis of two magnon effects on second order RS instability processes. Such work is currently in progress.

6.4.2 GILBERT DAMPING PARAMETER

The Gilbert damping parameter associated with ferromagnetic resonance, α_{FMR}, is generally taken as the standard measure of the FMR loss. As such, the corresponding α parameter calculated from the ΔH_k values can provide a useful basis for comparison. First, one can see that the spin wave Gilbert damping parameter α values from the butterfly curve fits are lower, sometimes by a factor of two or more, than the corresponding FMR Gilbert damping parameter α_{FMR} values. Note that the α_{FMR} values in Table 6.1 are based solely on the measured linewidths by the $\Delta H_{\mathrm{FMR}} = 2\alpha_{\mathrm{FMR}}\omega_p / |\gamma|$ connection. These α_{FMR} values likely contain the effects of inhomogeneity broadening and two magnon scattering as well as the intrinsic magnon-electron scattering losses normally ascribed to the α parameter [Kalarickal *et al.* (2006)], [Kambersky and Patton (1975)].

On the other hand, the generally lower α values are the result of the fact that the SWI derives from the renormalized modes with the lowest threshold. Renormalization can reduce, and in some cases eliminate, the broadening effects due to inhomogeneities, for example. It is important to note that this does not mean that there is no influence on the h_{crit} values from two magnon scattering and the affect of this on α is not clear. However, the generally lower α values listed in the second to last column of Table 6.1 are in the 0.002-0.005 range nominally associated with intrinsic magnon-electron processes only [Meckenstock *et al.* (1995)], [Frait and Fraitova (1980)], [Meckenstock *et al.* (2004)].

6.4.3 MAGNETIZATION LOCK UP ANGLE

The in-plane FMR precession angle at threshold $\vartheta_{\rm FMR}^{\rm crit}$ is also a useful measure of the instability response. The initial effect as the microwave power exceeds the SWI threshold is a lock-up in the uniform mode precession cone at $\vartheta_{\rm FMR}^{\rm crit}$, as energy is pumped into spin waves. This angle, therefore, is an important parameter in SWI processes.

The last column in Table 6.1 shows the calculated $\vartheta_{\rm FMR}^{\rm crit}$ angle. This angle is generally in the range of a few degrees. As one moves above the $h_{\rm crit}$ field, the lock up gradually relaxes, but there is a sizeable increase in loss, well above the levels indicated by the ΔH_k and α parameters discussed above [Gerrits *et al.* (2007)].

Large angle precession dynamics is an important element in many magnetic sensor and information storage applications, among others. Dobin and Victora (2004) describe one way to adapt SWI theory to large angle switching dynamics. The present lock up angle determinations provide a measure of the inherent limitations in a simple damped equation of motion analysis of large angle switching processes and the switching angle limits for the validity of such analyses.

REFERENCES

[An *et al.* (2004)] S. Y. An, P. Krivosik, M. A. Kramer, H. M. Olson, A. V. Nazarov, and C. E. Patton, J. Appl. Phys. **96**, 1572 (2004).

[Cherepanov (1992)] V. B. Cherepanov, Phys. Rev. B **45**, 12397 (1992).

[Cox *et al.* (2001)] R. G. Cox, C. E. Patton, M. A. Wittenauer, P. Kabos, and L. Chen, J. Appl. Phys. **89**, 4454 (2001).

[Dobin and Victora (2004)] A. Y. Dobin and R. H. Victora, J. Appl. Phys. **95**, 7139 (2004).

[Frait and Fraitova (1980)] Z. Frait and D. Fraitova, J. Magn. Magn. Mater. **15**, 1081 (1980).

[Gerrits *et al.* (2007)] T. Gerrits, P. Krivosik, M. L. Schneider, C. E. Patton, and T. J. Silva, Phys. Rev. Lett. **98**, 207602 (2007).

[Kalarickal *et al.* (2006)] S. S. Kalarickal, P. Krivosik, W. M., C. E. Patton, M. L. Schneider, P. Kabos, T. J. Silva, and J. P. Nibargar, J. Appl. Phys. **99**, 093909 (2006).

[Kambersky and Patton (1975)] V. Kambersky and C. E. Patton, Phys. Rev. B **11**, 2668 (1975).

[Krivosik (2006)] P. Krivosik, Technical Digests, IEEE International Magnetics Conference, San Diego, CA, 8-12 May 2006, (unpublished), Paper No. BA-06.

[Meckenstock *et al.* (1995)] R. Meckenstock, O. v. Geisau, J. Pelzl, and J. A. Wolf, J. Appl. Phys. **77**, 6439 (1995).

[Meckenstock *et al.* (2004)] R. Meckenstock, D. Spoddig, Z. Frait, V. Kambersky, and J. Pelzl, J. Magn. Magn. Mater. **272**, 1203 (2004).

[Nisenoff and Terhune (1965)] M. Nisenoff and R. W. Terhune, J. Appl. Phys. **36**, 732 (1965).

[Suhl (1957)] H. Suhl, J. Phys. Chem. Solids **1**, 209 (1957).

[Zakharov and Lvov (1973)] V. Zakharov and V. S. Lvov, Sov. Phys. Solid State **14**, 2513 (1973).

- 7 -

OBLIQUE PUMPING DATA ANALYSIS AND RESULTS

INTRODUCTION

This chapter provides results on oblique pumping (OP) and first order spin wave instability (SWI) processes in thin Permalloy films. The main results are (1) absorption profiles as a function of P_{in}, (2) a determination of h_{crit} as a function of H over the low H region, and (3) an analysis of the h_{crit} vs. H butterfly curve data in terms of the first order SWI theory. The threshold results are for two Permalloy films of thicknesses 104 and 123 nm at a frequency of 9.58 GHz. The materials and the experimental methods for data acquisition were presented in Ch. 4 and 5, respectively.

Section 7.1 provides a review of the qualitative changes in the absorption profiles as P_{in} is increased. The absorption curve results are for a range of $h_p - H - \phi$ coupling configurations. Section 7.2 presents the experimental butterfly curve data on oblique pumping. The overall shape of the butterfly curves and the dependence of h_{crit} on the ϕ angle are discussed. Section 7.3 considers the theoretical butterfly curve fits to the data along with a discussion of the spin wave linewidths and damping parameters, the critical spin wave modes, and the deviation of the theoretical fit from the data at low H fields.

7.1 HIGH POWER ABSORPTION PROFILES

This section presents the qualitative high power absorption profiles for the 74, 104, and 123 nm thin Permalloy films. The absorption profiles for the 104 nm film include the field regions for first and second order SWI processes. The FMR field region is included to provide a reference of comparison for the low field phenomena. The profiles for the 74 and 123 nm films are for the low field range only. The absorption profiles for the 104 and 123 nm films are for a range of coupling configurations between 90° and 0°. This demonstrates the coupling angle ϕ dependence of the oblique pumping process. However, only the profile for the SA configuration is shown for the 74 nm film. No oblique pumping response was observed.

Figures 7.1, 7.2, and 7.3 show example uncalibrated ρ vs. H data for the 104, 123, and 74 nm thin Permalloy films, respectively, and for a range of coupling angles. As discussed in Ch. 2, the changes in the low field region as the P_{in} level is increased qualitatively show the basic oblique pumping response. However, this response also depends on the ϕ angle. The changes in the oblique pumping response as a function of angle provides a qualitative means to compare the subsidiary absorption and parallel pumping responses. The quantitative results are found from threshold measurements and are discussed in Sec. 7.2. As mentioned, the 74 nm film only shows a response for $\phi = 90^{\circ}$ which is very weak and profiles for this sample are discussed last. An overview of the film properties was provided in Ch. 4.

Figure 7.1 shows OP absorption profiles for the 104 nm film and for $\phi = 90$, 70,

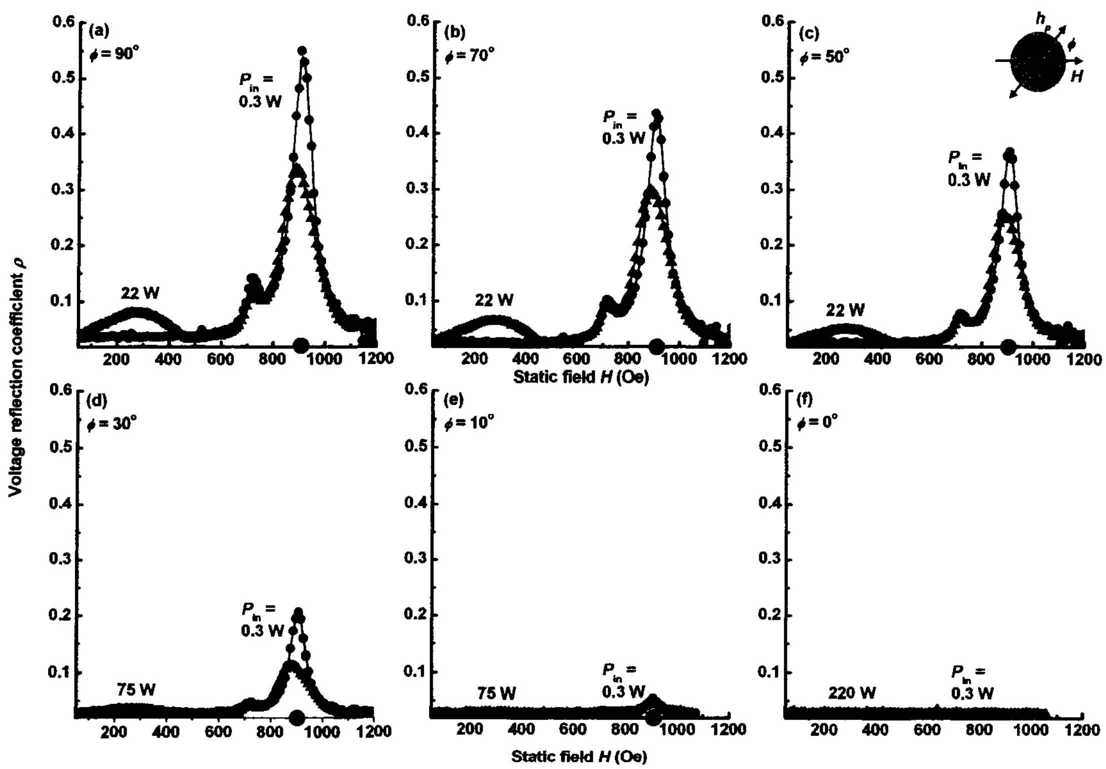

FIG. 7.1. Graphs of ρ vs. H for the 104 nm thin film and a microwave frequency of 9.58 GHz. The H and h_p fields were in-plane and at the ϕ angles indicated. The solid circle data are for low P_{in} and the open circle data are for high P_{in} values, as indicated. The solid points at 910 Oe indicate the H_{FMR} field point. The peaks at high and low field show the resonance saturation and oblique pumping effects, respectively.

50, 30, 10, and 0°, as indicated. The static and microwave fields were in-plane. The blue circle data are for low power and the red triangle data are for high power, as indicated. The curves are guides to the eye. The solid points indicate the FMR peak H_{res} at 910 Oe for each of the graphs. The H_{FMR} value is not the same as given in Table 4.1, since the microwave frequency is 9.58 GHz rather than 9.11 GHz. The high field peaks show the RS effect and the low field peaks show the OP effect. Recall that the measurements are extended to high field to provide a reference for comparison with the low field OP phenomenon.

As noted, the low power FMR peaks in Fig. 7.1 are at 910 Oe. The qualitative changes in the RS profiles, as the power is increased, provide an indication of the overall nonlinear response at FMR, as was discussed in Chapters 5 and 6.

The qualitative changes in the profiles at low field as P_{in} is increased provide an indication of the overall nonlinear OP response associated with first order SWI processes. Notice that the OP response depends on the ϕ angle and there is no response observed in graphs (e) or (f). The low P_{in} data for H below about 450 Oe show very low loss associated with the tail of the FMR response. As the power is increased, there is an increase in loss in this low H region in graphs (a) – (d). This increase in loss is the basic OP response. The OP responses are somewhat broad and lower in amplitude than the RS peak.

Graphs (a) – (c) show a decrease in loss for a fixed P_{in} with a decrease in ϕ. For an angle between 30° and 10° the OP response is no longer visible even for much

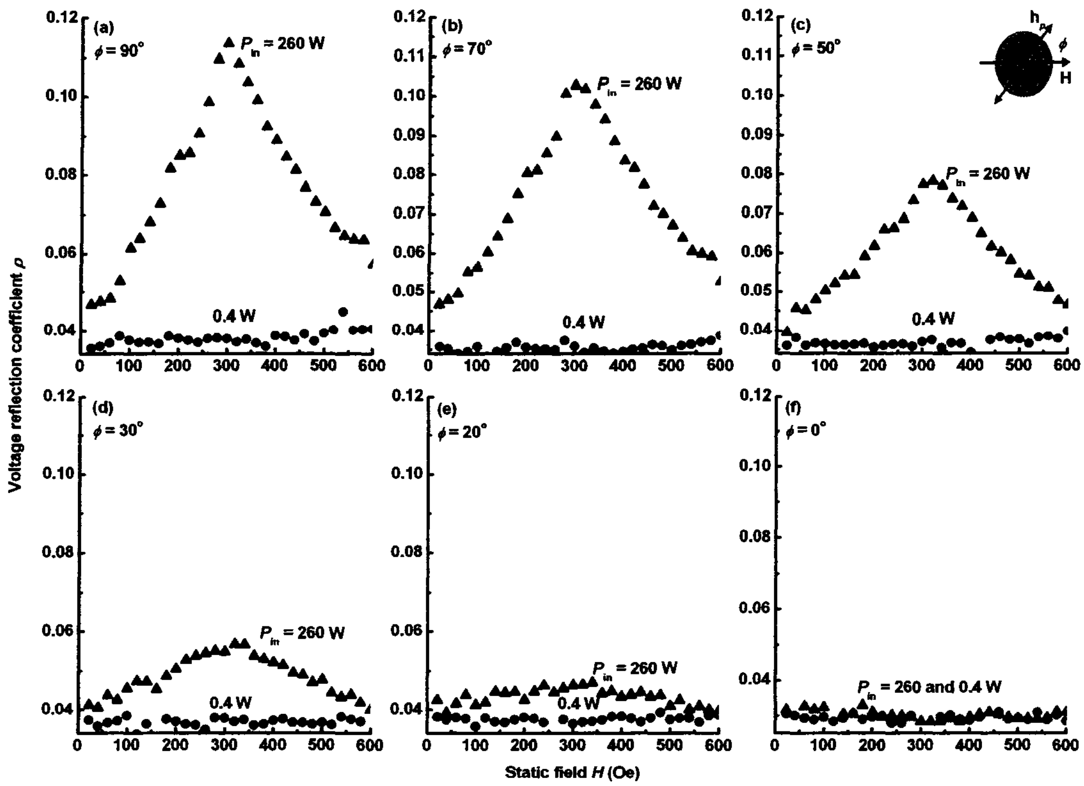

FIG. 7.2. Graphs of ρ vs. H for the 123 nm thin film and a microwave frequency of 9.58 GHz. The H and h_p fields were in-plane and at the ϕ angles indicated. The blue circle data are for low $P_{\text{in}} = 0.4$ W and the red triangle circle data are for high $P_{\text{in}} = 260$ W.

larger input powers and there is no observable OP response for ϕ=0°. The decrease in the OP amplitude for smaller coupling angles is related to the weak coupling of energy from the h_p into the spin wave modes.

Figure 7.2 shows example uncalibrated ρ vs. H data for the 123 nm film and for $\phi = 90$, 70, 50, 30, 20, and 0°, as indicated. The static and microwave fields were in-plane the film plane. The blue circle and red triangle data are for $P_{\text{in}} = 0.4$ and 260 W, respectively. Unlike Fig. 7.1, only the low field OP response region is shown.

Again the qualitative changes, as the P_{in} level is increased and the ϕ angle is decreased, provide an indication of the nonlinear OP response. Graphs (a) – (e) show an increase in loss for fields below about 600 Oe for high P_{in} levels. Figure 7.2 shows the same decrease in the amplitude of the response as the ϕ angle is decreased for a fixed P_{in} level, as Fig. 7.1 graphs (a) – (c). Notice that the response is still visible at $\phi = 20^{\circ}$, where as for the 104 nm film the OP response is barely visible at $\phi = 30^{\circ}$ even for powers as high as 260 W. As before no OP response was observed for $\phi = 0^{\circ}$.

Figure 7.3 shows ρ vs. H data for the 74 nm film at $\phi = 90^{\circ}$, as indicated. The static and microwave fields were in-plane. The blue circle, green triangle, and red

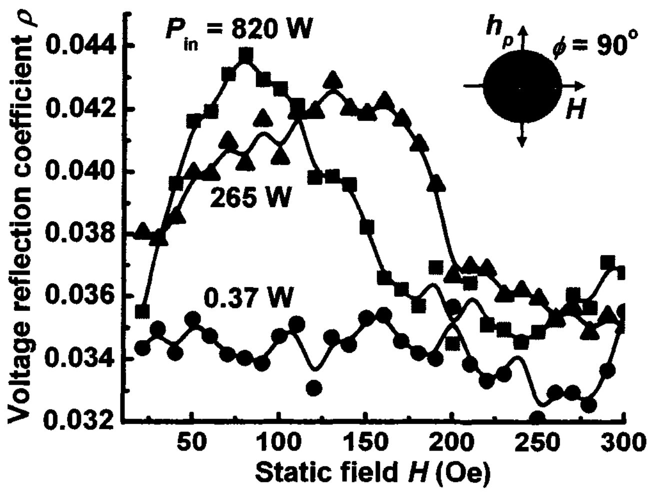

FIG. 7.3. Graphs of ρ vs. H for the 74 nm thin film and a microwave frequency of 9.58 GHz. The **H** and $\mathbf{h}_p$ fields were in-plane and at $\phi = 90^{\circ}$, as indicated. The blue solid circle data is for the low P_{in} of 0.37 W, the green triangle data is for the high P_{in} of 265 W and the red square data is for the very high P_{in} of 820 W.

square data are for $P_{in} = 0.37$, 265, and 820 W, respectively. The curves are guides to the eye. For the 74 nm film the field region of the response is much narrower than for the 104 and 123 nm films. This is again due to the thickness dependence of the spin wave dispersion relation.

The data evidence the typical subsidiary absorption response for H field below about 200 Oe. The first order SWI response is very weak for such a thin film and is almost lost within the noise. Even for very high P_{in} levels the loss is very small and no threshold response is measurable. No data are shown for angles other than $\phi = 90^{\circ}$, as there was no measurable change in loss.

The oblique pumping response is dependent on the film thickness. For the 123, 104, and 74 nm films the response extends up to maximum fields of around $H = 600$, 450, and 200 Oe, respectively. For thinner films the high field edge of the profile is lower. The high field edge of the profile is corresponds to the cutoff field H_{cut}. As discussed in Ch. 3, there are no available spin wave modes for fields above H_{cut} and no SWI response. The H_{cut} field depends on the $\omega_k = \omega_p / 2$ criteria and the thickness dependent spin wave dispersion. The spin wave band edge effect and thickness dependence found here mirrors the results of An *et al.* (2004) for subsidiary absorption only.

7.2 MAIN FEATURES OF THE BUTTERFLY CURVES

This section presents the h_{crit} vs. H oblique pumping butterfly curve data for the 104 and 123 nm thin Permalloy films. Two major features of the data are discussed. The first is the overall shape of the butterfly curve that is tied closely to the nature of the spin wave dispersion curves for thin films. The second feature is the dependence of the thresholds on the coupling angle. Energy is coupled from the perpendicular and parallel components of the microwave pumping field indirectly and directly, respectively, into the available spin wave modes. The butterfly curves, scaled by a factor of $\sin\phi$ for the 104 nm film, show that the parallel or direct coupling serves to increase the overall coupling by a small but significant amount.

Figure 7.4 shows h_{crit} vs. H butterfly curves for the 104 and 123 nm films. The threshold fields were obtained from data similar to those in Fig. 5.9. Graphs (a) and (b) show butterfly curves for coupling angles $\phi = 90$, 80, 70, and 60° and $\phi = 90$, 50, 40, 30, and 25°, respectively, for the 104 nm film. Graphs (c) and (d) show butterfly curves for coupling angles $\phi = 90$, 80, 70, and 60° and $\phi = 90$, 50, 40, 30, and 20°, respectively, for the 123 nm film. The static and microwave fields were in-plane at the indicated coupling configurations. The vertical dashed lines mark the computed half frequency spin wave cutoff field values H_{cut} of 460 and 560 Oe for the 104 and 123 nm films, respectively.

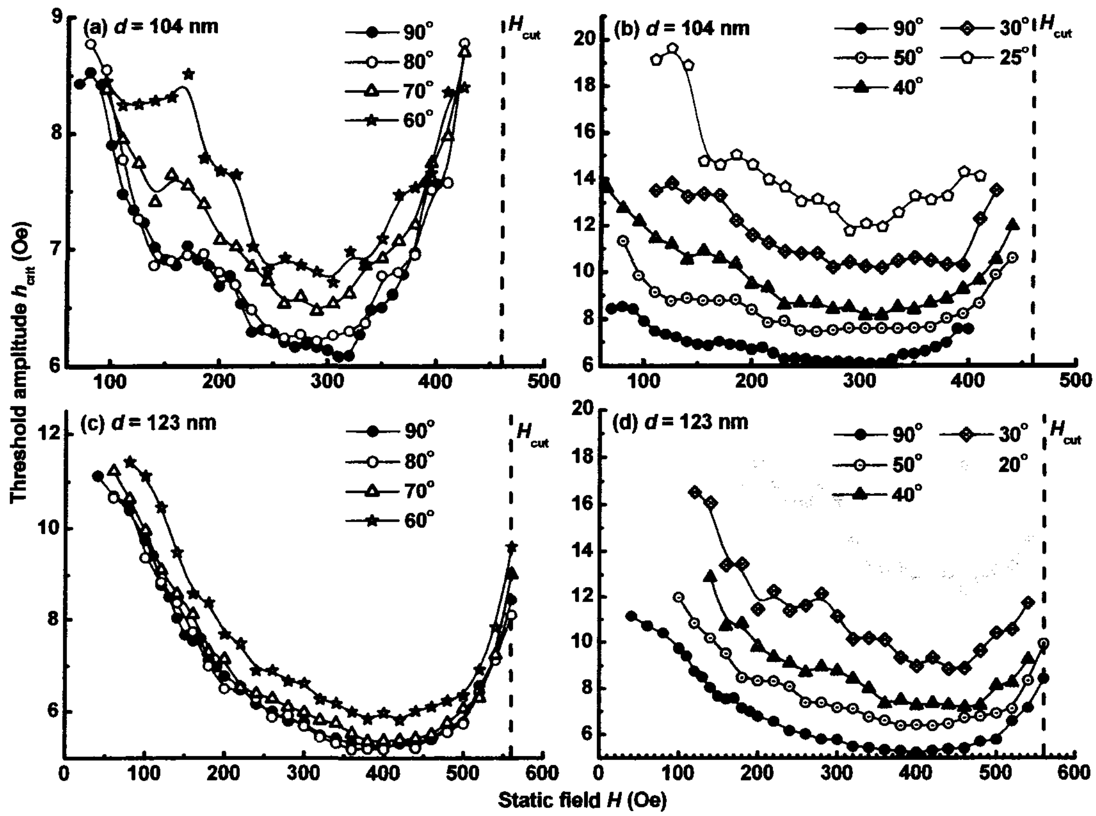

FIG. 7.4. Oblique pumping butterfly curves of h_{crit} vs. H for the 104 and 123 nm thin films, as indicated. The microwave pumping frequency was 9.58 GHz. The H and h_p fields were in-plane and at the ϕ angles indicated. The vertical dashed lines mark values of the computed H_{cut} at 460 and 560 Oe.

7.2.1 OVERALL SHAPE

The minimums of the butterfly curves in Fig. 7.4 are not sharp but rather occur over a broad field range. As one moves to the fields above the minimum, the threshold values increase somewhat faster than below the minimum. As noted above, these h_{crit} values appear to diverge at some high field cutoff H_{cut} and show a band edge effect.

As discussed in Sec. 7.1, the OP responses differ with film thickness. For the 123 nm film the butterfly curves occur over a larger range of static fields and the H_{cut} field is at a larger field value compared with the 104 nm film curves. The sharp increase in h_{crit} values near the H_{cut} field produces difficulties in the extraction of the thresholds closer to the cutoff field. It is notable that the high field edge of the OP profiles in Fig. 7.1 and 7.2 correspond well to the calculated H_{cut} of 460 Oe and 560 Oe values for the 104 and 123 nm thin films, respectively.

The increase in h_{crit} values for H values below the minimums of the butterfly curves is again connected to the available spin wave modes. The theoretical analysis of the data, presented below, shows that the zeroth order thin film approximation [Harte (1968)] is not applicable for these low fields. A full numerical calculation is required to explain the data in this low field region.

The butterfly curves in Fig. 7.4 are notably different from those for bulk ferrites. There are three major differences. First, for both polycrystalline and single crystal ferrites there is a shift of the minimum of the butterfly curves to lower H fields as the ϕ angle is decreased [Patton (1970)]. Figure 7.4 clearly shows that the minimums of the butterfly curves for both the 104 and 123 nm Permalloy films remain at their respective field values for all ϕ angles. Second, in polycrystalline ferrites there is only a slight increase in the h_{crit} values as the ϕ angle is decreased [Patton (1970); Green *et al.* (1969)], and for single crystal ferrites there is a decrease in the h_{crit} values as the ϕ angle is decreased [Patton (1970)]. Figure 7.4 shows a substantial increase in the h_{crit} values as the ϕ angle is decreased. The third difference is that for both the polycrystalline and single crystal ferrites the shape of the butterfly curve changes as ϕ is decreased [Patton (1970); Liu and Patton (1982); Wiese *et al.* (1995)]. The butterfly curve results for the Permalloy films are all similar in shape.

7.2.2 THRESHOLD AS A FUNCTION OF COUPLING ANGLE

The butterfly curves in Fig. 7.4 show an increase in the h_{crit} values with a decrease in the ϕ angle. This effect is connected to the coupling between the microwave pumping field and the available spin wave modes. The component of $\mathbf{h}_p$ that is transverse to $\mathbf{H}$ couples energy indirectly into the available spin wave modes via the uniform mode. The component of $\mathbf{h}_p$ that is parallel to $\mathbf{H}$ couples energy directly into the available spin wave modes. As the ϕ angle is decreased from $\phi = 90^\circ$ to 0° the contribution of energy from the transverse coupling process decreases and the contribution from the parallel coupling process increases. For small ϕ angles, the energy coupled into the spin wave modes is small and larger P_{in} levels are required to reach threshold. At $\phi = 0^\circ$ there is no observable increase in loss, as shown in Fig. 7.1 and 7.2. This *suggests* that there is no dipole-dipole interaction to couple energy into the spin wave modes and as a result, no parallel pumping process.

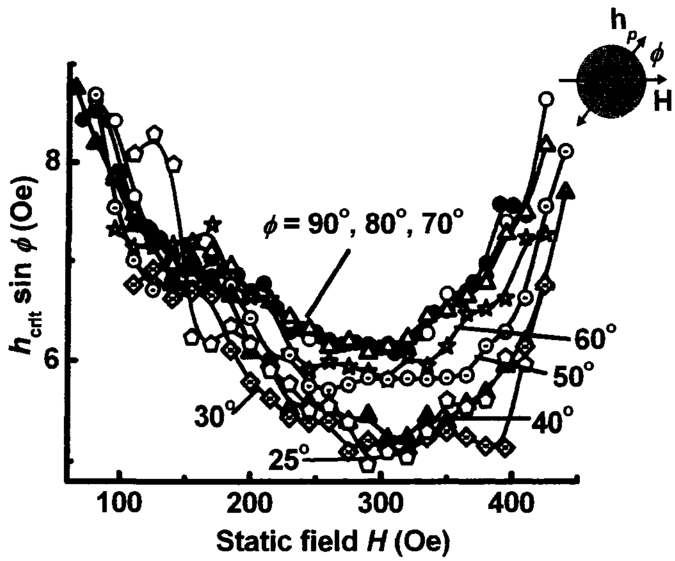

FIG. 7.5. Graphs of $h_{\text{crit}}\sin\phi$ vs. H field for the 104 nm thin film. The H field and the h_p field were in-plane and at the ϕ angles indicated. The corresponding h_{crit} vs. H data are shown in Fig. 7.4 graphs (a) and (b).

If there is no contribution from the parallel pumping process, the h_{crit} values should scale by a factor of $\sin\phi$, and graphs of $h_{\text{crit}}\sin\phi$ vs. H data should all lie along the same curve. Figure 7.5 shows $h_{\text{crit}}\sin\phi$ vs. H graphs for the 104 nm thin film and for all ϕ angles. The fields are in the film plane at the coupling configurations indicated. Notice that these are the same data as in Fig. 7.4 graphs (a) and (b) but weighted by $\sin\phi$.

The $h_{\text{crit}}\sin\phi$ data for $\phi = 90$, 80, and 70° all lay on the same curve, more or less. For smaller ϕ angles there is a drop in $h_{\text{crit}}\sin\phi$ data below this curve. This shows that energy is, in fact, coupled into the spin wave modes by the parallel pumping process. This coupling, however, is weak. In the $\phi = 0^{\circ}$ limit, the overall coupling is so weak that no parallel pumping response is observed.

7.3 FIRST ORDER SPIN WAVE INSTABILITY THEORY FITS TO THE BUTTERFLY CURVES

This section gives an analysis of theoretical fits to the butterfly curve data with the first order SWI theory presented in Ch. 3. Subsection 7.3.1 shows that the best fits to the data require a wave vector dependent spin wave linewidth. The ΔH_k trial function includes the phenomenological Gilbert damping and a $\sin^2 2\theta_k$ trial function that is loosely related to three magnon relaxation. Subsection 7.3.2 discusses the fits to the data and subsection 7.3.3 presents the corresponding critical spin wave modes.

7.3.1 SPIN WAVE LINEWIDTH TRIAL FUNCTIONS

Chapter 5 showed first order SWI theoretical fits to the SA butterfly curve data for the 104 nm thin film with three different ΔH_k trial functions. The first fit used a trial function of the form $\Delta H_k = A$ where A is a constant. This showed a good fit to the high field data only. The second fit used a trial function of the form $\Delta H_k = A + B\sin^2 2\theta_k$. Here the A is again a constant and the term that depends on θ_k is loosely related to three magnon relaxation. This showed a good fit to the minimum and high field portions of the butterfly curve and improved the fit to the low field data. The third fit used a trail function of the form $\Delta H_k = 2\alpha A_k / |\gamma| + B\sin^2 2\theta_k$ where $2\alpha A_k / |\gamma|$ is the phenomenological Gilbert damping term. The α is the Gilbert damping parameter and A_k is given in Eq. (3.23). This showed a very similar fit to that of the second trial function for large coupling angles but not for small angles. It was not clear from the subsidiary absorption data alone if the second or third trial function would best fit the oblique pumping data.

Figure 7.6 graphs (a), (b), and (c) show example $h_{\rm crit}$ vs. H data from Fig. 7.4 for the 104 nm and for $\phi = 90$, 40, and 30°, respectively. The solid blue curves are for fits to the data with the $\Delta H_k = A + B\sin^2 2\theta_k$ trial function. The best fit values are $A = 25$, 29, and 31.5 Oe for $\phi = 90$, 40, and 30°, respectively, and $B = 70$ Oe for all

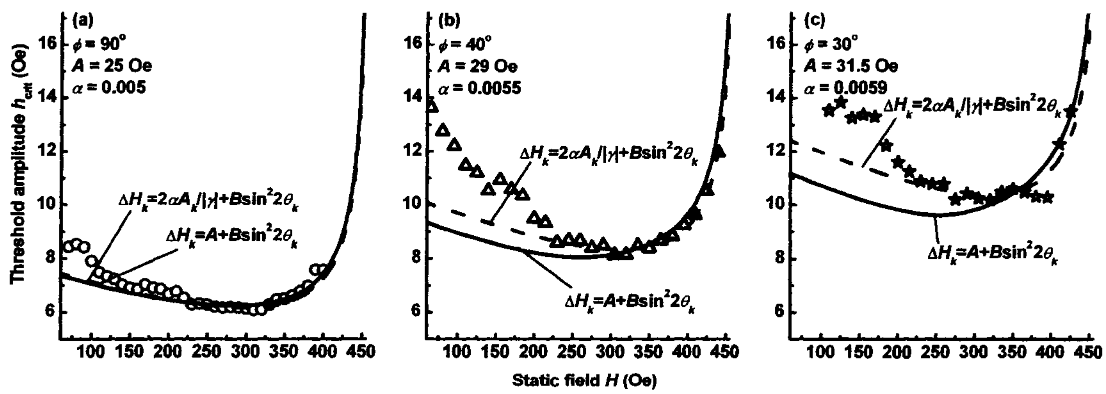

FIG. 7.6 Oblique pumping butterfly curves of $h_{\rm crit}$ vs. H for the 104 nm thin Permalloy film, as seen in Fig. 7.4, and theoretical fits to the data based on first order SWI theory. The solid curves are fits to the data with the trial function $\Delta H_k = A + B\sin^2 2\theta_k$. The dashed curves are fits to the data with the trial function $\Delta H_k = 2\alpha A_k / |\gamma| + B\sin^2 2\theta_k$. The α and A values for the fits are as indicated. The B value for all fits was 70 Oe.

theoretical fits. The red dashed curves are for fits to the data with the $\Delta H_k = 2\alpha A_k / |\gamma| + B\sin^2 2\theta_k$ trial function. The best fit values are $\alpha = 0.005$, 0.0055, and 0.0059 for $\phi = 90$, 40, and 30°, respectively, and, again, $B = 70$ Oe for all butterfly curve fits. The fits the data are based on the film parameters given in Ch. 4 and a best fit D value of 2.38×10^{-9} Oe cm^2/rad^2. Notice that it was necessary to vary the exchange constant D in order to fit the butterfly curves. This shows a strong dependence of the thresholds on the exchange interaction. The strong dependence on the exchange interaction results from the coupling of energy into larger θ_k modes.

The solid blue curves show good fits to the high field data in all three graphs and a reasonably good fit to the minimum of the butterfly curve in graph (a). The solid blue curves do not fit the minimums of the data in graphs (b) and (c) and do not fit the low field data in any of the graphs. The red dashed curves show good fits to the minimum and high field portions of the data in all three graphs. For H fields below about $H = 225$ Oe the fits deviate significantly from the data. This deviation is due to a break down of the Harte approximation and is discussed in Sec. 7.4.2. Overall the trial function that includes the Gilbert damping shows better fits to the data.

7.3.2 FIRST ORDER SPIN WAVE INSTABILITY THEORY FITS TO THE DATA

Figure 7.7 shows the butterfly curve data, given in Fig. 7.4, and theoretical fits to the data based on the first order SWI theory presented in Ch. 3 with a spin wave linewidth trial function of $\Delta H_k = 2\alpha A_k / |\gamma| + B\sin^2 2\theta_k$. The fits to the data are based on the film parameters given in Ch. 4 and D values of 2.38×10^{-9} and 2.20×10^{-9} Oe cm^2/rad^2 for the 104 and 123 nm films, respectively. The Gilbert damping parameters α used for the fits are given in Table 7.1. For both samples and all butterfly curve fits, the B parameter was constant at 70 Oe. The dashed line marks the H_{cut} that corresponds to the spin wave band edge effect.

Figure 7.7 shows that the first order SWI theory, with a zeroth order thin film approximation, provides a reasonable match to the measured oblique pumping butterfly curves for fields above 200 Oe or so. Below this field, value the data deviate significantly from the fits.

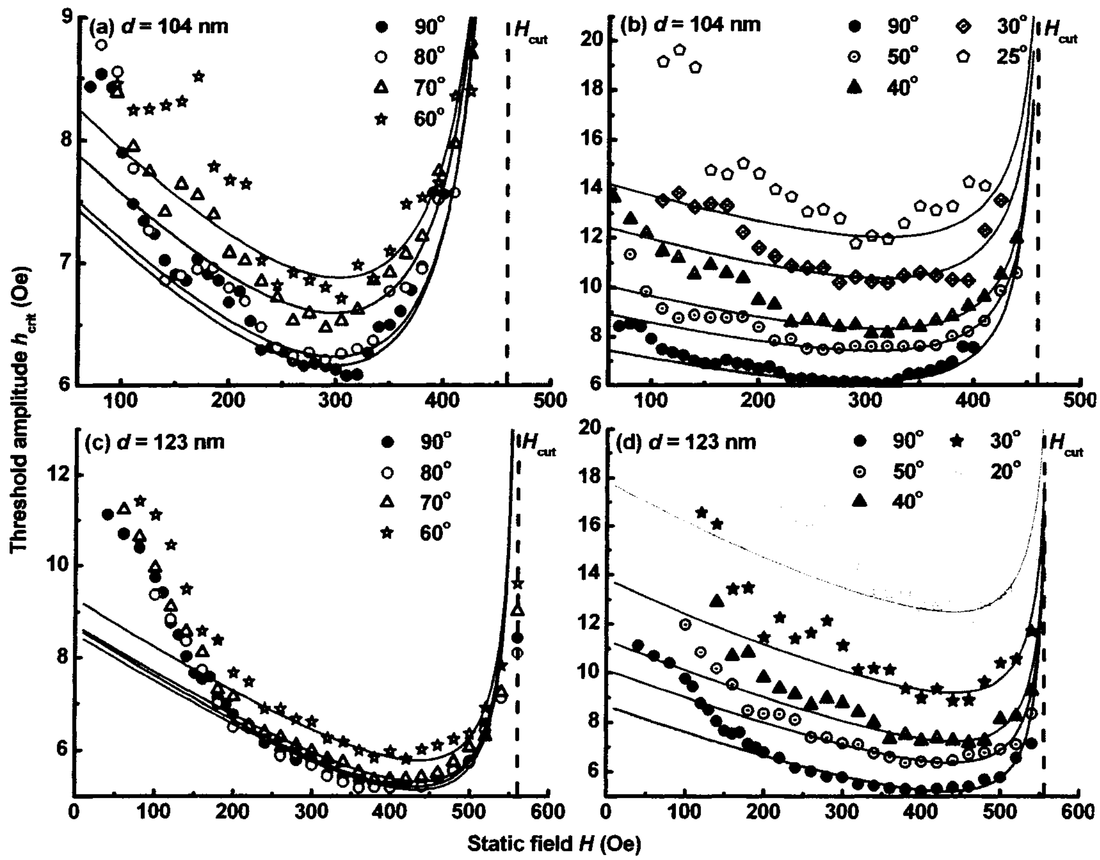

FIG. 7.7. Oblique pumping butterfly curves of h_{crit} vs. H for the 104 and 123 nm thin Permalloy films, as seen in Fig. 7.4, and first order SWI theory fits to the butterfly curves. The solid curves are fits to the data with the trial spin wave linewidth function $\Delta H_k = 2\alpha A_k / |\gamma| + B\sin^2 2\theta_k$. The α and A values for each coupling angle ϕ are given in Table 7.1. The B value for all fits was 70 Oe. The H field and the h_p field were in-plane and at the coupling angles ϕ indicated.

The $\Delta H_k = 2\alpha A_k / |\gamma| + B\sin^2 2\theta_k$ trial spin wave linewidth function is somewhat different than that needed to obtain good theoretical fits to butterfly curve data for ferrites. Previous in-plane subsidiary absorption and oblique pumping work on single crystal YIG ferrites, by Liu and Patton (1982) and Patton and Jantz (1979), generally require a spin wave linewidth in the form $\Delta H_k = A' + B'\sin^2 2\theta_k + C' L(k)$,

TABLE 7.1. Summary of parameters for the fits of the SWI theory to the oblique pumping curve data for the 104 and 123 nm samples.

Coupling angle ϕ (deg)	Spin wave linewidth parameters in the $\Delta H_k = 2\alpha A_k / \lvert\gamma\rvert + B\sin^2 2\theta_k$ function			
	104 nm thin film		123 nm thin film	
	Spin wave Gilbert damping parameter α	Three magnon process parameter B (Oe)	Spin wave Gilbert damping parameter α	Three magnon process parameter B (Oe)
90	0.0050	70	0.0046	70
80	0.0052	70	0.0046	70
70	0.0055	70	0.0047	70
60	0.0055	70	0.0049	70
50	0.0055	70	0.0050	70
40	0.0055	70	0.0050	70
30	0.0059	70	0.0054	70
25	0.0062	70	--	--
20	--	--	0.0058	70

where the Sparks function $C'L(k)$ gives something between a linear and a step response in k that loosely accounts for three magnon relaxation [Sparks (1964)]. The Sparks function was derived for spheres and is not applicable for thin films, as there are no available low k values for small θ_k values. Additionally, a constant A' term gave only poor fits to the data. Good fits required the introduction of a substantial k dependent component to ΔH_k, as discussed previously. The difference in the ΔH_k functions needed to fit the data for thin metal films is not a surprise, since the physical relaxation mechanisms are known to be quite different.

7.3.3 CRITICAL SPIN WAVE MODES

Figure 7.8 shows critical mode k_{crit} and θ_{crit} vs. H profiles that correspond to the butterfly curve responses in Fig. 7.7. Graphs (a) and (b) show the individual k_{crit} vs. H and θ_{crit} vs. H CM profiles, respectively, for the 104 nm thin film and for the applicable ϕ angles. The ϕ angles for the curves in Graph (a) are as indicated. The ϕ angles for the curves in Graph (b) are not indicated, as the maximum deviation between the curves is only 1°. The vertical dot-dashed lines mark the corresponding cutoff field H_{cut} from Fig. 7.4. Graphs (c) and (d) show the CM profiles in polar form or θ_{crit} vs. k_{crit} profiles for the 104 and 123 nm films, respectively, and for the applicable ϕ angles, as indicated.

Figure 7.8 (a) shows a decrease in the low field k_{crit} from 3.2×10^5 rad/cm to 2.0×10^5 rad/cm, as the coupling angle ϕ is decreased. For all coupling angles the k_{crit} values increase with an increase in the H field to their respective maximum values. The curves converge to $k_{crit} = 2.92\times10^5$ rad/cm as the static field approaches H_{cut}.

Graph (b) shows for all ϕ that the θ_{crit} follow the same basic curve. The θ_{crit} values for low field are around 15.5° and decrease nearly linearly with field until a static field of about 300 Oe. Above this field value the θ_{crit} shows a sharp decrease to about 1.5°, as the static field approaches the H_{cut} value.

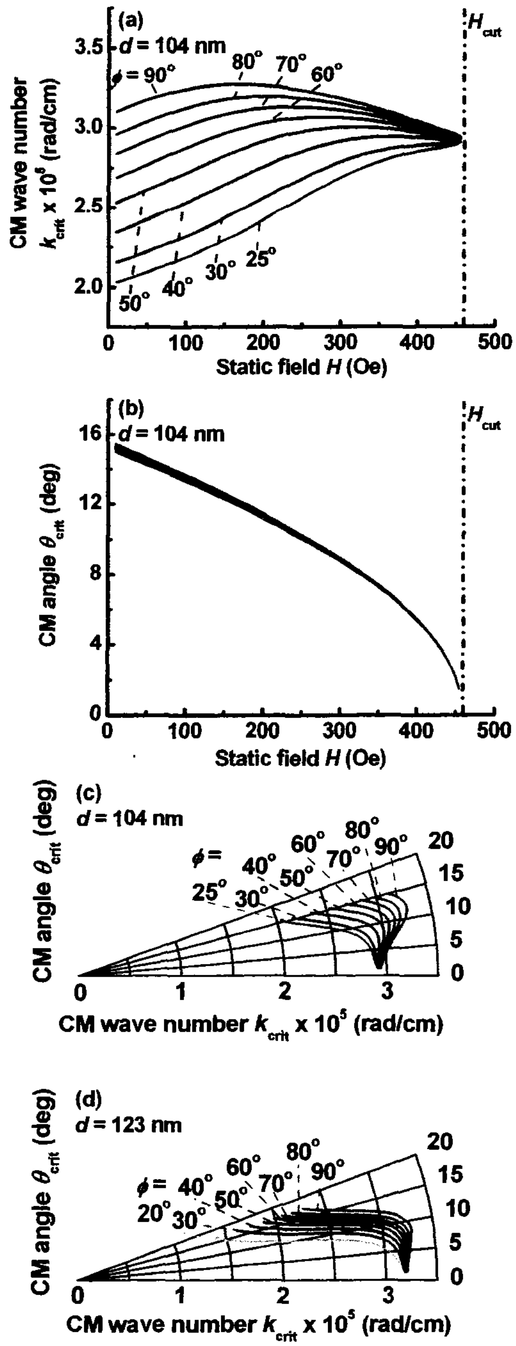

FIG. 7.8. Graphs (a) and (b) show the k_{crit} and θ_{crit} vs. H graphs, respectively, that correspond to the computed butterfly curves in Fig. 7.7 for the 104 nm thin film and for the applicable coupling angles ϕ. The ϕ are as indicated in Graph (a). The ϕ are not indicated in Graph (b). The vertical dot-dash lines show the cutoff field H_{cut}. Graphs (c) and (d) show the combined CM results in polar form for the 104 and 123 nm thin films, respectively, for the applicable coupling angles, as indicated.

Graph (c) shows that the range of the k_{crit} values is 2.0×10^5 rad/cm to 3.3×10^5 rad/cm. This is narrower that that of the 123 nm film. Graph (d) shows that the range of the k_{crit} values for the 123 nm film is 1.4×10^5 rad/cm to 3.3×10^5 rad/cm. The range of the θ_{crit} values is also larger for the 123 nm film than for the 104 nm film and is from 17.3° to 1.5°. The θ_{crit} values for the 104 nm film range from 15° to 1.5°. Notice that for both graphs the curves converge to $\theta_{crit} = 1.5°$.

As discussed previously, the butterfly curves in Fig. 7.7 are notably different from those for bulk ferrites and, correspondingly, the critical mode profiles are also quite different. For single crystal YIG and for the $\phi = 90°$ configuration, the k_{crit} values decrease linearly until the field point associated with the minimum of the butterfly curve. At this field point the wave vector abruptly drops to zero and sticks at zero up to H_{cut}. The θ_{crit} values stick close to 45° for fields below the minimum of the butterfly curve and then drop smoothly to zero for fields above the minimum field. For the $\phi = 0°$ configuration, the k_{crit} values decrease smoothly to zero at the H point associated with the minimum of the butterfly curve and stick at zero up to H_{cut}. The θ_{crit} values stick at 90° for fields below the minimum of the butterfly curve and then decrease [Patton and Jantz (1978), Patton (1980)].

The extreme differences between the CM profiles for bulk single crystal YIG and Permalloy thin films can be explained by (1) the very different nature of the spin wave dispersion curves because of the thin film geometry and the high saturation magnetization, (2) the different k and θ_k dependences of the $W_k^{(1)\perp}$ and $W_k^{(1)\parallel}$ coupling coefficients, (3) the different k and θ_k dependences of the spin wave linewidth ΔH_k, and (4) the very high saturation magnetization M_s in Permalloy relative to ferrites. In particular, the available spin wave modes for energy to be coupled into are different for thin films due to the differences in the spin wave band for thin films relative to bulk, the differences in the bottom of the spin wave band result in different three magnon scattering selection rules, and magnon-electron relaxation processes must be considered.

7.4 CONCLUSIONS FROM THE OBLIQUE PUMPING DATA ANALYSIS

This section discusses the two main points from the oblique pumping butterfly curve analysis. Subsection 7.4.1 discusses angle dependent Gilbert damping parameters α. The OP damping parameters, in combination with those from FMR and RS, indicate that the 123 nm film has an overall lower loss compared to the 104 nm film. The lowest α values occur for subsidiary absorption and are in agreement with those obtained from resonance saturation. All α values are consistent with those expected for magnon-electron relaxation. Subsection 6.4.2 discusses the fits to the data at low static fields. The spin wave dispersion curves used for the analyses are not correct in the ranges of the resultant k_{crit} and θ_{crit} values.

7.4.1 DAMPING PARAMETERS

As in Ch. 6, the Gilbert damping parameter associated with FMR, α_{FMR}, provides a useful comparison to the α parameters here. The α_{FMR} values for the 104 and 123 nm films are 0.0093 and 0.0090, respectively. Additionally, the α_{RS} found in Ch. 6 can also provide useful for comparison and are 0.0050 and 0.0048 for the 104 and 123 nm films, respectively. Table 7.1 shows that for large coupling angles, around $\phi = 90^{\circ}$ or so, both films show α values that are the same as the corresponding α_{RS} value or lower. These α values are lower, by about a factor of two, than the corresponding α_{FMR} values. As discussed in Ch. 6, the generally lower α_{RS} values are in the range nominally associated with intrinsic magnon-electron relaxation processes only [Meckenstock *et al.* (1995), Frait and Fraitova (1980), Meckenstock *et al.* (2004)]. The α values for large coupling are correspondingly in the range associated with electron relaxation processes.

Figure 7.9 shows plots of the Gilbert damping parameters α used for the fits in Fig. 7.7 and give in Table 7.1 as a function of ϕ. The red circle and blue triangle data are for the 104 and 123 nm thin films, respectively. The dashed red and blue horizontal lines at $\alpha = 0.0050$ and 0.0048 indicate the α_{RS} values obtained from the RS experiment for the 104 and 123 nm films, respectively, as given in Ch. 6.

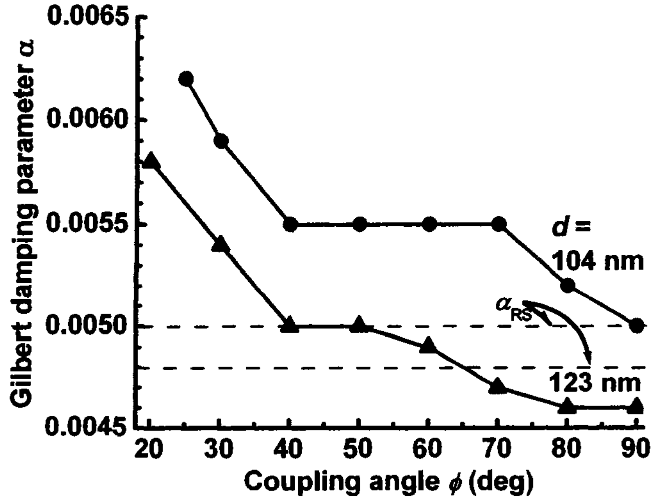

FIG. 7.9. Gilbert damping parameter α vs. ϕ used in the butterfly curve fits in Fig. 7.7 and listed in Table 7.1. The red circle and blue triangle data are for the 104 and 123 nm thin films, respectively. The dashed red and blue lines indicate the α_{RS} parameters found from the RS analysis for the 104 and 123 nm films, respectively.

Figure 7.9 shows two main points. First, the α parameters for the 123 nm film are consistently lower than those of the 104 nm film by about 0.0005. The α_{RS} and α_{FMR} values for the 123 nm film, as mentioned above, are also lower than the values for the 104 nm film. This indicates that the 123 nm thin film is an intrinsically lower loss film than the 104 nm film.

Second, the α parameters increase as the ϕ angle decreases. As mentioned, the α parameters for large ϕ angles agree reasonably well with the α_{RS} values for the respective films. It appears that there is an increase in damping as the ϕ angle decreases. However, the spin wave relaxation should be an intrinsic property of the sample and, as such, should not depend on the ϕ angle. There are two possible reasons for this increase (1) the Harte thin film approximation used to find closed solutions for the coupling coefficients and the spin wave dispersion relation is not sufficient and (2) the trial function used to fit the data is not adequate to fully describe the relaxation processes. To investigate this further, full exact numerical calculations of the coupling coefficients and the spin wave dispersion relation are required.

7.4.2 THEORETICAL FIT AT LOW FIELDS

As discussed above, below some particular H field the theoretical fit deviates significantly from the h_{crit} data. This is the result of a break down of the Harte thin film approximation. The Harte approximation breaks down in the limits of large k and θ_k values, as discussed in Ch. 3.

Figure 7.10 graphs (a) – (d) show f_k vs. k dispersion curve branches for the 104 nm film at $H = 400$, 300, 200, and 100 Oe, respectively. The red, blue and green branches were calculated from the spin wave dispersion relation found with the Harte approximation. The red and blue curves are for $\theta_k = 90^{\circ}$ and 0°, respectively.

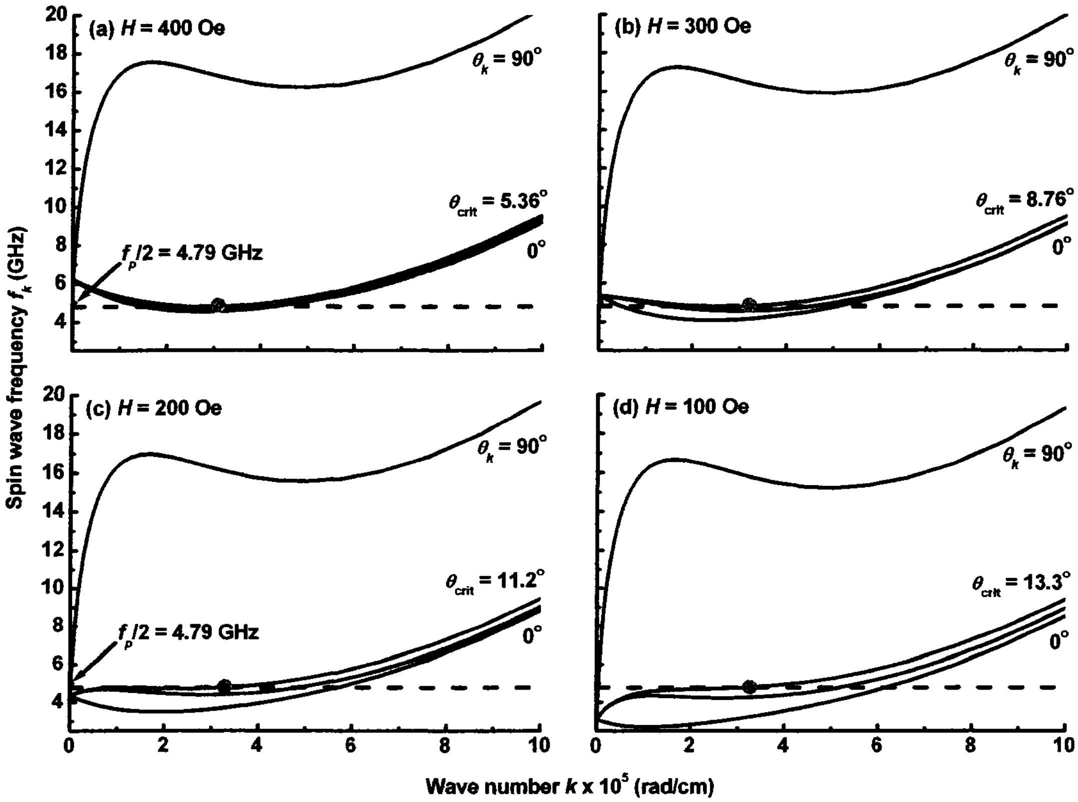

FIG. 7.10. Spin wave frequency f_k vs. k curves for the 104 nm film at four static field H values, as indicated. The red and blue curves are the $\theta_k = 90^\circ$ and 0° braches of the thin film dispersion curve calculated with the Harte approximation. The green curves are calculated with the Harte approximation and are for the indicated θ_{crit} angles and the purple curves are the corresponding dispersion curve branches found by an exact numerical calculation. The dashed line marks the half pump frequency $f_p/2 = 4.79$ GHz. The angles are as indicated. The grey dots indicate the critical mode for the particular field value from the theoretical fit to the butterfly curve for the 104 nm film and a $\phi = 90^\circ$, as seen in Fig. 7.9.

The green curves in graphs (a), (b), (c), and (d) are for the θ_{crit}=5.36°, 8.76°, 11.2°, and 13.3°, respectively, and the purple curves are corresponding branches found from an exact numerical calculation. The grey dots mark critical spin wave modes found from the theoretical fit to the $\phi = 90^\circ$ butterfly curve data for the 104 nm film, as shown in Fig. 7.9. The dashed lines are cuts at the half pump frequency $f_k = f_p/2 = 4.79$ GHz.

Graph (a) shows a reasonable match up between the exact and approximate dispersion curve calculations for the indicated critical mode at $H = 400$ Oe. Graph (b) shows that the exact dispersion curve for the indicated θ_{crit} is slightly lower in frequency then the approximate curve for $H = 300$ Oe. Graphs (c) and (d) show that there is no or little separation in frequency between the exact and approximate dispersion curves in the range of low k and θ_k. For lower fields and the corresponding larger θ_{crit} values the difference between the two classes of dispersion branches increases.

The ability to achieve a reasonable fit to the data for fields above about 225 Oe, as seen in Fig. 7.7, shows that the deviation between the exact and approximate dispersion curve branches is not significant for the θ_{crit} values of interest. However, the exact dispersion curves for fields below 225 Oe, in graphs (c) and (d), show that the critical modes from the theoretical fits are not the true modes.

To properly fit the butterfly curve data with exact thin film theory a general nonlocal exchange analysis through numerical methods [Wames and Wolfram (1970)] or Green's function analysis [Kalinikos and Slavin (1986)] is required. This greatly complicates the minimization over the available spin wave modes to find the lowest threshold field. This was not done but is very important for continued work.

REFERENCES

[An *et al.* (2004)] S. Y. An, P. Krivosik, M. A. Kramer, H. M. Olson, A. V. Nazarov, and C. E. Patton, J. Appl. Phys. **96**, 1572 (2004).

[Frait and Fraitova (1980)] Z. Frait and D. Fraitova, J. Magn. Magn. Mater. **15**, 1081 (1980).

[Green *et al.* (1969)] J. J. Green, C. E. Patton, and E. Stern, J. Appl. Phys. **40**, 172 (1969).

[Harte (1968)] K. J. Harte, J. Appl. Phys. **39**, 1503 (1968).

[Kalinikos and Slavin (1986)] B. A. Kalinikos and A. N. Slavin, J. Phys. C **19**, 7013 (1986).

[Liu and Patton (1982)] Y. H. Liu and C. E. Patton, J. Appl. Phys. **53**, 516 (1982).

[Meckenstock *et al.* (1995)] R. Meckenstock, O. v. Geisau, J. Pelzl, and J. A. Wolf, J. Appl. Phys. **77**, 6439 (1995).

[Meckenstock *et al.* (2004)] R. Meckenstock, D. Spoddig, Z. Frait, V. Kambersky, and J. Pelzl, J. Magn. Magn. Mater. **272**, 1203 (2004).

[Patton (1970)] C. E. Patton, J. Appl. Phys. **41**, 431 (1970).

[Patton and Jantz (1978)] C. E. Patton and W. Jantz, IEEE Trans. Magn. **14**, 698 (1978).

[Patton and Jantz (1979)] C. E. Patton and W. Jantz, J. Appl. Phys. **50**, 7082 (1979).

[Patton (1980)] C. E. Patton, Proceedings of the International Conference, October 1980, High Power Microwave Processes and Parametric Pumping in Single Crystal Ferrites.

[Sparks (1964)] M. Sparks, *Ferromagnetic Relaxation Theory* (McGraw-Hill, 1964).

[Wames and Wolfram (1970)] R. E. D. Wames and T. Wolfram, J. Appl. Phys. **41**, 987 (1970).

[Wiese *et al.* (1995)] G. Wiese, P. Kabos, and C. E. Patton, Phys. Rev. B **51**, 15085 (1995).

SUMMARY

INTRODUCTION

A comprehensive study of the high power resonance saturation and oblique pumping responses in thin Permalloy films has been performed. The objective of this study was to understand the basic nonlinear interactions and the corresponding relaxation mechanisms associated with the first and second order SWI processes in thin metal films. This objective was met through, (1) improvements to the high power FMR system and the resolution of cavity loading and calibration issues, (2) carefully calibrated resonance saturation measurements and a theoretical analysis of the threshold data, based on second order SWI theory, suitably modified for thin films, and (3) carefully calibrated oblique pumping measurements and a theoretical analysis of the threshold data, based on first order SWI theory, suitably modified for thin films.

8.1 IMPROVEMENTS TO THE HIGH POWER FMR SYSTEM AND NEW CALIBRATION TECHNIQUES

The high power FMR system has two main experimental modes of operation. The first experimental mode of operation is for low and high power FMR measurements. The low and high power FMR profiles are found by measurements of the voltage reflection coefficient ρ as a function of the static field H for specific microwave input powers P_{in}. The second experimental mode is for high power threshold measurements. The threshold curves are found from measurements of ρ vs. P_{in} for a set H field. To determine h_{crit} from the threshold measurements, calibrated ρ vs. microwave threshold field amplitude h_p responses must be determined through a precise cavity calibration from the ρ vs. P_{in} data.

Two improvements to the high power FMR system serve to increase the accuracy and efficiency of the system. The first improvement was the implementation of a new calibration procedure. The calibration procedure accounts for the system losses to provide accurate input and reflected power levels at the cavity position. The calibration takes into account variations in loss due to changes in the microwave frequency and includes precise calibrations of the variable attenuators. The second system improvement is the full automation of the high power system for threshold measurements over a H field range of interest. These modifications include new hardware, software, and critical calibrations of the computer controlled mechanical parts. The automation of the system reduces the maximum time for a full set of threshold measurements by over 75%.

Calibration issues that prevent precise h_{crit} determinations were resolved through a careful decoupling of the $\mathbf{h}_p$ and $\mathbf{H}$ fields and a full cavity response calibration. The cavity is decoupled to the point where one can define $C = h_p^2 / P_{in}$ for the sample loaded cavity and transition to a "calibrated" result. The full cavity calibration response takes into account the changes in the cavity parameters. This is important, in particular, over the field range of FMR, as the cavity parameters change with the real and imaginary parts of the susceptibility. The resolution of the cavity loading and calibration issues reduces field calibration errors at FMR by over 35%.

8.2 EXPERIMENTAL RESONANCE SATURATION RESULTS

Resonance saturation FMR profiles have been measured as a function of microwave power for a series of Permalloy films that range in thickness from 35 – 123 nm at 9.11 GHz and room temperature. The results show the basic resonance saturation response associated with second order SWI processes and a foldover effect that preliminary results suggest is due to two-magnon scattering interactions [Krivosik (2006)].

Spin wave instability threshold h_{crit} measurements have also been made over the full FMR absorption profile. Careful attention to cavity loading and calibration issues has yielded the first comprehensive data on second order spin wave instability processes at FMR and over the full FMR profile for thin metal films. These h_{crit} measurements demonstrate the threshold nature of the nonlinear response. The overall shapes of the resultant h_{crit} vs. H curves are closely tied closely to the low power FMR response. The jumps in the butterfly curves correspond to the foldover effect of the high power FMR profiles.

Chapter 3 presents the second order SWI, suitably modified for thin films. The theory provides the working equations for h_{crit} determinations and the corresponding critical modes. An outline of the operational procedure for the analysis of the butterfly curves is presented in Ch. 5. The results of the theoretical analyses are presented in Ch. 6.

For each film, the theoretical analyses yielded good fits to the butterfly curve data based on a single field independent value of the spin wave linewidth or spin wave relaxation rate η_k. These linewidths and the corresponding Gilbert damping parameter values are consistent with those expected for intrinsic magnon-electron relaxation [Kalarickal *et al.* (2006), Kambersky and Patton (1975)]. Additionally, the use of constant η_k values for the fits is significant in that the associated relaxation times are constant and in the small range 3 – 7 ns. It is important to note that the fits are not strongly dependent on the exchange interaction and a typical value for Permalloy was used for all fits [Nisenoff and Terhune (1965)]. The resonance saturation butterfly curve data and the corresponding fits are only the second such results on record. The first such results required the introduction of a substantial k dependent component to η_k.

The corresponding critical mode propagation angles $\theta_{\rm crit}$ for all films are constant at 0°. This is consistent with the original second order SWI theory for bulk isotropic ferrites biased at the FMR field [Suhl (1957)]. The spin wave frequency is equal to the microwave pumping frequency for second order processes, so that the critical mode wave vectors $k_{\rm crit}$ are completely specified. The $k_{\rm crit}$ are essentially constant over the full FMR profile which explains the good fits for a constant η_k.

The FMR precession angles at threshold show a lock up as the microwave power exceeds the SWI threshold and energy is pumped into spin waves. The FMR precession angles at threshold are quite small, on the order of a few degrees.

8.3 EXPERIMENTAL OBLIQUE PUMPING RESULTS

Oblique pumping field swept measurements for a range of coupling ϕ angles have been measured as a function of microwave power for Permalloy films of thicknesses 104 and 123 nm at 9.58 GHz and room temperature. The results show the basic oblique pumping response associated with first order SWI processes. The oblique pumping response is not a continuous effect but rather a threshold effect.

Spin wave instability threshold $h_{\rm crit}$ measurements have been made over the full oblique pumping field range. These data represent the first comprehensive threshold measurements at oblique angles for first order SWI processes in thin metal films. It is important to note that comprehensive subsidiary absorption measurements on thin metal films were performed previously by An *et al.* (2004).

The oblique pumping h_{crit} measurements demonstrate the threshold nature of the first order nonlinear response. The increase in h_{crit} with the decrease in ϕ angle and the lack of response for very small ϕ angles shows a very weak coupling of energy from h_p into the spin wave modes due to the parallel pumping process. The data show cutoffs at high field that depend on the film thickness. These cutoff fields correspond to the field points at which the bottom of the spin wave band is above one half the microwave pump frequency.

Chapter 3 presents first order SWI, suitably modified for thin films. This theory provides the working equations for h_{crit} determinations and the corresponding critical modes for the first order processes. An outline of the operational procedure for the analysis of the butterfly curves is presented in Ch. 5. The results of the theoretical analyses are presented in Ch. 7.

For both films the theoretical analyses yielded good fits to the butterfly curve data with the exception of the low field data. This is due to a break down of the Harte thin film approximation. The fits were based on a η_k trial function that depended on a phenomenological Gilbert damping term and a θ_k dependent trial function. A constant value of the B parameter associated with the θ_k dependent trial function was used for all the fits. The α parameters for both films and for $\phi = 90°$ agree with the α values found from the resonance saturation study but increased for smaller coupling angles. The oblique pumping, resonance saturation, and FMR Gilbert damping parameters were all lower for the 123 nm film than for the 104 nm film. This implies that the 123 nm film has an overall lower loss than the 104 nm film. The butterfly curve fits show a strong dependence on the exchange interaction due to the coupling of energy into larger θ_k values than for resonance saturation. The D value was varied to provide the best fit to the data.

The θ_{crit} and k_{crit} values that correspond to the butterfly curve fits vary substantially over range of fields for oblique pumping. This is consistent with the results for bulk isotropic ferrites [Patton (1979)]. Exact calculations of the thin film dispersion curve show that the critical modes from the theoretical fit in the low field region are not available modes. This discrepancy explains the deviation of the fits from the low field data and is due to a break down of the Harte thin film approximation used to find closed solutions to the coupling coefficients and the spin wave dispersion relation. Full numerical calculations of the coupling coefficients and the spin wave dispersion are required to analyze the low field data properly.

8.4 FUTURE WORK ON METAL FILMS

The study of high power FMR in thin metal films provides a starting point for future work on thin metal films and simultaneously introduces a multitude of new unanswered questions. There are three main areas for future high power FMR work on thin metal films. First, out-of-plane measurements of the SWI processes in thin Permalloy films are necessary in order to complete the basic experimental study of Permalloy. Second, with the ground work laid for high power experiments on metal films, the study of SWI processes in larger loss metal and patterned films is necessary for new technologies. Lastly, SWI theory for thin films needs to be (a) numerically calculated to provide proper fits to the experimental results, (b) further developed to understand the two magnon effects on the resonance saturation data, (c) expanded to provide the capability to analyze data above the instability threshold, and (d) connected to large angle switching. These studies are important for the advancement of technology, as they provide valuable information for applications such as nano contacts and storage information technology.

REFERENCES

[An *et al.* (2004)] S. Y. An, P. Krivosik, M. A. Kramer, H. M. Olson, A. V. Nazarov, and C. E. Patton, J. Appl. Phys. **96**, 1572 (2004).

[Kalarickal *et al.* (2006)] S. S. Kalarickal, P. Krivosik, W. M., C. E. Patton, M. L. Schneider, P. Kabos, T. J. Silva, and J. P. Nibargar, J. Appl. Phys. **99**, 093909 (2006).

[Kambersky and Patton (1975)] V. Kambersky and C. E. Patton, Phys. Rev. B **11**, 2668 (1975).

[Krivosik (2006)] P. Krivosik, Technical Digests, IEEE International Magnetics Conference, San Diego, CA, 8-12 May 2006, (unpublished), Paper No. BA-06.

[Nisenoff and Terhune (1965)] M. Nisenoff and R. W. Terhune, J. Appl. Phys. **36**, 732 (1965).

[Patton (1979)] C. E. Patton, Phys. Status Solidi B **92**, 211 (1979).

[Suhl (1957)] H. Suhl, J. Phys. Chem. Solids **1**, 209 (1957).

REFERENCES

[An *et al.* (2004)] S. Y. An, P. Krivosik, M. A. Kramer, H. M. Olson, A. V. Nazarov, and C. E. Patton, J. Appl. Phys. **96**, 1572 (2004).

[Anderson and Suhl (1955)] P. W. Anderson and H. Suhl, Phys. Rev. **100**, 1788 (1955).

[Arfken and Weber (2001)] G. B. Arfken and H. J. Weber, *Mathematical Methods for Physicists* (Harcourt/Academic Press, San Diego, 2001).

[Arias and Mills (1999)] R. Arias and D. L. Mills, Phys. Rev. B **60**, 7395 (1999).

[Ashcroft and Mermin (1976)] N. W. Ashcroft and N. D. Mermin, *Solid State Physics* (Harcourt, Inc., 1976).

[Berteaud and Pascard (1965)] A. Berteaud and H. Pascard, J. Appl. Phys. **36**, 970 (1965).

[Berteaud and Pascard (1966)] A. Berteaud and H. Pascard, J. Appl. Phys. **37**, 2035 (1966).

[Bloembergen and Damon (1952)] N. Bloembergen and R. W. Damon, Phys. Rev. **85**, 699 (1952).

[Bloembergen and Wang (1954)] N. Bloembergen and S. Wang, Phys. Rev. **93**, 72 (1954).

[Bozorth (1978)] Bozorth, *Ferromagnetism* (IEEE, Inc., New York, 1978).

[Chen and Patton (1994)] M. Chen and C. E. Patton, in *Nonlinear Phenomena and Chaos in Magnetic Materials*, edited by Wigen (World Scientific, Singapore, 1994), Ch. 3 Spin wave instability processes in ferrites.

[Cherepanov (1992)] V. B. Cherepanov, Phys. Rev. B **45**, 12397 (1992).

[Comly *et al.* (1963)] J. B. Comly, T. Penney, and R. V. Jones, J. Appl. Phys. **34**, 1145 (1963).

[Comly (1965)] J. B. Comly, Technicial Report No. 485, (unpublished) 1965.

[Cox *et al.* (2001)] R. G. Cox, C. E. Patton, M. A. Wittenauer, P. Kabos, and L. Chen, J. Appl. Phys. **89**, 4454 (2001).

[Dobin and Victora (2004)] A. Y. Dobin and R. H. Victora, J. Appl. Phys. **95**, 7139 (2004).

[Elmen (2007)] Elmen, In Encyclopaedia Britannica, Retrived August 29 2007, from Encyclopaedia Britannica Online: http://www.britannica.com/eb/article-9032459.

[Frait and Fraitova (1980)] Z. Frait and D. Fraitova, J. Magn. Magn. Mater. **15**, 1081 (1980).

[Frait and Patton (1980)] Z. Frait and C. E. Patton, Rev. Sci. Instrum. **51**, 1092 (1980).

[Gerrits *et al.* (2007)] T. Gerrits, P. Krivosik, M. L. Schneider, C. E. Patton, and T. J. Silva, Phys. Rev. Lett. **98**, 207602 (2007).

[Gilbert (1955)] T. A. Gilbert, Technical Report No. 11, (unpublished) 1955.

[Green and Kohane (1964)] J. J. Green and T. Kohane, SCP Solid State Tech. **49**, (1964).

[Green *et al.* (1969)] J. J. Green, C. E. Patton, and E. Stern, J. Appl. Phys. **40**, 172 (1969).

[Griffiths (1946)] J. H. E. Griffiths, Nature **158**, 670 (1946).

[Guan *et al.* (2007)] Y. Guan, W. E. Bailey, E. Vescovo, C. C. Kao, and D. A. Arena, J. Magn. Magn. Mater. **312**, 374 (2007).

[Harte (1964)] K. J. Harte, Technical Report No. 364, (unpublished) 1964.

[Harte (1968)] K. J. Harte, J. Appl. Phys. **39**, 1503 (1968).

[Hoefer *et al.* (2005)] M. A. Hoefer, M. J. Ablowitz, B. Ilan, M. R. Pufall, and T. J. Silva, Phys. Rev. Lett. **95**, 267206 (2005).

[Hurben (1996)] M. J. Hurben, Ph. D. dissertation, Colorado State University, Fort Collins, Colorado (1996).

[Jackson (1999)] J. D. Jackson, *Classical Electrodynamics* (John Wiley and Sons, Inc., 1999).

[Kalarickal *et al.* (2006)] S. S. Kalarickal, P. Krivosik, W. M., C. E. Patton, M. L. Schneider, P. Kabos, T. J. Silva, and J. P. Nibargar, J. Appl. Phys. **99**, 093909 (2006).

[Kalarickal (2007)] S. S. Kalarickal, Private communication, 2007.

[Kalinikos and Slavin (1986)] B. A. Kalinikos and A. N. Slavin, J. Phys. C **19**, 7013 (1986).

[Kambersky and Patton (1975)] V. Kambersky and C. E. Patton, Phys. Rev. B **11**, 2668 (1975).

[Kittel (1948)] C. Kittel, Phys. Rev. **73**, 155 (1948).

[Krivosik (2006)] P. Krivosik, Technical Digests, IEEE International Magnetics Conference, San Diego, CA, 8-12 May 2006, (unpublished), Paper No. BA-06.

[Krivosik (2007)] P. Krivosik, Private communication, 2007.

[Landau and Lifshitz (1935)] L. Landau and E. Lifshitz, Phys. Z. Sowjet Union **8**, 153 (1935).

[Liu and Patton (1982)] Y. H. Liu and C. E. Patton, J. Appl. Phys. **53**, 516 (1982).

[McKinstry *et al.* (1985)] K. D. McKinstry, C. E. Patton, and K. M., J. Appl. Phys. **58**, 925 (1985).

[McKinstry and Patton (1989)] K. D. McKinstry and C. E. Patton, Rev. Sci. Instrum. **60**, 439 (1989).

[McMichael and Krivosik (2004)] R. D. McMichael and P. Krivosik, IEEE Trans. Magn. **40**, 2 (2004).

[Meckenstock *et al.* (1995)] R. Meckenstock, O. v. Geisau, J. Pelzl, and J. A. Wolf, J. Appl. Phys. **77**, 6439 (1995).

[Meckenstock *et al.* (2004)] R. Meckenstock, D. Spoddig, Z. Frait, V. Kambersky, and J. Pelzl, J. Magn. Magn. Mater. **272**, 1203 (2004).

[Milton (1968)] A. F. Milton, Ph. D. dissertation, Harvard University, Cambridge, Massachusetts (1968).

[Nazarov (2002)] A. V. Nazarov, Ph. D. dissertation, Colorado State University, Fort Collins, Colorado (2002).

[Nazarov *et al.* (2002)] A. V. Nazarov, C. E. Patton, R. G. Cox, L. Chen, and P. Kabos, J. Magn. Magn. Mater. **248**, 164 (2002).

[Ni *et al.* (2006)] W. Ni, J. Kim, and E. C. Kan, IEEE Trans. Magn. **42**, 2827 (2006).

[Nisenoff and Terhune (1965)] M. Nisenoff and R. W. Terhune, J. Appl. Phys. **36**, 732 (1965).

[Olson *et al.* (2007)] H. M. Olson, P. Krivosik, K. Srinivasan, and C. E. Patton, J. Appl. Phys. **102**, 023904 (2007).

[Osaka *et al.* (2005)] T. Osaka, T. Asahi, J. Kawaji, and T. Yokoshima, Electrochimica Acta **50**, 4576 (2005).

[Osaka and Sayama (2007)] T. Osaka and J. Sayama, Electrochimica Acta **52**, 2884 (2007).

[Pascard and Berteaud (1964)] H. Pascard and A. Berteaud, C. R. Acad. Sc. Paris **258**, 2275 (1964).

[Pascard (1965)] H. Pascard, Ph.D. dissertation, University of Paris, Paris, France (1965).

[Patton (1968)] C. E. Patton, J. Appl. Phys. **39**, 3060 (1968).

[Patton (1969)] C. E. Patton, J. Appl. Phys. **40**, 2837 (1969).

[Patton (1970)] C. E. Patton, J. Appl. Phys. **41**, 431 (1970).

[Patton and Green (1971)] C. E. Patton and J. J. Green, Rev. Sci. Instrum. **42**, 193 (1971).

[Patton (1975)] C. E. Patton, in *Magnetic Oxides*, edited by Craik (Wiley, London, 1975), p. 575-645, Ch. 10 Microwave resonance and relaxation.

[Patton and Jantz (1978)] C. E. Patton and W. Jantz, IEEE Trans. Magn. **14**, 698 (1978).

[Patton (1979)] C. E. Patton, Phys. Status Solidi B **92**, 211 (1979).

[Patton and Jantz (1979)] C. E. Patton and W. Jantz, J. Appl. Phys. **50**, 7082 (1979).

[Patton (1980)] C. E. Patton, Proceedings of the International Conference, October 1980, High Power Microwave Processes and Parametric Pumping in Single Crystal Ferrites.

[Patton (2006)] C. E. Patton, Seagate Research Laboratory, Pittsburgh, Pennslyvania, 1 November 2006, (unpublished), Phenomenological Damping Precessional Dynamics.

[Schloemann (1959)] E. Schloemann, Technical Report No. R-48, (unpublished) 1959.

[Schloemann *et al.* (1960)] E. Schloemann, J. J. Green, and U. Milano, J. Appl. Phys. **31**, 386S (1960).

[Schloemann *et al.* (1963)] E. Schloemann, R. I. Joseph, and I. Bady, J. Appl. Phys. **34**, 672 (1963).

[Slavin and Kabos (2005)] A. N. Slavin and P. Kabos, IEEE Trans. Magn. **41**, 1264 (2005).

[Sparks (1964)] M. Sparks, *Ferromagnetic Relaxation Theory* (McGraw-Hill, 1964).

[Suhl (1957)] H. Suhl, J. Phys. Chem. Solids **1**, 209 (1957).

[Suhl (1959)] H. Suhl, J. Appl. Phys. **30**, 1961 (1959).

[Vendik *et al.* (1977)] O. G. Vendik, B. A. Kalinikos, and D. N. Chatorizhskii, Fiz. Tverd Tela **19**, 387 (1977).

[Waldron (1969)] R. A. Waldron, *Theory of Guided Electromagnetic Waves* (Van Nostrand Reinhold Company, London, 1969).

[Wames and Wolfram (1970)] R. E. D. Wames and T. Wolfram, J. Appl. Phys. **41**, 987 (1970).

[Wang *et al.* (2006)] X. H. Wang, H. Orikasa, N. Inokuma, Q. H. Yang, P. X. Hou, H. Oshima, K. Itoh, and T. Kyotani, J. Mater. Chem. **17**, 986 (2006).

[Weast and Astle (1982)] R. C. Weast and M. J. Astle, *CRC Handbook of Chemistry and Physics 63rd ed*, (CRC Press, Inc., 1982).

[Wiese *et al.* (1995)] G. Wiese, P. Kabos, and C. E. Patton, Phys. Rev. B **51**, 15085 (1995).

[Zakharov and Lvov (1973)] V. Zakharov and V. S. Lvov, Sov. Phys. Solid State **14**, 2513 (1973).

[Zhang *et al.* (1987)] Y. T. Zhang, C. E. Patton, G. Srinivasan, G. O. White, C. J. Brower, and C. A. Edmondson, Rev. Sci. Instrum. **58**, 620 (1987).